THE UNIVERSITY OF CHICAGO

SPACE: THE FINAL FRONTIER IN DYNAMIC REPRESENTATIONS IN MOTOR CORTEX

A DISSERTATION SUBMITTED TO

THE FACULTY OF THE DIVISION OF THE BIOLOGICAL SCIENCES

AND THE PRITZKER SCHOOL OF MEDICINE

IN CANDIDACY FOR THE DEGREE OF

DOCTOR OF PHILOSOPHY

COMMITTEE ON COMPUTATIONAL NEUROSCIENCE

BY

WEI LIANG

CHICAGO, ILLINOIS

MARCH 2023

COPYRIGHT

To my advisor Nicho, who gave me freedom and reassurance to explore.

To my animal colleagues, who remind me to make it count.

To my family, for their love, understanding and support.

TABLE OF CONTENTS

LIST OF FIGURES

LIST OF TABLES

LIST OF EQUATIONS

ACKNOWLEDGEMENTS

Advisor and Mentor

Nicho Hatsopoulos

Thesis Committee

Jason MacLean

Stephanie Palmer

Yali Amit

ARC Staff

Pierre Latalladi

Marquis Buchanan

Darya Mailhiot

Marek Niekrasz

Jenna Schoenberger

Jennifer McGrath

Alyssa Brown

Allison Ostdiek

Rebecca Turcios

Katia Silva

Cara Mitchell

Betty Theriault

Bridget Clancy

Erika Becerra

Hatlab Colleagues

Karthikeyan Balasubramanian

Vasileios Papadourakis

Carrie Balcer

Kazutaka Takahashi

Courtney Coleman

Rebecca Junod

Taylor Elder

Paul Aparicio

Hidenori Watanabe

Caleb Sponheim

Marina Sundiang

Jeff Walker

Dalton Moore

Alex Lee

Ariana Tortolani

Krystian Loetscher

Friederice Pirschel

Kai Qian

Fritzie Arce-MacShane

Rashi Bhatt

Grossman Institute

Elena Rizzo

Hoang Ngo

Parkker Burgan

Maya Suraj

Adriana Villegas

Amy Martiny

Lili González-Hernández

Animal Colleagues

Hermes

Breaux

Lester

Mack

Theseus

Kris

Jim

Einstein

Iris

My Family and Friends

ABSTRACT

The primary motor cortex (M1) is known for its general static correspondence between body parts and clustered sites on the physical cortical sheet – the somatotopic map. Under this view, it's tempting to believe that the orchestration of motor output in M1 is as rigid as manipulating the movement of a marionette, where a fixed set of strings would reliably dictate the movements of corresponding body parts of the puppet.

In this thesis work, we argue that motor representation on the M1 cortical sheet is in fact dynamic, from two perspectives: (1) the relationship between neural activity and muscle output is dynamic along movement execution; (2) the information-bearing neural activity itself is dynamically patterned across the cortical sheet during movement execution.

The first part of the work shows that, rather than being a static mapping, the relationship between neural activity and muscle output is constantly evolving during simple point-to-point reaches. Any given location on the cortical sheet bears the most information about different muscles at different times; any muscle is represented by different cortical locations at different times. Furthermore, this dynamic representation is movement-specific and most stable around movement onset, possibly serving functional needs. These dynamics happen at significantly shorter time scales than training-induced neural plasticity, presumably reflecting neural multiplexing unfolding over time.

The second part of the work shows that during movement execution M1 recruits spatially organized patterns of activity across the cortical sheet in a behaviorally specific manner. In particular, recruitment times form planar propagating patterns across the cortical sheet. The directions of those propagating patterns differ systematically according to reach directions,

bearing important kinematic information. This finding expands the repertoire of spatio-temporally complex neural codes and points to their potential facilitative roles in neural computation.

Together, this work speaks to the dynamic motor representation of the physical M1 cortical sheet. The effects that cortical activities have on the motor outputs are best understood by considering the interplay between space and time in characterizing population neural activity, and by considering the dynamic mapping between the cortex and effectors.

I. INTRODUCTION

Static cortical spatial organization in the primary motor cortex

Located along the precentral gyrus, the primary motor cortex (M1) is a brain region important for voluntary movement control, also a region where lowest electrical currents are needed to elicit body movements on the cortex (Fritsch & Hitzig, 1870). Here we review the rich literature studying how space on the cortical sheet is systematically organized to encode movement from a static perspective.

Cortical spatial maps encoding body parts

Since its discovery, the traditional view believed in an orderly arrangement of different body parts on M1. To begin with, English neurologist John Hughlings Jackson observed that his epilepsy patients displayed seizures spreading cross adjacent body regions, in a sequential order that is fixed for a patient but different across patients (Jackson, 1867). This observation made him hypothesize that this region we now call M1 had localized and systematic representation controlling movements of different body parts. Subsequently, this localizationist view was corroborated in live animals by Fritsch and Hitzig (1870) and Ferrier (1886), through surface electrical stimulations and lesions experiments.

As surface electrical stimulation techniques became relatively more focal, detailed maps were later plotted by Woolsey and collaborators (Woolsey, 1952) for monkeys and Penfield and collaborators (Penfield & Boldrey, 1937; Penfield & Rasmussen, 1950) for humans. In those simplified maps (termed simiusculus and homunculus respectively), a common theme of orderly arrangements from medial to lateral M1 existed, sequentially dedicated to foot, legs, trunk,

shoulder, upper limb, hands, face and mouth. Despite those simplified illustrations, they also noted that the actual boundaries were not clear-cut, with non-negligible overlaps. Furthermore, representations for hands, face and mouth – where finer movements were generally expected, were disproportionately large. Movements elicited in those studies were quite overt, given the intensity, duration and location of stimulation.

In order to obtain better specificity and easier interpretation than surface stimulations, Asanuma and Sakata (1967) started the use of intracortical microstimulation (ICMS) in motor research. The current levels were much lower than surface stimulations and frequency was quite high (330Hz). They stimulated various depths of the cat motor cortex and identified intermingled zones that facilitated or inhibited reflexes of individual foreleg muscle nerves. In the years to follow, ICMS quickly became a standard electrical stimulation technique for mapping motor cortex, with gradually evolving stimulation protocols (Kwan, Mackay, et al., 1978; Kwan, MacKay, et al., 1978; Cheney & Fetz, 1985). Using low frequency (15Hz) ICMS, Park and colleagues (2001, 2004) stimulated macaque M1 in/near layer 5 during reach-to-grasp task, to construct stimulus-triggered averages of electromyographic (EMG) activities of 24 forelimb muscles. This protocol minimized temporal summations of excitatory post-synaptic potentials (EPSPs), but still found overlapping representations at single sites, in the form of coactivations of muscle synergies (e.g., proximal and distal muscles together). A finer structure within the forelimb representation also manifested, which showed a horseshoe-shaped zone with proximal parts (shoulder and elbow) surrounding a transitory coactivation zones in the middle and distal parts (wrist, intrinsic hand and digits) at the core (Park et al., 2001; similar structure as found in Kwan, MacKay, et al., 1978).

Apart from invasive electrical stimulations, additional studies using single neuron recording, functional magnetic resonance imaging (fMRI) and magnetoencephalography (MEG) also confirmed the distributed nature of movement representation of different body parts (Cheyne et al., 1991; Sanes et al., 1995; Schieber & Hibbard, 1993).

To summarize, the spatial organization of motor cortex follows a crude whole-body sequence when zoomed out, but locally (e.g. for upper limb or digits) it can become hugely distributed/non-ordered. There is also significant divergence and convergence of outputs (Schieber, 2001). Underlying those complicated spatial representations, there are anatomical reasons like prevalent horizontal connections, intrinsic ambiguities of mapping a 3-dimensional body onto a 2-dimensional cortical sheet, and also functional reasons like synergistic needs (Schieber, 2001; Graziano & Aflalo, 2007).

Cortical spatial maps encoding functional properties of movement and posture

Maps discussed above focused on understanding of spatial organization in terms of body parts (including gross body parts, joints or muscles). Alternative means of segregation exists, which are related to the bigger question of what motor cortex actually encodes.

Instead of dividing into effector components, Graziano and colleagues (2002, 2005) proposed studying the spatial organization of the larger motor cortex using ethological action groups. Through longer durations of ICMS that were at behaviorally relevant timescale (500ms), they elicited movements including the following categories in macaques: climbing/leaping, reach-to-grasp, defense, hand-to-mouth, hand in lower space, manipulation in central space,

chewing/licking. Actions that were more isolated were represented in the more caudal part of motor cortex (from medial to lateral: hand in lower space, manipulation in central space, chewing/licking; this part of motor cortex is largely M1), while actions that were more integrative were represented in the more rostral part of motor cortex (from medial to lateral: climbing/leaping, reach-to-grasp, defense, hand-to-mouth). This trend of mapping the cortex with ethologically relevant actions gained momentum in studies with other species as well (e.g., human electrical stimulation study in Desmurget et al., 2014 and Huber et al., 2020; new world monkey electrical stimulation and chemical inhibition studies in Stepniewska et al., 2009, 2014; for a review, see Graziano, 2016).

In contrast, there is also a reductionist route, studying cortical spatial organizations related to kinematic parameters such as position, velocity and acceleration. Building on previous work (Amirikian & Georgopoulos, 2003), Georgopoulos and colleagues (2007) systematically mapped the preferred directions of multi-units in M1 proximal arm area as macaques performed free 3-D reaches. They discovered that sites tuned for similar directions were orderly organized in columns of roughly 30μm wide, with repeats in every ~240 μm. Within the distance of half a repeat, the further sites were from the center in the direction tangential to the layers, the more dissimilar their preferred directions were to the center. Similar local structures were found by Stark and colleagues (2009), who studied the spatial organization considering position, velocity and acceleration at the same time. One difficulty lies in the related natures of those variables, which was nicely dealt with by careful treatment of temporal correlation and large sample space (with scribbling and tracing tasks). They found that nearby single units / multi-units tended to encode for one movement parameter (in most cases, velocity), and that single units at the same electrodes tended to prefer similar values of the same parameter. Based on these results, they

suggested that motor cortical neurons accumulating within a spatial range of ~200 μm tended to encode a single parameter, notwithstanding a small portion of neurons related to other parameters. Nevertheless, no global gradients were reported in either Georgopoulos and colleagues (2007) or Stark and colleagues (2009). A global map encoding (final) arm and hand postures was discovered by Graziano and colleagues (2002). Using the 0.5s-long stimulations, they found systematic global arrangements of final positions of hand in 3-D, irrespective of starting positions or trajectories; with some overlap, the map represented different vertical and horizontal (left to right) final hand locations within different cortical regions.

Although M1 is known to modulate according to force and change of force (Evarts, 1968; Humphrey et al., 1970), little considerations seemed to have been explicitly given to the spatial organizations with those kinetic parameters.

Dynamic cortical spatial organization of the primary motor cortex

Long-term fluidity

Accumulated evidence indicated that spatial motor maps are far from static. In fact, spatial organizations discussed above should be understood as snapshots of an individual's ever-evolving motor maps. Various factors can result in the change in the spatial organization of maps, including developmental process, motor learning, and damage to the motor system. Those changes generally take place over a relatively long period of time.

Many mammals (especially altricial ones) were born only with the necessary motor skills for survival, leaving refined motor skills for postnatal development (Martin et al., 2005; Muir,

2000). In kittens, M1 motor representation started at postnatal day 45, with gradually more representation for distal forelimb joints and co-representation of multiple joints, together with lowering ICMS thresholds overall (Chakrabarty & Martin, 2000). In rats, motor cortex representation was detectable at postnatal day 13, with gradually lowered thresholds for short-duration ICMS (Young et al., 2012). Environmental enrichment could accelerate the development, and skilled forelimb training could increase its representation in the contralateral hemisphere (Young et al., 2012). Another study in rats (Singleton et al., 2021) used long-duration ICMS, and reported that simple forelimb movements could be evoked at postnatal day 25 but only in the caudal forelimb area; while complex movements could be evoked at day 30 in both caudal and rostral areas. Those complex movement representations were later reorganized, with 'grasp' and 'elevate' mostly in rostral area and all four complex movements ('grasp', 'elevate', 'advance' and 'retract') in caudal area. They also noted that experimental manipulations could change the representation—reduced inhibition accelerated its development and skilled reach learning increased 'grasp' and 'retract' representation in the contralateral hemisphere. In humans, reduced threshold in transcranial magnetic stimulation (TMS) needed for eliciting movement was also observed along development (Eyre et al., 2000).

Even after the critical period, skilled learning continues to shape the topographical arrangements of M1, reflecting M1's lifelong malleability. Nudo, Milliken and colleagues (1996) trained adult squirrel monkeys on two different tasks (pellet retrieval from small-diameter well vs forearm pronation/supination) and observed corresponding changes in the cortical representation: for pellet retrieval, the digit representations expanded while representation for wrist/forearm decreased; for forearm pronation/supination, the opposite happened. Interestingly, increased use per se without novel skill development doesn't modify representations. In the same lab setup,

Plautz and colleagues (2000) had adult squirrel monkeys retrieve pellets from a big-diameter well with matched activity levels, but observed no changes in the areas of distal forelimb representations. This signified that natural cortical spatial reorganization was driven by functional needs.

Lastly, damages to the motor system (including cortex, spinal cord and effectors), as well as the rehabilitation process also influences the cortical spatial map. With surface electrode stimulation as mapping technique, Glees and Cole (1950) reported that after lesion of the thumb representation area, trained monkeys had spontaneously reorganized their motor map to represent thumb in a surrounding area. In contrast, with short-duration ICMS as mapping technique, Nudo and Milliken (1996) showed that infarcts within the untrained monkeys' digits representation area caused widespread reduction in digits' representation, which gave room to enlarge adjacent wrist/forearm representation. These results point to the complications of (prior) motor experience and exact lesioning method, in addition to mapping technique. In terms of rehabilitation, studies with short-duration (Kleim et al., 2003) and long-duration ICMS (Ramanathan et al., 2006) as mapping techniques have both shown that motor map reorganization happens with physical rehabilitation after focal lesion in rats, and that the ability to re-express previously lost representation (either certain body parts or complex action sets) correlated with the extent of recovery. Apart from physical recruitment, direct electrical cortical stimulation could aid rehabilitation process (Brown et al., 2003; Kleim et al., 2003), accompanied with cortical remapping (Kleim et al., 2003).

Short-term dynamics

Regrettably, almost all research studying the fluidity of cortical spatial organization focused on changes that took place during a relatively long period of time (at least days, usually longer), with the assumption that maps are relatively stable within an experimental session. Studies looking into the flexible nature of encoding on a fast temporal scale were usually performed without explicit consideration of physical cortical space, or failed to discover meaningful spatial structures (Ben-Shaul et al., 2003, 2004; Churchland & Shenoy, 2007; Hatsopoulos et al., 2007; Rokni et al., 2007).

In light of this, in the first part of the thesis, I aim to describe the dynamical nature of cortical spatial organization in the primary motor cortex on a fast temporal scale: within single reaches. Given the highly distributed nature of movement encoding, the prevalent presence of divergence and convergence to outputs, as well as the ever-changing functional needs in orchestrating movements, I anticipate the relationship between M1 cortical sites and muscle activities to be constantly evolving during the execution of movements. Mapping out that relationship in space would help in understanding how stable spatial map characteristics (eg. proximal-distal gradient) are and provide the important spatial component in flexible movement encoding.

Presence and computational potentials of cortical propagation patterns

Certain aspects of neural signals can sometimes be spatio-temporally ordered on the cortical sheet, forming cortical propagation patterns. Such patterns can exist on different spatial scales, either within distinct local brain regions (mesoscopic) or globally in the whole brain

(macroscopic). Detecting propagation at different spatial scales requires different recording techniques— local patterns generally require more invasive techniques such as voltage-sensitive dyes (see Wu et al., 2008 for a review) and electrode arrays (eg. Rubino et al., 2006), while global patterns are usually detected with less invasive techniques such as electrocorticography (ECoG) (Alexander et al., 2013), electroencephalography (EEG) (Patten et al., 2012), magnetoencephalography (MEG) (Ribary et al., 1991) and functional magnetic resonance imaging (fMRI) (Lee et al., 2005).

Here I start by reviewing studies documenting propagation patterns in the primary motor cortex, then I briefly zoom out to review other relatively information-rich propagation patterns from across the brain. Next, I review theoretical works discussing mechanisms behind the formation of propagation patterns, as well as possible computations or processing that could be achieved with propagation patterns. Finally, I discuss potentials of discovering movement-specific propagation patterns in the primary motor cortex.

Propagation patterns in M1 and beyond

Using electrode arrays, propagation patterns have been detected in the phase and amplitude of the local field potentials. When phase is the object of interest, those patterns are often called waves.

In M1, the most well documented propagation patterns are in the beta frequency (roughly from 15 to 30Hz) of the LFP. In a typical reaching task, beta power generally increases during planning or steady muscle co-contraction period, exhibiting a peak in the spectrogram, which upon the onset of reach movement quickly drops (Baker et al., 1999; Sanes & Donoghue, 1993).

Rubino et al. (2006) found that around 50 to 200ms after the onset of Go cue, beta phase waves propagate across the upper limb area in the macaque M1 cortical sheet. The propagations primarily following one of two opposite directions in the rostro-caudal axis, with a mean propagation speed of 0.16m/s. These waves were potentially mediated by the predominant inter-area connectivity between dorsal premotor cortex (PMd) and M1 (Rubino et al., 2006); the bidirectionality could be a result of wave reflections at the boundary between M1 and area 3a (Takahashi et al., 2011). Additionally, the latency and amplitude of the evoked beta wave carry visual information regarding the target to reach, though neither propagation direction nor propagation speed were target-specific. Furthermore, those beta wave propagation directions corresponded to the prominent directions of sequential orchestrated single-neuron spiking activities in a subset of M1 neurons (Takahashi et al., 2015). This subset of neurons has narrow spike waveforms, which was likely composed of local inhibitory and excitatory pyramidal cells. This common directionality between beta wave and single-units reflected the same cortical spatial anisotropy in M1, which meant that propagation activity in the local field could provide a window to probe finer-scale local neural activity. In addition to non-human-primates, similar beta waves have also been found in the arm/hand area of M1 in a tetraplegic human subject (Takahashi et al., 2011), though the propagations were bidirectional following a different axis (medio-lateral axis), which might be due to a potentially reorganized somatotopy of M1 after trauma, or the fact that a chin cursor rather than own limb was used for performing the task.

This characteristic beta activity offered opportunities to probe propagating activities not only in the phase domain, but also in the amplitude. Using center-out reach tasks in macaques, Best et al. (2017) showed that trial-averaged beta envelopes of different electrodes in M1 do not attenuate synchronously upon movement initiation, but instead sequentially attenuated forming a

propagation pattern across the cortical sheet. In follow-up studies, Balasubramanian et al. (2020) extracted single-trial beta envelopes, and found that sequential attenuations followed the one of two directions along a rostral-caudal axis. Perturbations against the beta pattern delayed movement initiation, signifying the important role of natural beta attenuation propagation in movement initiation. Furthermore, this bimodal distribution of beta attenuation propagation directions was also found in macaque precision grip force task and tongue protrusion tasks, as well as in human isometric wrist extension task (Balasubramanian et al., 2022). Despite its universality, those beta amplitude propagations do not carry movement details, as the propagation direction and speed did not vary systematically with behavioral measurements other than reaction times.

Beyond M1, there was abundant documentation of propagation patterns elsewhere in the brain as well. Mesoscopically, in sensory areas such as primary visual and auditory cortices where there exist clear functional maps, it is common for propagating waves to initiate from the site of thalamic afferents and then propagate to surrounding areas when on a trial-averaged level (Song et al., 2006; Wu et al., 2008; Xu et al., 2007). However, those propagations are usually quite diffuse and possess radiating nature; and, on a single-trial basis there are huge variabilities (~85%) due to spontaneous patterns of cortical origin adding onto the evoked patterns, obscuring the evoked patterns (Arieli et al., 1996; Xu et al., 2007). Compared with primary sensory cortices, origin-specific propagations of this nature are harder to find in M1, perhaps due to the relatively crude spatial layout.

Macroscopically, propagation patterns have been found to be linked to general behavioral states at best, rather than detailed sensory qualities or memory content. For example, the macroscopic 8-12Hz alpha waves in human EEG travel primarily from frontal to occipital in the absence of

visual stimuli, while in the presence of visual stimuli, forward-travelling waves from occipital to frontal also emerge, likely supporting visual processing (Alamia & VanRullen, 2019; Pang et al., 2020). Similarly, 2-13Hz waves in human ECoG propagate from posterior to anterior during episodic memory encoding, and from anterior to posterior during retrieval (Mohan et al., 2022). In neither case was the detailed content being processing encoded in the propagation.

Formation of propagation patterns

Three mechanisms underlying phase-based propagation patterns have been proposed by Ermentrout and Kleinfeld (2001), all involving at least one cellular pacemaker. First of all, a single oscillator could drive excitations in nearby cortical regions at different distances, where closer sites are excited before further sites, creating waves. Propagation patterns happening in the cortical-thalamic network could be of this type (Bollimunta et al., 2011). Secondly, a burst of excitatory pulses could transmit along a chain of cortical locations, with relay-like successive activations. Even in normal awake brains with strong background activity, cortical locations along the way can be weakly entrained, sustaining the propagation of (sparse) waves (Muller et al., 2018). Thirdly, when considering all neurons as locally-coupled oscillators, the phase lag between neighboring oscillators could result in wave motion. In those mechanisms, spatial anisotropy in the network connectivity largely influences the directions of propagation (Takahashi et al., 2015).

Wu et al. (2008) proposed an additional mechanism without the need of cellular pacemakers, which involves the interactions of neuronal populations. Even though a stimulus can only generate one non-oscillatory propagating pulse in an excitable medium, two pulses colliding at a

particular timing and angle could give rise to spiral waves, which is self-sustained and fueled by the phase singularity. This mechanism operates at an emergent population level, in contrast to the local cellular level above.

Lastly, some additional mechanisms were proposed to explain the formation of forward and backward propagation patterns. As briefly mentioned above, structurally, reflections at area boundaries could result in reversions of wave directions (Takahashi et al., 2011; Xu et al., 2007). Perhaps more interestingly from a functional perspective, forward and backward waves could naturally arise during predictive coding schemes. Alamia and VanRullen (2019) built a multi-level network with biologically-plausible delays between layers, and used it to predict upcoming stimuli based on past stimuli. Hierarchically higher level makes predictions about the previous level and transmits its prediction back to it, in the form of inhibition; while the previous level evaluates the prediction and transmits the prediction error (i.e. residual, in the form of excitation) to the higher level, to help with adjusting its prediction for the next round. When the model was only fed with a time-varying input at the lowest layer, mimicking the reception of visual stimuli, network produced mostly forward waves in the alpha band; when the model was only fed with a time-varying prior at the highest layer, mimicking top-down expectations, network produced mostly feedback waves in the alpha band. Those simulation results largely reproduced macroscopic propagation patterns seen in human EEG data during visual processing and rest, indicating that those propagations patterns arise naturally when a biological network implements predictive encoding.

Computational potential of propagation patterns

Are propagation patterns merely by-products of brain functions, or are there relevant computational benefits as well? Despite little causal experimental evidence, some guiding hypotheses have been proposed.

First of all, propagation patterns could affect the firing probabilities of neurons along the way (Muller et al., 2018). Oscillations in membrane potential provide periodic deinactivation, which heighten the sensitivity of neurons to input changes (Ermentrout & Kleinfeld, 2001; Hopfield, 1995). When oscillation phases are spatially organized along cortical sheet, only part of the relevant neurons are deactivated, ensuring stable presence of responsive neurons. Furthermore, propagations might also be capable in helping organize a behaviorally/sensory relevant axis (Muller et al., 2018). For example, travelling waves could act as a 'bar code scanner', helping sensory areas scan incoming sensory stream for novel features (Ermentrout & Kleinfeld, 2001).

Secondly, propagation patterns could help providing contextual information for information processing. In V1, waves originating from initial retinotopic locations broadly influence neurons a few millimeters away, traversing over different ocular dominance columns and orientation maps (Muller et al., 2018). This type of broad activity could be relevant to the formation of non-traditional receptive fields. In cases where multiple stimuli were present in the sensory stream, waves can label simultaneously perceived features with a unique phase, which could help with object segmentation and categorization (Ermentrout & Kleinfeld, 2001). Furthermore, we can consider the brain as a chaotic system. A useful property for waves in chaotic systems was temporal reversibility, which implied that the recent history of wave could be backed out with sufficient knowledge of the dynamical system. For example, when a wave travels through V1 cortical sheet, both the stimulus position and recent past might have been encoded within the

distributed spatio-temporal pattern, which could help with processing dynamic scenes (Muller et al., 2018).

Thirdly, when considering idealistic dense waves under the framework of reaction-diffusion systems, many interesting computation capabilities manifest. In small spiking networks with relatively few synaptic connections, a travelling excitation state can be considered as a packet of information. Collision-based interactions between waves can thus perform logic operations like AND and XOR, through the merging and annihilation of two waves respectively (Adamatzky et al., 2005; Muller et al., 2018). More complex wave-based computations such as pattern recognition could also be realized in simulations through position learning based on spike-timing dependence (Highland, 2018, 2021). Those idealistic situations are hard to achieve in the brain and significant adjustment will be needed to address real scenarios.

Lastly, Wu et al. (2008) proposed that propagation patterns in the cortex could be considered as emergent behavior of neuronal population, capable of exhibiting 'swarm intelligence' as we see in swarms of animals with local interaction rules. Given that various brain functions such as sensory, motor and cognitive functions require no 'conductor neuron', it is possible that some computations could happen at this emergent level rather than on the level of isolated individual neurons. This idea might seem like a long shot, but it is helpful to consider cortical propagation phenomenon in a broader context of self-organizing systems of various scales, in light of their analogous properties.

To summarize, despite the prevalence of spatio-temporal patterns in the brain including M1, there is little experimental evidence of those patterns encoding exact behaviorally relevant

details. This is in stark contrast to the various computational potentials of propagation patterns from a theoretic perspective. Thus, in the second part of my dissertation, I will probe for new spatio-temporal patterns in M1 that might bear more computational relevance such as detailed kinematics. Given the anisotropic cortical connectivity, gross somatotopic gradient and spatially-organized neuronal interactions in M1, I anticipate that such patterns should exist, especially when information-rich neural signals are considered.

Information-rich high-gamma signal in motor cortex

The broad high-frequency band (>100Hz, also called the 'high-gamma' band) in the extracellular local field potential is a broad-band signal with no clear peak in the spectrum, known as a useful 'proxy' for neuronal spike outputs (Buzsáki et al., 2012). Here I review the various frequency definitions of the high-gamma signals, its spatial reach and relationship with unit activity, as well as decoding applications. I will primarily draw on evidence from the motor cortex, unless no such literature is found regarding the particular issue. I will not discuss real high-frequency oscillations such as those ripple oscillations (>200Hz) in the hippocampus (Buzsáki et al., 1992; Ylinen et al., 1995), given the vastly different nature of the signal.

Frequency definition of high-gamma signal

In contrast to the other classical lower frequency bands, there is no unanimous definition of 'high-gamma' band. Anything above the traditional gamma frequency has been considered 'high-gamma' by various groups (e.g. 63-200Hz as in Rickert et al., 2005; 75-150Hz as in Rich & Wallis, 2017; 102-238Hz as in Ray & Maunsell, 2011; 100-200Hz as in Zhuang et al., 2010;

70-300Hz as in Flint et al., 2012; 100-300Hz as in Perel et al., 2015). Still higher frequency bands have also been singled out and investigated (e.g. 200-400Hz as in Zhuang et al., 2010 and in Gallego-Carracedo et al., 2022; 250-500Hz as in Ray & Maunsell, 2011); sometimes they were referred to as 'broad-band high frequency', sometimes without specific names other than the frequency. From here on we loosely refer to those higher frequency bands as high-gamma as well.

Origin of high-gamma signal and similarity with spiking activity

Generally speaking, spiking events, synaptic inputs, and volume conduction from remote sources all contribute to the local field potential (Pesaran et al., 2018). The high-frequency range, though, is less affected by the volume conduction effect. Some considered it to be dominated by spiking activities (Pesaran et al., 2018), while others thought it could be a combination of action potentials and other network changes that led up to the spiking activities (incl. synaptic events), which would require intracellular recordings with channel blockers to precisely isolate (Ray & Maunsell, 2011).

How similar are the high-gamma signals and spiking activities? In monkey primary visual cortex, Ray and Maunsell (2011) compared the temporal traces of LFP of individual frequency bands averaged over the same stimulus presentations with average multi-unit firing rate over the same stimulus. They found that the higher the LFP frequency, the higher the correlation, reaching a peak correlation around 0.9 for 250-500Hz. Furthermore, even after controlling for stimulus presentation, (noise) correlation was also highest in the same frequency band, reaching ~0.3. This indicated that the co-variation between high-frequency LFP and thresholded multi-unit activity was resulted from more than just common stimulus modulations. In the primary

motor cortex, Perel et al. (2015) found that the kinematic encoding in the high frequency LFPs (100-300Hz) were more similar to thresholded multi-unit activities, than sorted single unit activities. Also in the primary motor cortex, Gallego-Carracedo et al. (2022) compared the latent dynamics (in the form of principal components) from LFP and from single units. They found that when allowing for linear combinations (with canonical correlation analysis), among all band-limited signals, 200-400Hz latent dynamics had the best alignment with single unit latent dynamics during movement preparation and execution. In summary, there were decent resemblance between high-gamma and unit activities, especially with multi-unit signals.

Spatial resolution of high-gamma signal

A related question is how localized those high-gamma signals are. This depends on the exact location, state and correlations of synaptic inputs, usually on a scale of a few hundred μm in the lateral direction of cortical sheet (Kajikawa & Schroeder, 2011; Katzner et al., 2009; Liu & Newsome, 2006). Using biologically plausible simulations, Leski et al. (2013) systematically showed that with higher frequency LFPs, the spatial reach (defined as 95% of total root mean square amplitude) became smaller, because (1) single-neuron LFP contribution decayed faster with distance for higher frequency components due to differential intrinsic dendritic filtering and (2) correlated synaptic input resulted in LFP correlations to a lesser extent for higher frequency components. For example, with simulated layer-5 (or layer-3) cells with uncorrelated basal synaptic input, the spatial reach for soma-level LFP near 0Hz, 100Hz, 200Hz and 400Hz was respectively around 140, 120, 90, 85μm (or around 120, 100, 85, 75μm). With correlated input (correlation coefficient = 0.1), spatial reach for simulated layer-5 (or layer-3) cells at the same frequencies increased to around 850, 750, 500, 200μm (or around 620, 400, 150, 80μm). Similar

conclusions were established experimentally in the primary motor cortex. Using a center-out task, Perel et al. (2015) also found that LFP *noise* correlation between electrodes were lower and decayed faster with distance for higher frequencies compared to lower frequencies, arriving at less than 0.2 for >200Hz at farther than 400μm away; LFP *signal* correlation between electrodes were also much lower for higher frequencies than lower frequencies (below 0.6 for >200Hz), but signal correlation was hardly distance-dependent (for both high and low frequencies).

In contrast, unit activities are more localized. Spikes generated at soma with a diameter of 10-30 μm would have its amplitude decayed by about 90% when recording from about 65 μm away (Gray et al., 1995; Rall, 1962). MUAs (without spike sorting) are thought to reflect aggregated spikes from a radius of 140~300 μm (Gold et al., 2006; Holt & Koch, 1999). In Perel et al. (2015), the correlations of thresholded MUA were smaller than the highest-frequency high-gamma at the same distances.

Thus, in theory high-gamma LFP should provide moderate spatial integration between low-frequency LFP and unit activity. Indeed, Rich and Wallis (2017) found that high-gamma activity possessed a spatial organization that was more ordered than unit activities, despite the spatial heterogeneity of encoding variables and valences in neuron populations in the orbitofrontal cortex. In our context of cortical array recording with a standard inter-electrode spacing of 400 μm, high-gamma's spatial integration is at a similar scale to inter-electrode spacing, which should offer an ideal spatial resolution for the manifestation of smooth spatial characteristics if existent.

Decoding applications of high-gamma signal

High-gamma band signal in the primary motor cortex has proved to offer good decoding performance, both in offline open-loop analyses and in real-time closed-loop applications.

Offline-wise, Zhuang et al. (2010) looked at reach-to-grasp behaviors in able-bodied monkeys, and found that the 100-200Hz and 200-400Hz bands carried the most mutual information with 3D reach-and-grasp kinematics among all frequency bands considered. The 200-400Hz band additionally offered the best reconstruction of reach kinematics, grasp aperture and grasp velocity when tested with Kalman filter based decoders, reaching a performance almost as good as from single units. Bansal et al. (2012) also found that the 200-400Hz frequency band offered the best encoding of 3D reach kinematics and grasp aperture among all LFP bands looked at in M1 and ventral premotor (PMv), which added to the robustness of decoders built with single-units. Not only was high-frequency LFP useful in predicting kinematics, it was also capable of predicting muscle activities. With a Wiener cascade model, Flint, Ethier, et al. (2012) showed that the power in 200-300Hz LFP predicted EMG activity in proximal and distal muscles better than lower frequency bands, while monkeys performed reach-to-grasp and isometric wrist force tasks. The combined LFP performance (integrating all frequency bands) at the best lag was very similar to the performance of spikes at the best lag. Lastly, Perge et al. (2014) examined open-loop decoding performance while tetraplegic patients performed a four-direction center-out-and-back task. They confirmed that the 200-400Hz band performed best among LFP bands in the prediction of movement direction and endpoint velocity across an one-year period, while combined LFP attained similar performance as spikes.

In addition, there were some closed-loop applications. Flint et al. (2013) obtained LFP and thresholded multi-unit activity while monkeys performed a continuous reach task, then built biomimetic controllers based on Wiener cascade model, and tracked their performance in

controlling a BMI for over a year without retraining. They found that the combined LFP decoder including the high frequency band (200-300Hz) retained or improved their high-level performance for nearly a year, exceeding the longevity of multi-units which was a little over half a year. Although initially multi-units performed a little better than LFP on average, LFP was able to close the gap as time went by. Importantly, those closed-loop performances exceeded offline performances built from the corresponding signal types, indicating that monkeys were able to make active adaptations in the closed-loop setups with the high-gamma band just like with multi-units. Another closed-loop application by Milekovic et al. (2018) was somewhat special. They selected features from LFP signals (including frequencies as high as 350Hz) from the arm area of dominant precentral gyrus in a patient with locked-in syndrome and another patient with tetraplegia, from which they built a letter-entry communication BMI through regularized linear discriminant analysis. This BMI enabled a spelling rate of 3.07~6.88 correct characters/minute without recalibration, maintaining the performance throughout the 76~138 days the study lasted. Different from Flint et al. (2013), Milekovic et al. (2018) found that open-loop decoding had no worse performance compared with the closed-loop decoding in this setup, leading to the conclusion that even without active adaptive control from the patient side, this population-level approach utilizing informative LFP signals in M1 could make reliable BMIs.

Why does high-gamma activity offer comparable and complementary decoding performance to unit activities? In addition to the substantial signal similarity between high-gamma and unit activity discussed above, other reasons also contributed. First of all, practically both single-unit activity and multi-unit activity depend on some sort of thresholding. Spikes with amplitudes that are too small to cross threshold or get isolated would not appear in the resolvable unit activity, but could still contribute to the high-gamma band power (Ray & Maunsell, 2011). Secondly,

spiking activity recorded by electrodes are biased towards larger cells, which are more likely to connect with other brain areas, reflecting the output of a brain region (Mitzdorf, 1985). This is in contrast to components of LFP which likely largely reflect the input to an area and the local processing therein (Andersen et al., 2004). Thirdly, high-gamma reflects average population activity, thus can be less noisy especially when nearby neurons have similar response properties (Andersen et al., 2004). Fourthly, when there are small extracellular voltage fluctuations which only affect firing rate of any particular neuron minimally and probabilistically, aggregate high-gamma activity could be affected to a larger extent (Rich & Wallis, 2017). Lastly, over an extended period of time, single-unit activity can be unstable in terms of firing rate and amplitude, due to changes in electrode impedance and array location; thus, fixed decoders based solely on single-unit activity usually have compromised decoding performance longitudinally (Perge et al., 2013). On the other hand, population-based LFP signal such as high-gamma is stable over time regardless of the ability to record spikes concurrently at the same channels, thus capable of mitigating loss in spiking activity for decoding purposes (Flint, Lindberg, et al., 2012; Rupp et al., 2014).

To summarize, the high-gamma band, especially the 200-400Hz frequency band, stands out among LFP signals in terms of localization, similarity with unit activity and decoding performance. Compared to unit activities and lower-frequency LFPs, it offers an intermediate spatial resolution ideal for probing mesoscopic cortical organizations in extracellular recording. Thus, for both parts of the thesis, I will primarily use the 200-400Hz band LFP as the neural signal.

References

Adamatzky, A., Costello, B. D. L., & Asai, T. (2005). *Reaction-diffusion computers*. Elsevier.

Alamia, A., & VanRullen, R. (2019). Alpha oscillations and traveling waves: Signatures of predictive coding? *PLoS Biology*, *17*(10), 1–26. https://doi.org/10.1371/journal.pbio.3000487

Alexander, D. M., Jurica, P., Trengove, C., Nikolaev, A. R., Gepshtein, S., Zvyagintsev, M., Mathiak, K., Schulze-Bonhage, A., Ruescher, J., Ball, T., & van Leeuwen, C. (2013). Traveling waves and trial averaging: The nature of single-trial and averaged brain responses in large-scale cortical signals. *NeuroImage*, *73*, 95–112. https://doi.org/10.1016/j.neuroimage.2013.01.016

Amirikian, B., & Georgopoulos, A. P. (2003). Modular organization of directionally tuned cells in the motor cortex: Is there a short-range order? *Proceedings of the National Academy of Sciences of the United States of America*, *100*(21), 12474–12479. https://doi.org/10.1073/pnas.2037719100

Andersen, R. A., Musallam, S., & Pesaran, B. (2004). Selecting the signals for a brain-machine interface. *Current Opinion in Neurobiology*, *14*(6), 720–726. https://doi.org/10.1016/j.conb.2004.10.005

Arieli, A., Sterkin, A., Grinvald, A., & Aertsen, A. (1996). Dynamics of ongoing activity: Explanation of the large variability in evoked cortical responses. *Science*, *273*(5283), 1868–1871. https://doi.org/10.1126/science.273.5283.1868

Asanuma, H., & Sakata, H. (1967). Functional Organization of a Cortical Efferent System Examined with Focal Depth Stimulation in Cats. *Journal of Neurophysiology*, *30*(1), 35–54. https://doi.org/10.1152/jn.1967.30.1.35

Baker, S. N., Kilner, J. M., Pinches, E. M., & Lemon, R. N. (1999). The role of synchrony and oscillations in the motor output. *Experimental Brain Research*, *128*(1–2), 109–117. https://doi.org/10.1007/s002210050825

Balasubramanian, K., Arce-McShane, F. I., Dekleva, B. M., Collinger, J. L., & Hatsopoulos, N. G. (2022). *Propagating motor cortical patterns of excitability are ubiquitous across human and non-human primate movement initiation*. https://papers.ssrn.com/sol3/papers.cfm?abstract_id=4108216

Balasubramanian, K., Papadourakis, V., Liang, W., Takahashi, K., Best, M. D., Suminski, A. J., & Hatsopoulos, N. G. (2020). Propagating Motor Cortical Dynamics Facilitate Movement Initiation. *Neuron*, *106*(3), 526-536.e4. https://doi.org/10.1016/j.neuron.2020.02.011

Bansal, A. K., Truccolo, W., Vargas-Irwin, C. E., & Donoghue, J. P. (2012). Decoding 3D reach and grasp from hybrid signals in motor and premotor cortices: Spikes, multiunit activity, and local field potentials. *Journal of Neurophysiology*, *107*(5), 1337–1355. https://doi.org/10.1152/jn.00781.2011

Ben-Shaul, Y., Drori, R., Asher, I., Stark, E., Nadasdy, Z., & Abeles, M. (2004). Neuronal Activity in Motor Cortical Areas Reflects the Sequential Context of Movement. *Journal of*

Neurophysiology, *91*(4), 1748–1762. https://doi.org/10.1152/jn.00957.2003

Ben-Shaul, Y., Stark, E., Asher, I., Drori, R., Nadasdy, Z., & Abeles, M. (2003). Dynamical organization of directional tuning in the primate premotor and primary motor cortex. *Journal of Neurophysiology*, *89*(2), 1136–1142. https://doi.org/10.1152/jn.00364.2002

Best, M. D., Suminski, A. J., Takahashi, K., Brown, K. A., & Hatsopoulos, N. G. (2017). Spatio-Temporal Patterning in Primary Motor Cortex at Movement Onset. *Cerebral Cortex (New York, N.Y. : 1991)*, *27*(2), 1491–1500. https://doi.org/10.1093/cercor/bhv327

Bollimunta, A., Mo, J., Schroeder, C. E., & Ding, M. (2011). Neuronal mechanisms and attentional modulation of corticothalamic alpha oscillations. *Journal of Neuroscience*, *31*(13), 4935–4943. https://doi.org/10.1523/JNEUROSCI.5580-10.2011

Brown, J. A., Lutsep, H., Cramer, S. C., & Weinand, M. (2003). Motor cortex stimulation for enhancement of recovery after stroke: Case report. *Neurological Research*, *25*(8), 815–818. https://doi.org/10.1179/016164103771953907

Buzsáki, G., Anastassiou, C. A., & Koch, C. (2012). The origin of extracellular fields and currents-EEG, ECoG, LFP and spikes. *Nature Reviews Neuroscience*, *13*(6), 407–420. https://doi.org/10.1038/nrn3241

Buzsáki, G., Horvath, Z., Urioste, R., Hetke, J., & Wise, K. (1992). High-frequency network oscillation in the hippocampus. *Science*, *256*(5059), 1025–1027.

Chakrabarty, S., & Martin, J. H. (2000). Postnatal development of the motor representation in primary motor cortex. *Journal of Neurophysiology*, *84*(5), 2582–2594. https://doi.org/10.1152/jn.2000.84.5.2582

Cheney, P. D., & Fetz, E. E. (1985). Comparable patterns of muscle facilitation evoked by individual corticomotoneuronal (CM) cells and by single intracortical microstimuli in primates: Evidence for functional groups of CM cells. *Journal of Neurophysiology*, *53*(3), 786–804. https://doi.org/10.1152/jn.1985.53.3.786

Cheyne, D., Kristeva, R., & Deecke, L. (1991). Homuncular organization of human motor cortex as indicated by neuromagnetic recordings. *Neuroscience Letters*, *122*(1), 17–20. https://doi.org/10.1016/0304-3940(91)90182-S

Churchland, M. M., & Shenoy, K. V. (2007). Temporal complexity and heterogeneity of single-neuron activity in premotor and motor cortex. *Journal of Neurophysiology*, *97*(6), 4235–4257. https://doi.org/10.1152/jn.00095.2007

Desmurget, M., Richard, N., Harquel, S., Baraduc, P., Szathmari, A., Mottolese, C., & Sirigu, A. (2014). Neural representations of ethologically relevant hand/mouth synergies in the human precentral gyrus. *Proceedings of the National Academy of Sciences of the United States of America*, *111*(15), 5718–5722. https://doi.org/10.1073/pnas.1321909111

Ermentrout, G. B., & Kleinfeld, D. (2001). Traveling Electrical Waves in Cortex. *Neuron*, *29*(1), 33–44. https://doi.org/10.1016/s0896-6273(01)00178-7

Evarts, E. V. (1968). Relation of pyramidal tract activity to force exerted during voluntary movement. *Journal of Neurophysiology*, *31*(1), 14–27.

https://doi.org/10.1152/jn.1968.31.1.14

Eyre, J. A., Miller, S., Clowry, G. J., Conway, E. A., & Watts, C. (2000). Functional corticospinal projections are established prenatally in the human foetus permitting involvement in the development of spinal motor centres. *Brain*, *123*(1), 51–64. https://doi.org/10.1093/brain/123.1.51

Ferrier, D. (1886). *The functions of the brain*. Smith, Elder.

Flint, R. D., Ethier, C., Oby, E. R., Miller, L. E., & Slutzky, M. W. (2012). Local field potentials allow accurate decoding of muscle activity. *Journal of Neurophysiology*, *108*(1), 18–24. https://doi.org/10.1152/jn.00832.2011

Flint, R. D., Lindberg, E. W., Jordan, L. R., Miller, L. E., & Slutzky, M. W. (2012). Accurate decoding of reaching movements from field potentials in the absence of spikes. *Journal of Neural Engineering*, *9*(4). https://doi.org/10.1088/1741-2560/9/4/046006

Flint, R. D., Wright, Z. A., Scheid, M. R., & Slutzky, M. W. (2013). Long term, stable brain machine interface performance using local field potentials and multiunit spikes. *Journal of Neural Engineering*, *10*(5). https://doi.org/10.1088/1741-2560/10/5/056005

Fritsch, G., & Hitzig, E. (1870). On the electrical excitability of the cerebrum. In von Bonin G. *Some Papers on the Cerebral Cortex. Springfield, IL: Charles C Thomas*.

Gallego-Carracedo, C., Perich, M. G., Chowdhury, R. H., Miller, L. E., & Gallego, J. Á. (2022). Local field potentials reflect cortical population dynamics in a region-specific and frequency-dependent manner. *ELife*, *11*, 1–24. https://doi.org/10.7554/eLife.73155

Glees, P., & Cole, J. (1950). recovery of skilled motor functions after small repeated lesions of motor cortex in macaque. *Journal of Neurophysiology*.

Gold, C., Henze, D. A., Koch, C., & Buzsáki, G. (2006). On the origin of the extracellular action potential waveform: A modeling study. *Journal of Neurophysiology*, *95*(5), 3113–3128. https://doi.org/10.1152/jn.00979.2005

Gray, C. M., Maldonado, P. E., Wilson, M., & McNaughton, B. (1995). Tetrodes markedly improve the reliability and yield of multiple single-unit isolation from multi-unit recordings in cat striate cortex. *Journal of Neuroscience Methods*, *63*(1–2), 43–54. https://doi.org/10.1016/0165-0270(95)00085-2

Graziano, M. S. A. (2016). Ethological Action Maps: A Paradigm Shift for the Motor Cortex. *Trends in Cognitive Sciences*, *20*(2), 121–132. https://doi.org/10.1016/j.tics.2015.10.008

Graziano, M. S. A., & Aflalo, T. N. (2007). Mapping behavioral repertoire onto the cortex. *Neuron*, *56*(2), 239–251. https://doi.org/10.1016/j.neuron.2007.09.013

Graziano, M. S. A., Aflalo, T. N. S., & Cooke, D. F. (2005). Arm movements evoked by electrical stimulation in the motor cortex of monkeys. *Journal of Neurophysiology*, *94*(6), 4209–4223. https://doi.org/10.1152/jn.01303.2004

Graziano, M. S. A., Taylor, C. S. R., & Moore, T. (2002). Complex movements evoked by microstimulation of precentral cortex. *Neuron*, *34*(5), 841–851.

https://doi.org/10.1016/S0896-6273(02)00698-0

Hatsopoulos, N. G., Xu, Q., & Amit, Y. (2007). Encoding of movement fragments in the motor cortex. *Journal of Neuroscience*, *27*(19), 5105–5114. https://doi.org/10.1523/JNEUROSCI.3570-06.2007

Highland, F. (2018). Unsupervised learning of polychronous wavefront computation configurations for pattern recognition. *Procedia Computer Science*, *140*, 134–143. https://doi.org/10.1016/j.procs.2018.10.311

Highland, F. (2021). A Theoretical Basis for the Application of Neuromorphic Concepts to Polychronous Wavefront Computation. *Procedia Computer Science*, *185*(June), 353–360. https://doi.org/10.1016/j.procs.2021.05.036

Holt, G. R., & Koch, C. (1999). Electrical interactions via the extracellular potential near cell bodies. *Journal of Computational Neuroscience*, *184*, 169–184.

Hopfield, J. J. (1995). Pattern recognition computation using action potential timing for stimulus representation. *Nature*, *376*(6535), 33–36.

Huber, L., Finn, E. S., Handwerker, D. A., Bönstrup, M., Glen, D. R., Kashyap, S., Ivanov, D., Petridou, N., Marrett, S., Goense, J., Poser, B. A., & Bandettini, P. A. (2020). Sub-millimeter fMRI reveals multiple topographical digit representations that form action maps in human motor cortex. *NeuroImage*, *208*(December 2019). https://doi.org/10.1016/j.neuroimage.2019.116463

Humphrey, D. R., Schmidt, E. M., & Thompson, W. D. (1970). Predicting Measures of Motor Performance from Multiple Cortical Spike Trains. *Science*, *170*(3959), 758–762.

Jackson, J. H. (1867). Remarks on the disorderly movements of chorea and convulsion, and on localisation. *Med Times Gazette*, *2*, 669–670.

Kajikawa, Y., & Schroeder, C. E. (2011). How local is the local field potential? *Neuron*, *72*(5), 847–858. https://doi.org/10.1016/j.neuron.2011.09.029

Katzner, S., Nauhaus, I., Benucci, A., Bonin, V., Ringach, D. L., & Carandini, M. (2009). Local Origin of Field Potentials in Visual Cortex. *Neuron*, *61*(1), 35–41. https://doi.org/10.1016/j.neuron.2008.11.016

Kleim, J. A., Bruneau, R., VandenBerg, P., MacDonald, E., Mulrooney, R., & Pocock, D. (2003). Motor cortex stimulation enhances motor recovery and reduces peri-infarct dysfunction following ischemic insult. *Neurological Research*, *25*(8), 789–793. https://doi.org/10.1179/016164103771953862

Kwan, H. C., Mackay, W. A., Murphy, J. T., & Wong, Y. C. (1978). An intracortical microstimulation study of output organization in precentral cortex of awake primates. *Journal de Physiologie*, *74*(3), 231–233.

Kwan, H. C., MacKay, W. A., Murphy, J. T., & Wong, Y. C. (1978). Spatial organization of precentral cortex in awake primates. II. Motor outputs. *Journal of Neurophysiology*, *41*(5), 1120–1131.

Lee, S. H., Blake, R., & Heeger, D. J. (2005). Traveling waves of activity in primary visual cortex during binocular rivalry. *Nature Neuroscience*, *8*(1), 22–23. https://doi.org/10.1038/nn1365

Leski, S., Lindén, H., Tetzlaff, T., Pettersen, K. H., & Einevoll, G. T. (2013). Frequency Dependence of Signal Power and Spatial Reach of the Local Field Potential. *PLoS Computational Biology*, *9*(7). https://doi.org/10.1371/journal.pcbi.1003137

Liu, J., & Newsome, W. T. (2006). Local field potential in cortical area MT: Stimulus tuning and behavioral correlations. *Journal of Neuroscience*, *26*(30), 7779–7790. https://doi.org/10.1523/JNEUROSCI.5052-05.2006

Martin, J. H., Engber, D., & Meng, Z. (2005). Effect of forelimb use on postnatal development of the forelimb motor representation in primary motor cortex of the cat. *Journal of Neurophysiology*, *93*(5), 2822–2831. https://doi.org/10.1152/jn.01060.2004

Milekovic, T., Sarma, A. A., Bacher, D., Simeral, J. D., Saab, J., Pandarinath, C., Sorice, B. L., Blabe, C., Oakley, E. M., Tringale, K. R., Eskandar, E., Cash, S. S., Henderson, J. M., Shenoy, K. V., Donoghue, J. P., & Hochberg, L. R. (2018). Stable long-term BCI-enabled communication in ALS and locked-in syndrome using LFP signals. *Journal of Neurophysiology*, *120*(1), 343–360. https://doi.org/10.1152/jn.00493.2017

Mitzdorf, U. (1985). Current source-density method and application in cat cerebral cortex: Investigation of evoked potentials and EEG phenomena. *Physiological Reviews*, *65*(1), 37–100. https://doi.org/10.1152/physrev.1985.65.1.37

Mohan, U. R., Zhang, H., & Jacobs, J. (2022). The direction and timing of theta and alpha traveling waves modulate human memory processing. *BioRxiv*, 2022.02.07.479466. https://www.biorxiv.org/content/10.1101/2022.02.07.479466v1%0Ahttps://www.biorxiv.org/content/10.1101/2022.02.07.479466v1.abstract

Muir, G. D. (2000). Early ontogeny of locomotor behaviour: A comparison between altricial and precocial animals. *Brain Research Bulletin*, *53*(5), 719–726. https://doi.org/10.1016/S0361-9230(00)00404-4

Muller, L., Chavane, F., Reynolds, J., & Sejnowski, T. J. (2018). Cortical travelling waves: Mechanisms and computational principles. *Nature Reviews Neuroscience*, *19*(5), 255–268. https://doi.org/10.1038/nrn.2018.20

Nudo, R. J., Milliken, G. W., Jenkins, W. M., & Merzenich, M. M. (1996). *Use-Dependent Primary Motor Alterations of Movement Representations In Primary Motor Cortex of Adult Squirrel Monkeys*. *16*(2), 785–807.

Nudo, Randolph J., & Milliken, G. W. (1996). Reorganization of movement representations in primary motor cortex following focal ischemic infarcts in adult squirrel monkeys. *Journal of Neurophysiology*, *75*(5), 2144–2149. https://doi.org/10.1152/jn.1996.75.5.2144

Pang, Z., Alamia, A., & Vanrullen, R. (2020). Turning the stimulus on and off changes the direction of α traveling waves. *ENeuro*, *7*(6), 1–11. https://doi.org/10.1523/ENEURO.0218-20.2020

Park, M. C., Belhaj-Saïf, A., & Cheney, P. D. (2004). Properties of primary motor cortex output

to forelimb muscles in rhesus macaques. *Journal of Neurophysiology*, *92*(5), 2968–2984.

Park, M. C., Belhaj-Saïf, A., Gordon, M., & Cheney, P. D. (2001). Consistent features in the forelimb representation of primary motor cortex in rhesus macaques. *Journal of Neuroscience*, *21*(8), 2784–2792. https://doi.org/10.1523/jneurosci.21-08-02784.2001

Patten, T. M., Rennie, C. J., Robinson, P. A., & Gong, P. (2012). Human cortical traveling waves: Dynamical properties and correlations with responses. *PLoS ONE*, *7*(6), 1–10. https://doi.org/10.1371/journal.pone.0038392

Penfield, W., & Boldrey, E. (1937). Somatic Motor and Sensory Representation in Man. *Brain*, 389–443.

Penfield, W., & Rasmussen, T. (1950). *The cerebral cortex of man; a clinical study of localization of function.*

Perel, S., Sadtler, P. T., Oby, E. R., Ryu, S. I., Tyler-Kabara, E. C., Batista, A. P., & Chase, S. M. (2015). Single-unit activity, threshold crossings, and local field potentials in motor cortex differentially encode reach kinematics. *Journal of Neurophysiology*, *114*(3), 1500–1512. https://doi.org/10.1152/jn.00293.2014

Perge, J. A., Homer, M. L., Malik, W. Q., Cash, S., Eskandar, E., Friehs, G., Donoghue, J. P., & Hochberg, L. R. (2013). Intra-day signal instabilities affect decoding performance in an intracortical neural interface system. *Journal of Neural Engineering*, *10*(3). https://doi.org/10.1088/1741-2560/10/3/036004

Perge, J. A., Zhang, S., Malik, W. Q., Homer, M. L., Cash, S., Friehs, G., Eskandar, E. N., Donoghue, J. P., & Hochberg, L. R. (2014). Reliability of directional information in unsorted spikes and local field potentials recorded in human motor cortex. *Journal of Neural Engineering*, *11*(4). https://doi.org/10.1088/1741-2560/11/4/046007

Pesaran, B., Vinck, M., Einevoll, G. T., Sirota, A., Fries, P., Siegel, M., Truccolo, W., Schroeder, C. E., & Srinivasan, R. (2018). Investigating large-scale brain dynamics using field potential recordings: Analysis and interpretation. *Nature Neuroscience*, *21*(7), 903–919. https://doi.org/10.1038/s41593-018-0171-8

Plautz, E. J., Milliken, G. W., & Nudo, R. J. (2000). Effects of repetitive motor training on movement representations in adult squirrel monkeys: Role of use versus learning. *Neurobiology of Learning and Memory*, *74*(1), 27–55. https://doi.org/10.1006/nlme.1999.3934

Rall, W. (1962). Electrophysiology of a Dendritic Neuron Model. *Biophysical Journal*, *2*(2), 145–167. https://doi.org/10.1016/S0006-3495(62)86953-7

Ramanathan, D., Conner, J. M., & Tuszynski, M. H. (2006). A form of motor cortical plasticity that correlates with recovery of function after brain injury. *Proceedings of the National Academy of Sciences of the United States of America*, *103*(30), 11370–11375. https://doi.org/10.1073/pnas.0601065103

Ray, S., & Maunsell, J. H. R. (2011). Different origins of gamma rhythm and high-gamma activity in macaque visual cortex. *PLoS Biology*, *9*(4). https://doi.org/10.1371/journal.pbio.1000610

Ribary, U., Ioannides, A. A., Singh, K. D., Hasson, R., Bolton, J. P. R., Lado, F., Mogilner, A., & Llinás, R. (1991). Magnetic field tomography of coherent thalamocortical 40-Hz oscillations in humans. *Proceedings of the National Academy of Sciences of the United States of America*, *88*(24), 11037–11041. https://doi.org/10.1073/pnas.88.24.11037

Rich, E. L., & Wallis, J. D. (2017). Spatiotemporal dynamics of information encoding revealed in orbitofrontal high-gamma. *Nature Communications*, *8*(1), 1–13. https://doi.org/10.1038/s41467-017-01253-5

Rickert, J., Cardoso De Oliveira, S., Vaadia, E., Aertsen, A., Rotter, S., & Mehring, G. (2005). Encoding of movement direction in different frequency ranges of motor cortical local field potentials. *Journal of Neuroscience*, *25*(39), 8815–8824. https://doi.org/10.1523/JNEUROSCI.0816-05.2005

Rokni, U., Richardson, A. G., Bizzi, E., & Seung, H. S. (2007). Motor Learning with Unstable Neural Representations. *Neuron*, *54*(4), 653–666. https://doi.org/10.1016/j.neuron.2007.04.030

Rubino, D., Robbins, K. A., & Hatsopoulos, N. G. (2006). Propagating waves mediate information transfer in the motor cortex. *Nature Neuroscience*, *9*(12), 1549–1557. https://doi.org/10.1038/nn1802

Rupp, K. M., Schieber, M. H., & Thakor, N. V. (2014). Local field potentials mitigate decline in motor decoding performance caused by loss of spiking units. *2014 36th Annual International Conference of the IEEE Engineering in Medicine and Biology Society, EMBC 2014*, 1298–1301. https://doi.org/10.1109/EMBC.2014.6943836

Sanes, J. N., & Donoghue, J. P. (1993). Oscillations in local field potentials of the primate motor cortex during voluntary movement. *Proceedings of the National Academy of Sciences of the United States of America*, *90*(10), 4470–4474. https://doi.org/10.1073/pnas.90.10.4470

Sanes, Jerome N, Donoghue, J. P., Thangaraj, V., Edelman, R. R., & Warach, S. (1995). Shared Neural Substrates Controlling Hand Movements in Human Motor Cortex Author (s): Jerome N . Sanes , John P . Donoghue , Venkatesan Thangaraj , Robert R . Edelman and Steven Warach Published by : American Association for the Advancement of Science S. *Science*, *268*(5218), 1775–1777.

Schieber, M. H. (2001). Constraints on somatotopic organization in the primary motor cortex. *Journal of Neurophysiology*, *86*(5), 2125–2143. https://doi.org/10.1152/jn.2001.86.5.2125

Schieber, M. H., & Hibbard, L. S. (1993). How Somatotopic is the Motor Cortex Hand Area ? Author (s): Marc H . Schieber and Lyndon S . Hibbard Published by : American Association for the Advancement of Science Stable URL : http://www.jstor.org/stable/2881942 Accessed : 01-04-2016 14 : 02 UTC Yo. *Science*, *261*(5120), 489–492.

Singleton, A. C., Brown, A. R., & Teskey, G. C. (2021). Development and plasticity of complex movement representations. *Journal of Neurophysiology*, *125*(2), 628–637. https://doi.org/10.1152/jn.00531.2020

Song, W. J., Kawaguchi, H., Totoki, S., Inoue, Y., Katura, T., Maeda, S., Inagaki, S., Shirasawa,

H., & Nishimura, M. (2006). Cortical intrinsic circuits can support activity propagation through an isofrequency strip of the guinea pig primary auditory cortex. *Cerebral Cortex*, *16*(5), 718–729. https://doi.org/10.1093/cercor/bhj018

Stark, E., Drori, R., & Abeles, M. (2009). Motor cortical activity related to movement kinematics exhibits local spatial organization. *Cortex*, *45*(3), 418–431. https://doi.org/10.1016/j.cortex.2008.03.011

Stepniewska, I., Fang, P. C. Y., & Kaas, J. H. (2009). Organization of the posterior parietal cortex in galagos: I. Functional zones identified by microstimulation. *Journal of Comparative Neurology*, *517*(6), 765–782. https://doi.org/10.1002/cne.22181

Stepniewska, I., Gharbawie, O. A., Burish, M. J., & Kaas, J. H. (2014). Effects of muscimol inactivations of functional domains in motor, premotor, and posterior parietal cortex on complex movements evoked by electrical stimulation. *Journal of Neurophysiology*, *111*(5), 1100–1119. https://doi.org/10.1152/jn.00491.2013

Takahashi, K., Kim, S., Coleman, T. P., Brown, K. A., Suminski, A. J., Best, M. D., & Hatsopoulos, N. G. (2015). Large-scale spatiotemporal spike patterning consistent with wave propagation in motor cortex. *Nature Communications*, *6*(May), 1–11. https://doi.org/10.1038/ncomms8169

Takahashi, K., Saleh, M., Penn, R. D., & Hatsopoulos, N. G. (2011). Propagating waves in human motor cortex. *Frontiers in Human Neuroscience*, *5*(APRIL), 1–8. https://doi.org/10.3389/fnhum.2011.00040

Woolsey, C. N. (1952). Patterns of localization in precentral and" supplementary motor areas and their relation to the concept of a motor area. *Publ. Assoc. Res. Nerv. Ment. Dis.*, *30*, 238–264.

Wu, J. Y., Huang, X., & Zhang, C. (2008). Propagating waves of activity in the neocortex: What they are, what they do. *Neuroscientist*, *14*(5), 487–502. https://doi.org/10.1177/1073858408317066

Xu, W., Huang, X., Takagaki, K., & Wu, J. young. (2007). Compression and Reflection of Visually Evoked Cortical Waves. *Neuron*, *55*(1), 119–129. https://doi.org/10.1016/j.neuron.2007.06.016

Ylinen, A., Bragin, A., Nádasdy, Z., Jandó, G., Szabó, I., Sik, A., & Buzsáki, G. (1995). Sharp wave-associated high-frequency oscillation (200 hz) in the intact hippocampus: Network and intracellular mechanisms. *Journal of Neuroscience*, *15*(1 I), 30–46. https://doi.org/10.1523/jneurosci.15-01-00030.1995

Young, N. A., Vuong, J., & Campbell Teskey, G. (2012). Development of motor maps in rats and their modulation by experience. *Journal of Neurophysiology*, *108*(5), 1309–1317. https://doi.org/10.1152/jn.01045.2011

Zhuang, J., Truccolo, W., Vargas-Irwin, C., & Donoghue, J. P. (2010). Decoding 3-D reach and grasp kinematics from high-frequency local field potentials in primate primary motor cortex. *IEEE Transactions on Biomedical Engineering*, *57*(7), 1774–1784. https://doi.org/10.1109/TBME.2010.2047015

II. SPATIAL EVOLUTION OF INFORMATION DYNAMICS IN THE PRIMARY MOTOR CORTEX

Abstract

The primary motor cortex (M1) is known to be spatially organized in terms of muscles and body parts, notwithstanding some overlap. However, the classical view is largely static, neglecting potential representational changes on a fast time scale. To address potential representational dynamics, we probed the mutual information between M1 signals recorded across the cortical sheet and electromyography (EMG) activity from a set of muscles while a macaque monkey performed planar reaches. Here, we demonstrated that the spatial organization of the M1 encoding was in fact quite dynamic throughout the course of a reaching movement such that a given cortical site maximally encoded different muscles at different times. Despite these rapid representational changes, a proximal-to-distal gradient of the upper limb representation was preserved particularly close to movement onset. Representation was most stable close to movement onset, with characteristic topographic maps, possibly serving functional needs. This study bridges the important gap between flexible motor encoding and static motor maps, emphasizing the importance of considering space and time together in motor representation studies.

Introduction

For over a hundred years, people have examined whether and how movement representations in the primary motor cortex are spatially organized (Jackson, 1867; Fritsch & Hitzig, 1870; Ferrier, 1886). Various movement relevancies have been investigated, largely assuming a largely static nature of representation over short period of time.

Early maps were generated with surface electrical stimulations, including the simiusculus plotted by Woolsey and colleagues in monkeys (Woolsey, 1952), as well as the homunculus plotted by Penfiled and colleagues in humans (Penfield & Boldrey, 1937; Penfield & Rasmussen, 1950). In those maps, an ordered sequence of body parts (foot, legs, trunk, shoulder, upper limb, hands, face and mouth) was illustrated from medial to lateral cortical sheet, giving an oversimplified impression that the mapping from sites on the primary motor cortex to body parts were clear-cut. Even though the authors did note a certain degree of overlap among body part representations, this fact has not been fully appreciated even today.

With the development of intracortical microstimulation (ICMS) (Asanuma & Sakata, 1967), researchers were able to perform more focal stimulation using penetrating microelectrodes. Park and colleagues (2001, 2004) stimulated layer 5 of primary motor cortex with short-duration low-frequency ICMS, while macaques performed reach-to-grasp tasks. They confirmed the overlapping nature of representation at single sites for the upper limb area, where proximal and distal muscles were co-represented synergistically. They also found a fine horseshoe-shaped spatial map within the forelimb representation, where shoulder and elbow areas surrounded a transitory coactivation zone, which in turn surrounded hand areas.

As people began to explore additional spatial organization, Graziano and colleagues (2002, 2005) found a systematic spatial organization of ethological actions using longer ICMS trains

(500ms) where actions such as the hand moving to lower peripersonal space, hand manipulation in central peripersonal space, chewing/licking were encoded sequentially from medial to lateral portions of M1. They also found that the final arm and hand postures (mainly in the vertical and horizonal axes) were represented at distinct cortical regions. Apart from the above, no global cortical spatial organization has been found with other functional properties of movement, such as velocity, acceleration, force, or change of force (Georgopoulos et al., 2007; Stark et al., 2009; Evarts, 1968; Humphrey et al., 1970).

Even though we know that cortical representation maps are malleable in the long term due to development, learning or injury (Chakrabarty & Martin, 2000; Glees & Cole, 1950; Nudo et al., 1996), the spatial structure of movement representations during a given behavior is largely assumed to be invariant in the examples above, perhaps due to limitations of the ICMS paradigm. This static assumption seems unwarranted, especially considering that movement encoding itself is flexible and dynamic within very short time (Ben-Shaul et al., 2003, 2004; Churchland & Shenoy, 2007; Hatsopoulos et al., 2007; Rokni et al., 2007). Moreover, in the few studies that looked at space and time simultaneously in the representation, no global spatial structure on the cortical sheet has been discovered accompanying representational changes (Ben-Shaul et al., 2003; Hatsopoulos et al., 2007).

Here for the first time, we tracked the dynamics of cortical representational maps of forelimb muscles during single reaches, using mutual information to quantify the relationship between neural activity and electromyography (EMG) activity. We chose the high-gamma band signal in the local field potential as our proxy for neural activity, given its rich information and dense spatial coverage (Rickert et al., 2005). We found that cortical representation across space evolved throughout movement, but certain spatial organization principles such as proximal to

distal gradient were still maintained. Those spatio-temporal representation changes were different for different movement directions, with interesting stability points, likely serving functional needs.

Methods

Surgery procedures

A male rhesus macaque (*Macaca Mulatta*) Bx was the subject for this study. He was implanted with bipolar electromyography (EMG) electrodes in 13 muscles from shoulder to hand (Anterior Deltoid, Posterior Deltoid, Pectoralis Major, Biceps Lateral, Biceps Medial, Triceps Long head, Triceps Lateral, Brachioradialis, Flexor Carpi Ulnaris, Extensor Carpi Ulnaris, Extensor Carpi Radialis, Extensor Digitorum Communis, Flexor Digitorum Superficialis). He was also implanted with a set of dual Utah multi-electrode arrays (Blackrock Microsystems, Salt Lake City, UT) in the left primary motor cortex, each containing 64 electrodes. Electrode length was 1.5mm, with a uniform inter-electrode distance of 4μm in the 8-by-8 grid. The arrays corresponded to the arm/hand areas of the right limb, as confirmed by electrically stimulating the cortex during surgery with surface electrodes and observing corresponding twitches prior to array implantation. All procedures regarding surgery, animal training and data collection were approved by the University of Chicago Institutional Animal Care and Use Committee (IACUC) and obey the Guide for the Care and Use of Laboratory Animals.

Behavioral task

The animal was trained to perform a reach task in different directions, with his right upper limb constrained by a 2D exoskeletal robot (BKIN Technologies). All the reach directions were on a horizontal plane roughly at the height of his elbow when his (right) upper limb was naturally hanging. To perform the task, he moved the joystick at the tip of the robot, while receiving simultaneous visual feedback of the cursor position on the screen in front of him. The task involved a hold period for 1000ms, during which the animal held the joystick steadily, keeping the cursor within a central target. The peripheral target then appeared indicating the desired reach location. He then moved the joystick to direct the cursor to the peripheral target. Each target had a radius of 0.75cm; the distance from the central target to the peripheral target was 5.5cm. The peripheral target could appear in one of 8 possible locations on a circle (in 45° intervals clockwise from 0° to 315°, where forward movement was 0° and rightward movement was 90°). A trial was considered successful once the cursor reached the peripheral target and remained in the target for a variable period of time (400 - 600ms), upon which the animal received juice reward. Movement durations vary across reach directions, but generally ranged between 300 to 1200ms. We also had the monkey perform 2-target center-out task (where target appears in one of two directions: 45° and 225°), to get more trials out of each reach direction. This 2-direction reach task had variable hold time from 800-1200ms, but otherwise identical to the 8-direction task. There was one session for each variant of the task.

Collection and preprocessing of neural and muscle data

EMG signals from 13 muscles were individually amplified, band-pass filtered between 0.3 Hz to 1kHz, digitalized and sampled at 2k Hz. Then for preprocessing, EMG activities were further band-pass filtered between 20 Hz to 1kHz, followed by rectification and smoothing by low-pass filtering below 10Hz. Then, envelopes were down-sampled to 200Hz. Individual trials of muscle activities were aligned on movement onset (defined as the time point where 15% of the peak speed was reached for that trial).

Neural signals were collected with Blackrock Microsystems (Salt Lake City, UT). To obtain local field potentials, neural signals from 128 channels were low-pass filtered below 500Hz with a Butterworth filter and then digitized at 2kHz. From there, high-gamma band signals were extracted by band-pass filtering within 200Hz - 400Hz with a Butterworth filter. We then computed the Hilbert transformation to obtain the amplitude envelopes. Finally the envelopes was low-pass filtered below 10Hz to match the smoothness of muscle signal, and then down-sampled to 200Hz.

Intracortical microstimulation

Short-duration intracortical microstimulation (ICMS) was performed to map the classical somatotopic map. For each stimulation event, we stimulated an electrode for 25 biphasic pulses (cathodic first) at 333Hz. The duration of positive and negative phases were 200µs, with an interval duration of 55 µs. We started at 20µA for each electrode. If any muscle twitch was observed, we lowered the current to determine the threshold and isolate the effect; if no muscle twitch was observed, we increased the current level. If no muscle twitch was elicited at 40µA, the effect of stimulating this electrode would be considered as 'not observed'.

Estimation of mutual information

To comprehensively quantify the dependent relationship between two variables, we used mutual information (MutInfo). The mutual information between two continuous variables *x* and *y* is a function of the joint probability distribution and marginal distributions:

$$MutInfo(X,Y) = \int dx\, dy\ P(x,y) \log_2 \frac{P(x,y)}{P(x)P(y)}$$

Equation 2.1

Traditional estimations used fixed or adaptive binning to extract the probabilities above (eg. Darbellay & Vajda, 1999), which are subject to non-negligible systematic errors (Kraskov et al., 2004). Instead, we used Kraskov-Stögbauer-Grassberger estimator, a binless mutual information estimator (Kraskov et al., 2004). It utilizes another formulation of mutual information, expressed by the difference between marginal and joint entropies:

$$MutInfo\ (X,Y) = H(X) + H(Y) - H(X,Y)$$

$$\text{Where } H(X) = -\int dx\ P(x) \log_2 P(x)$$

Equation 2.2

The probability distributions above were estimated based on the *k*-th nearest neighbor distances, where multivariate neighbors were defined based on the maximum norm. By varying *k*, one can adjust the spatial scales on which relationships are being probed. Important expansions of this method were made by Holmes and Nemenman (2019)which enables estimation of error bars and detection of sample-size dependent bias, facilitating the selection of *k*. Sample-size dependent

bias is present when MutInfo estimations made with non-overlapping subsamples of the full data (e.g. until 10 divisions) result in much lower estimates than using the full dataset (e.g. beyond one standard error). A small k generally (1) enables the detection of features at a finer scale, (2) utilizes data points better and possesses less sample-size dependent bias, but (3) is also more susceptible to fluctuations in the distribution thus having a larger error bar (sometimes estimates could reach impossible negative MutInfo values within one standard error). In our case, k was selected to strike a balance among those considerations: we chose k values that resulted in acceptable standard deviations and minimal sample-size dependent bias. For all-directions pooled MutInfo computations, we used k=4; for direction-separated MutInfo computations, we used k=9. This was to deal with the increasing fluctuations in the distributions when less data points were available. Our results were qualitatively stable across a range of k values.

In order to track the changes of mutual information along movement execution, we divided the EMG activities into 29 sliding time windows, with 200ms window size and 50ms step size (i.e. -400ms ~ -200ms, -350ms ~ -150ms, …, 1000ms ~ 1200ms). Within each window, we consider different leads/lags of muscle and neural activity, from 600ms neural-led to 400ms muscle-led in steps of 5ms. In the direction-pooled version, mutual information was computed between neural signal and EMG for each electrode-muscle pair at each lead/lag, with all sample points of each time window from all trials; in the direction-separate version, mutual information was computed between neural signal and EMG for each electrode-muscle pair at each lead/lag, with sample points of each time window further down-sampled by 4 times (i.e. 50Hz), for trials with the same target direction. Subsampling was done to address the problem of autocorrelation in the continuous signals, especially given less diversity in trials in the case of direction-specific data. As our interests are mainly focused on relative strengths, (remaining) autocorrelation should not

be a severe problem regarding mean estimates to either pooled or direction-specific variants. As for its effect on error bar estimation, we carefully mitigated it by choosing *k*s that are not too small so that our comparisons would still be meaningful even when error bars were slightly underestimated.

Key implementation code was based on Holmes and Nemenman (2019), which could be accessed at https://github.com/EmoryUniversityTheoreticalBiophysics/ContinuousMIEstimation.

Computation of MutInfo-based somatotopic map

At each particular *k* and subsampling ratio (and for each reach direction, in the case of direction-specific mutual information), we arrived at a 4-dimensional tensor of mutual information of shape 29 (# of absolute time windows) × 13 (# of muscles) × 201 (# of relative times) × 128 (# of electrodes).We selected the range of relative time from -300ms to 300ms and then computed the maximal MutInfo over the axis of relative times, arriving at a 3-dimensional tensor of 29 (# of absolute time windows) × 13 (# of muscles) × 128 (# of electrodes).

To arrive at the full map, for each absolute time window and for each electrode, we picked the muscle that had the maximal mutual information out of the 13 muscles, and used the color corresponding to that muscle to represent that electrode on the cortical map. To arrive at the 'motor' map from the full map, we only kept electrodes where maximal mutual information values were obtained at negative relative times (i.e. neural activity preceding EMG). To arrive at the 'sensory' map from the full map, we only kept electrodes where maximal mutual information values were obtained at positive relative times (i.e. EMG preceding neural activity).

Computation of representation evolution (non-spatial view)

Like above, at each particular *k* and subsampling ratio (and for each reach direction, in the case of direction-specific mutual information), we arrived at a 4-dimensional tensor of mutual information of shape 29 (# of absolute time windows) × 13 (# of muscles) × 201 (# of relative times) × 128 (# of electrodes).We selected relative time range from -300ms to 300ms and then computed the maximal MutInfo over the axis of relative times, arriving at a 3-dimensional tensor of 29 (# of absolute time windows) × 13 (# of muscles) × 128 (# of electrodes). We then computed the space-independent representation using two methods: summing-up or winner-take-all.

With the summing-up method, for each absolute time window and for each muscle, we summed up all the mutual information values for all electrodes, arriving at a matrix of mutual information, of shape 29 (# of absolute time windows) × 13 (# of muscles). Next, muscles were grouped according to the representation classification of interest (i.e. body parts — shoulder/elbow/wrist/hand, FE — flexion/extension, or both body part and FE — eight combos). Finally, for each absolute time window, mutual information values for muscles of the same group were added up, then divided by the number of muscles in that group. This last step of division was to ensure that representation intensity was not affected by the different number of muscles we had sampled in each group. We ended up with a representation matrix of shape 29 (# of absolute time windows) × 2/4/8 (# of groups).

With the winner-take-all method, for each absolute time window and for each muscle, we counted the number of electrodes that had this muscle as the top-represented muscle, arriving at a matrix of electrode counts, of shape 29 (# of absolute time windows) × 13 (# of muscles). Next, muscles were grouped according to the representation classification of interest like above.

Finally, we adjusted the electrode count by dividing by the number of muscles in that group, arriving at representation matrices as explained above.

Tensor decomposition

For mutual information computed separately for eight directions, we reorganized tensor into a 3-dimensional tensor of shape [# of directions × (# of muscles × # of electrodes) × (# of absolute time windows × # of relative times)]. To understand potential low-dimensional structures of the mutual information tensor, we performed a form of non-negative tensor factorization, namely CANDECOMP/PARAFAC (canonical decomposition/ parallel factors, CP) decomposition (Kim & Park, 2012; Kola et al., 2017), which approximates the tensor as a sum of outer products (i.e. factors) of 3 non-negative vectors (one for each dimension). Code is available at https://github.com/kimjingu/nonnegfac-matlab/blob/master/ncp.m and https://www.tensortoolbox.org. The performance of reconstruction is measured by the relative error, which is the ratio between the Frobenius norm of the error tensor and the Frobenius norm of the original tensor, with the error tensor being the difference of the original tensor and the reconstructed tensor. Number of factors were selected based on a balance of low relative error and interpretability.

Results

Somatotopic representation is dynamic during reach

During the center-out task, our monkey subject performed constrained reaches towards one of eight directions on the horizontal plane (Fig. 2.1a), while his EMG activity and high-gamma LFP activity were extracted. To start with, we wanted to obtain a general understanding of the evolution of representation around movement onset. For that, we computed the mutual information between each muscle and electrode pair, using data from all reach directions. For example, for the pair of Anterior Deltoid (Fig. 2.1b) and electrode 101 (Fig. 2.1c) using a -80ms lag (neural activity preceding muscle activity), mutual information changed throughout the reach course, reaching the peak at around -50ms relative to movement onset. For the same muscle with another electrode (electrode 9, Fig. 2.1e) also using -80ms lag, the temporal evolution of mutual evolution followed a slightly different time course, reaching peak at movement onset (Fig. 2.1f). Nevertheless, there was a general trend for information to be initially low, then increase transiently before returning to baseline levels. For most of them, there was a sharp increase in mutual information around movement onset.

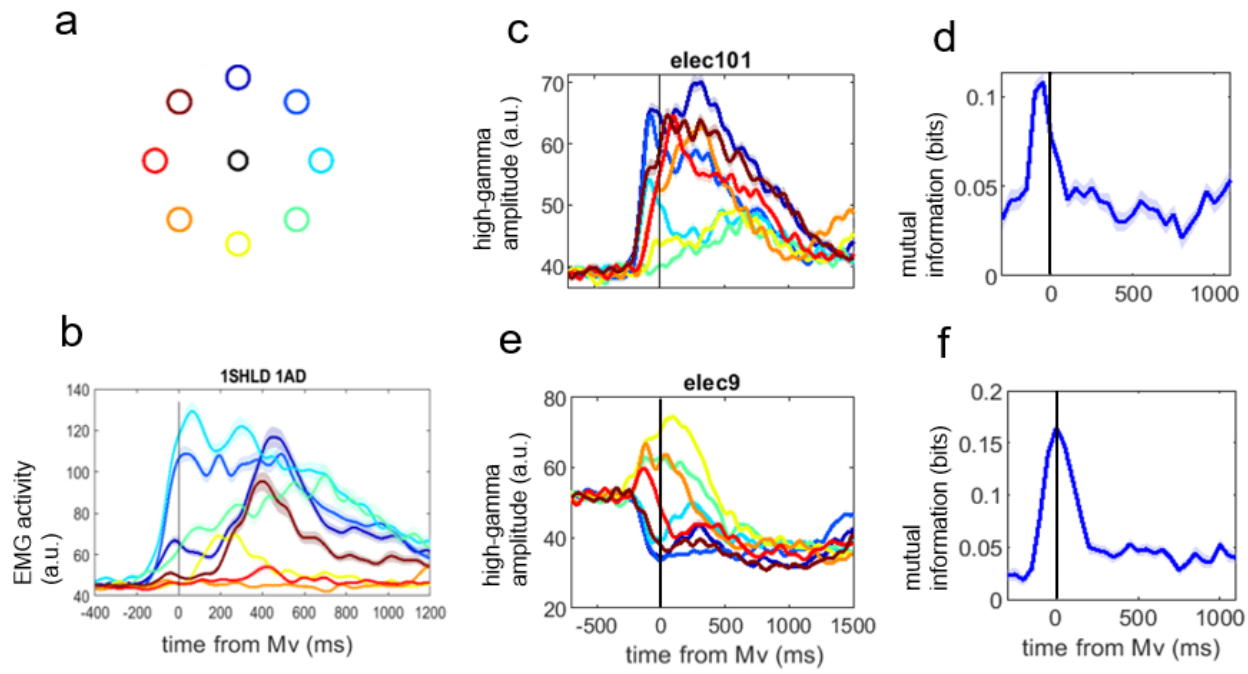

Figure 2.1 Different mutual information evolutions for different muscle-electrode pairs. **a**. movement task was a constrained reach task from the central black target to one of eight colored targets on the periphery. **b**. EMG activity of a shoulder muscle Anterior Deltoid, averaged for each reach direction separately. Color of traces were the same as target illustration in **a**. Shaded area represented standard error of mean (SEM). **c**. amplitude of high-gamma envelope at electrode 101, averaged for each reach direction separately. Color of traces were the same as target illustration in **a.** Shaded area represented SEM. **d**. mutual information computed for muscle in **b** and electrode in **c** at -80ms relative timing (neural activity preceding muscle activity by 80ms), separately for each 200ms-long time window along movement course. Trials from all directions were considered for this figure. Shaded area represented SEM. **e**. same as **c** but for another electrode (electrode 9). **f**. same as **d** but for another pair: muscle in **b** and electrode in **e.** Similar rise of mutual information was present upon movement onset but at a slightly later time than in **d**.

Next, we aimed to visualize the representation change on the cortical sheet. For each electrode, we considered the muscle that was represented most (i.e. the muscle with which this electrode had the most MutInfo) in a certain time window. There are three versions of somatotopic maps: full map (Fig. 2.2a), 'motor' map (Fig. 2.2b) and 'sensory' map (Fig. 2.2c). The 'motor' map only displayed electrodes whose maximal MutInfo were obtained when neural activity preceded

muscle activity; while the ‘sensory’ map only displayed electrodes whose maximal MutInfo were obtained when neural activity lagged muscle activity. The full map combined both maps and further included a few electrodes where the maximal MutInfo were obtained with simultaneous muscle and neural activity. Note that we are not implying any direct causality here, as that is beyond the connotation of mutual information.

In all those maps, representations of the same muscle were distributed across a relatively large area of the cortical sheet, but also possessing preferred congregation area. Looking at the full map (Fig. 2.2a), a majority of wrist representation was present during the hold preparation period. Then closer to movement onset, a lot of those wrist representation was replaced by a separation of shoulder and hand representation, roughly following the proximal-distal gradient in the ICMS-based somatotopic map. As the movement unfolded, more wrist and elbow representation started to come in. As for the ‘motor’ and ‘sensory’ maps, during hold we observed slightly more ‘motor’ sites than ‘sensory’ sites, then closer to movement onset, there was a sharp increase of ‘motor’ sites, which gradually receded as movement unfolded, giving place to ‘sensory’ sites. Interestingly, the representation in the corresponding ‘motor’ and ‘sensory’ maps were quite representative of the full map, with similar ratios of muscle preferences and locations. This implied the integrative nature of the ‘motor’ and ‘sensory’ sites in the primary motor cortex, mostly likely from one continuity.

Note that despite the constant evolution, the MutInfo-based somatotopic maps never resembled the ICMS-based somatotopic map. In general, MutInfo-based maps had less distinct boundaries between body parts and were more distributed; the ratio of body part representation constantly changed, and a certain electrode could represent different muscles at different times.

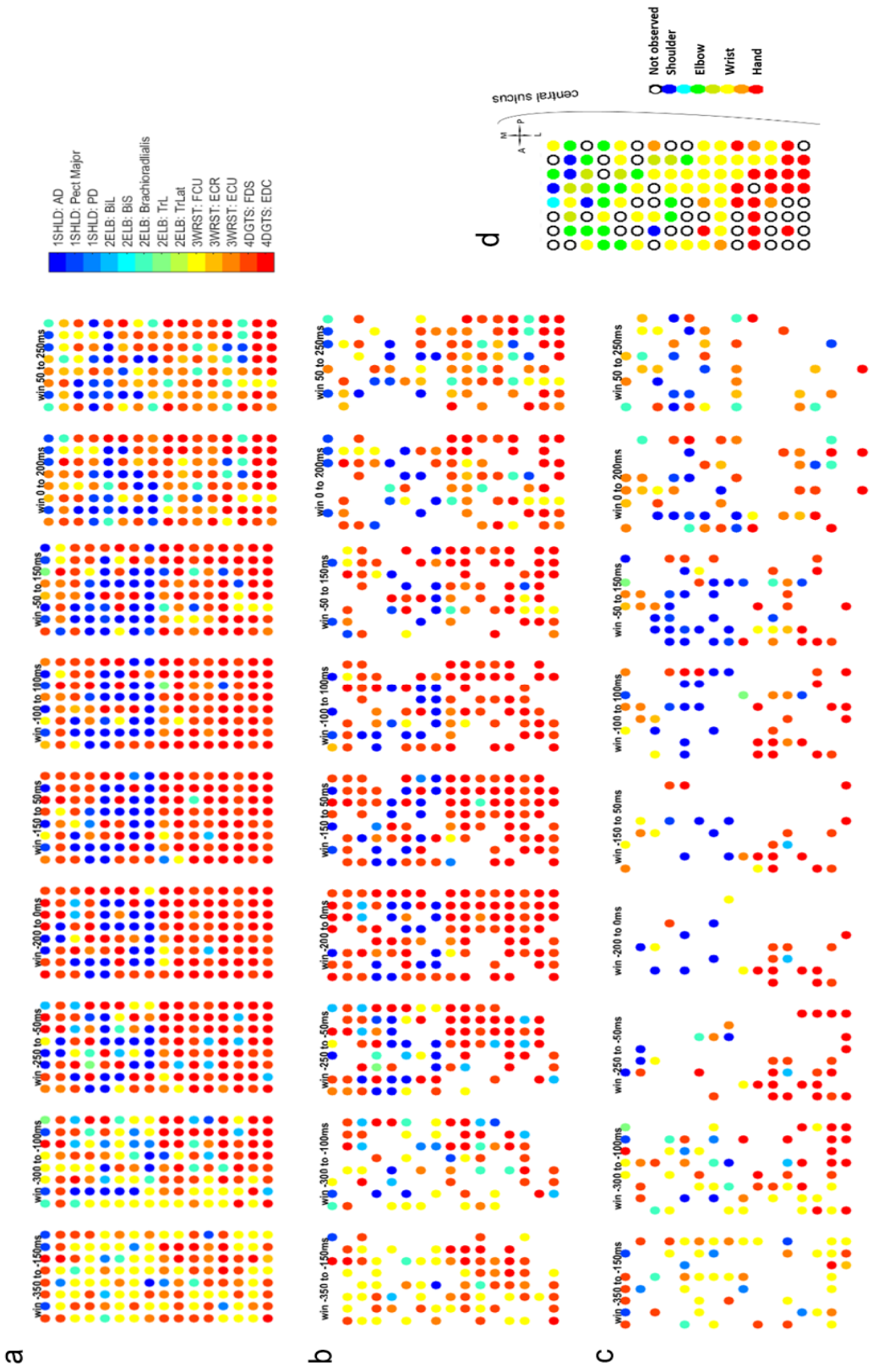

Figure 2.2 Mutual information based somatotopic maps were dynamic and different from ICMS-based map. **a.** mutual information based somatotopic map - full map. Each circle was

(**Figure 2.2** continued) color-coded by the muscle that was most represented at this site at this time window in the movement course. **b**. mutual information based somatotopic map – 'motor' map. Same as **a** but only showing electrodes that obtained the maximal mutual information at relative times where neural activity preceded muscle activity. **c**. mutual information based somatotopic map – 'sensory' map. Same as **a** but only showing electrodes that obtained the maximal mutual information at relative times where neural activity lagged muscle activity. **d**. ICMS-based somatotopic map, color-coded by the body part that twitched during electrical stimulation.

Representation evolution is movement-specific and widely distributed

Beyond general representation change throughout movement obtained using a pool of heterogenous reaches, we wanted to know whether different movement directions possessed different representational dynamics. For that, we computed mutual information for each muscle-electrode pair at each relative times at each absolute time windows, separately for each reach direction.

Before diving into the many new sets of somatotopic maps, for simplicity we first illustrated the changes of representation strength in a space-independent way. Here, we added up mutual information obtained from different electrodes for the same muscle, then further grouped the muscles by their body locations and flexion/extension (i.e. polarity) function. (Note that this summation operation on mutual information is not perfect — see Discussion for further considerations and justifications). The summed mutual information was then adjusted according to the number of muscles in that group, to reduce the effect of biased muscle sampling (see Methods for details). Fig. 2.3 shows the resultant dynamic changes of representation strength through reaches of different directions. Adjacent directions tended to have similar dynamical patterns. Most muscle categories obtained peak representation strength around movement onset for most directions, with some exceptions: shoulder flexors and wrist extensors peaked later for forward and leftward directions (Fig. 2.3 a, g, h); a different type of representation strength

evolution was present for inward and inward-rightward directions (Fig. 2.3 d and e), characterized by slow rise and delayed (multiple) peaks. While digit flexors were the most represented group closer to movement onset for most directions, shoulder extensors were most represented for inward and leftward directions (Fig. 2.3 e-g). Notably, there was great consistency between sessions, as results obtained from a 2-direction reach session on another day showed very similar evolution of representation strengths (insets in Fig. 2.3b and f).

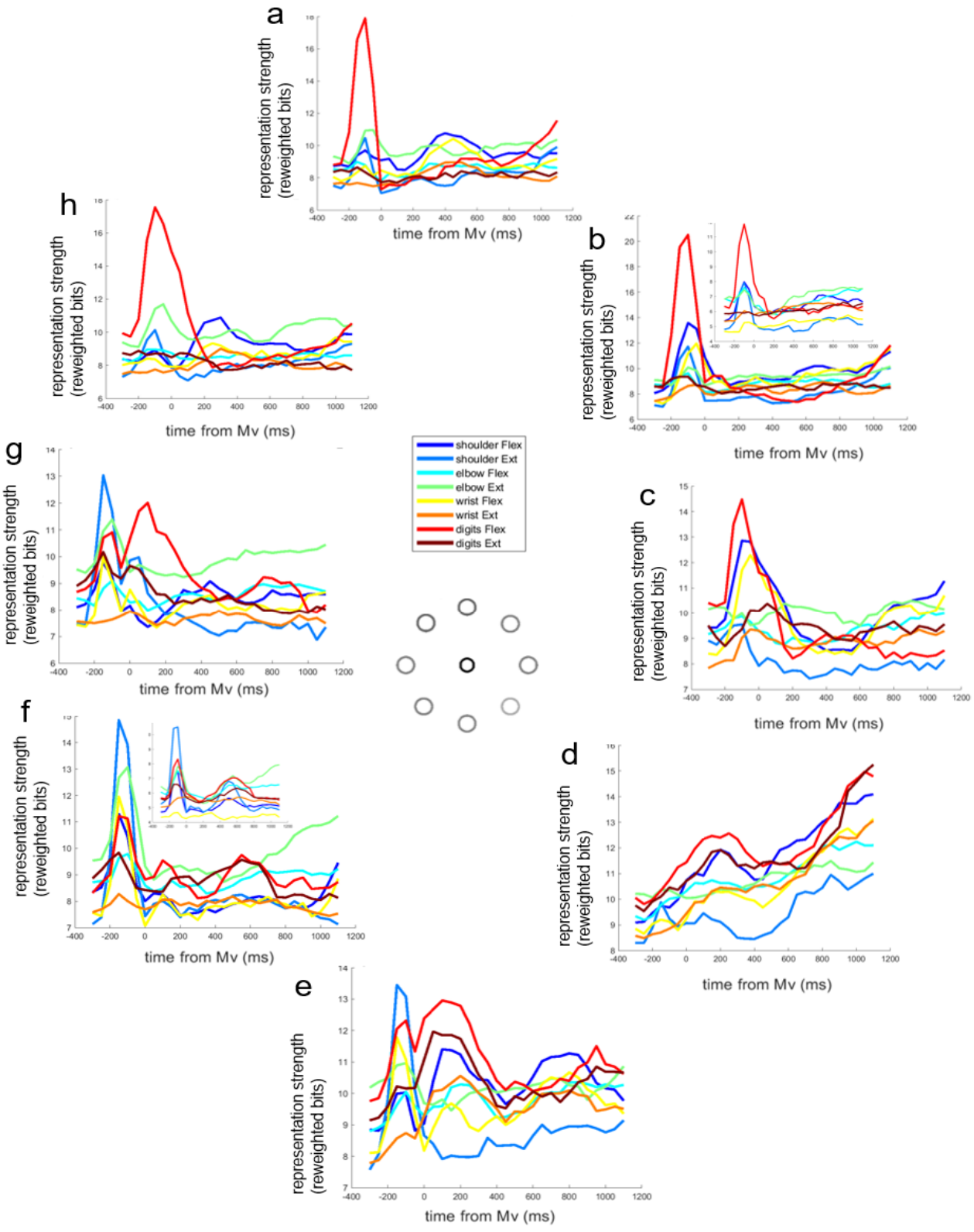

Figure 2.3 Evolution of representation strengths was movement-specific. Mutual information evolution was computed separately for eight reach directions (**a**–**h**), arranged in sequence

(**Figure 2.3** continued) according to actual physical reach directions. In each figure, each line was color-coded by body part and flexion/extension combinations. Insets in **b** and **f** show results from the same direction reaches from a 2-direction reach dataset obtained on a different day.

Next, we explored more thoroughly four representative diagonal directions (45º, 135º, 225º and 315º) from the 8-direction center-out dataset (Fig. 2.4 a-d). Common to all reach directions, more than half of the sites constantly changed their muscle representations through the movement course (blue line in the first row of Fig. 2.4). Only a tiny fraction of sites preserved both body part and polarity categories despite muscle change (difference between blue and purple lines in the first row of Fig. 2.4), while a little less than a quarter of sites preserved body part (difference between blue and red lines in the first row of Fig. 2.4), and roughly half of sites preserved polarity (difference between blue and yellow lines in the first row of Fig. 2.4). Those ratios roughly matched chance levels, indicating that the representational shifts were quite random and not particularly 'compensatory'. For each reach direction, there was a timepoint with most representational stability, where usually 50~60% of sites preserved the body part and flexion/extension represented (green line in the first row of Fig. 2.4). For most directions, this timepoint was immediately prior to movement onset, except for the 135º reach direction considered here which had a slower ramp-up. Those stability timepoints corresponded to particular layouts of the somatotopic maps (including the full map, 'motor' map and 'sensory' map, here showing only the former two in the second row of Fig. 2.4), which were usually vastly different for different reach directions. Maps and most represented muscle could be quite similar for similar reach directions (Fig. 2.4 a and d). Those most represented muscles were largely activated for those particular directions at those stability timepoints (third row in Fig. 2.4), though not necessarily reaching the overall EMG peak in the whole time course just yet.

Looking at the change in body part represented (last two rows of Fig. 2.4), again reach direction made a difference. The change of representation strength was analyzed in two ways here: in addition to the MutInfo-summation view explained above, we also counted the number of electrodes favoring each muscle (winner-take-all view). The winner-take-all (electrode count) view was in general more fluctuating than the MutInfo-summation view as expected. Interestingly, the MutInfo-summation view many times showed different trends, timing and relative ranking of body parts, compared to the winner-take-all view. For example, shoulder representation had different peaking time for 45º reach direction (Fig. 2.4 a, last two rows). As another example, shoulder and elbow representation was quite heavy in the MutInfo-summation view but not in the winner-take-all view, with the latter heavily dominated by digits (Fig. 2.4 c, last two rows). This implied that the cortical representation for shoulder and elbow were more distributed than that for digits at least during certain movements.

We also looked at data collected from another dataset of 2 reach directions (45º and 225º) on a different day, respectively in Fig. 2.5 a and b. The instability trends (first row in Fig. 2.5) and representation strength trends (last two rows in Fig. 2.5, especially the more stable last row) were qualitatively similar to those in Fig. 2.4. Somatotopic maps had varied layout, but the most represented muscle in each reach direction (in the winner-take-out sense) was the same as in Fig. 2.4. The consistency of results among different sessions of similar tasks indicated that the representation scheme of the same movement was relatively fixed across days.

Figure 2.4 Evolution of representation (in)stability, topography and strength. Results were obtained from 8-direction center-out reaches, but only showing four diagonal directions (45º, 135º, 225º and 315º, from **a** to **d**) for clarity. Those reach directions were noted in the insets of the figures in the first row. The first row shows the instability and stability of representation from adjacent time windows. Blue lines show the number of electrodes whose most represented

(**Figure 2.4** continued) muscle changed in adjacent time windows; red lines show the number of electrodes whose most represented muscles in adjacent time windows were from different body parts; yellow lines show the number of electrodes whose most represented muscles in adjacent time windows were from different flexion/extension function group; purple lines show the number of electrodes whose most represented muscles changed either body part or flexion/extension; green lines show the number of electrodes whose most represented muscles kept the same body part and flexion/extension. Green arrows point to the peak of the green lines (i.e. most stability observed during the movement course). The second row shows the corresponding full somatotopic map (left) and 'motor' map (right) at the time point of most representational stability, color-coded using muscle colors as in the legend of Fig. 2a. The third row shows the average EMG activity for the muscle that was most represented in the full map. Each trace represented a different reach direction just as in Fig. 1, with the colored arrow pointing to the trace for the specific direction considered here. The last two rows show changes of representation strength of different body parts, computed using two different methods: the fourth row was computed in a winner-take-all sense, using adjusted electrode count as the measurement; the fifth row was computed using a MutInfo-summation method, using adjusted bits as the measurement. See Methods section for details.

Figure 2.5 Evolution of representation (in)stability, topography and strength for another dataset. Same as Fig. 2.4 but obtained from another dataset of 2-direction center-out reaches (**a** for 45º, **b** for 225 º). See descriptions for Fig. 2.4.

Representation for different movements could be explained by common factors

Finally, we aimed to simplify the understanding of dynamic representation for different reach directions, muscles and sites. For this purpose, we performed non-negative matrix decomposition on the tensor of mutual information (Fig. 2.6 a, see also methods for details), and showed that the representation for different movements could be understood using a unified set of bases. We performed the decomposition using 2~5 factors, which produced relative errors of 0.6261, 0.6169, 0.6164, 0.6120 respectively. We chose 4 factors, considering both interpretability and faithfulness of reconstruction. Weights of the dimensions of reach direction were quite continuous for adjacent directions (Fig. 2.6 b). Representation for rightward and inward movements had later peaks and was slightly noisier in general (Fig. 2.6 c factor 2 and 1).

Representation for most reach directions (especially outward ones) had sharper early peak which could diffuse into later movement segments (Fig. 2.6 c factor 3 and 4). The sharp early factor (factor 3) had an interesting spatial component as well: the lateral posterior part of the primary motor cortex was most involved in this early sharp rise of mutual information (Fig. 2.7 a), not only for digits muscles but also for many of the shoulder, elbow and wrist muscles. This early informative concentration later diffused to more medial and anterior parts of the cortical sheet for most muscles considered (e.g. Anterior Deltoid, Pectoralis Major, Biceps Lateral, Biceps Medial, Triceps Long head, Flexor Carpi Ulnaris, Extensor Digitorum Communis, Extensor Carpi Ulnaris), though in some cases stayed in the lateral posterior area (e.g. for Brachioradialis, Extensor Carpi Radialis and Flexor Digitorum Superficialis) (see Fig. 2.7 b). For those remaining rightward-inward movements which didn't have a sharp early information rise, the slow rise of information was quite diffuse spatially, with some sparse hotspots on the cortical sheet (factor 2, spatial weights not shown here).

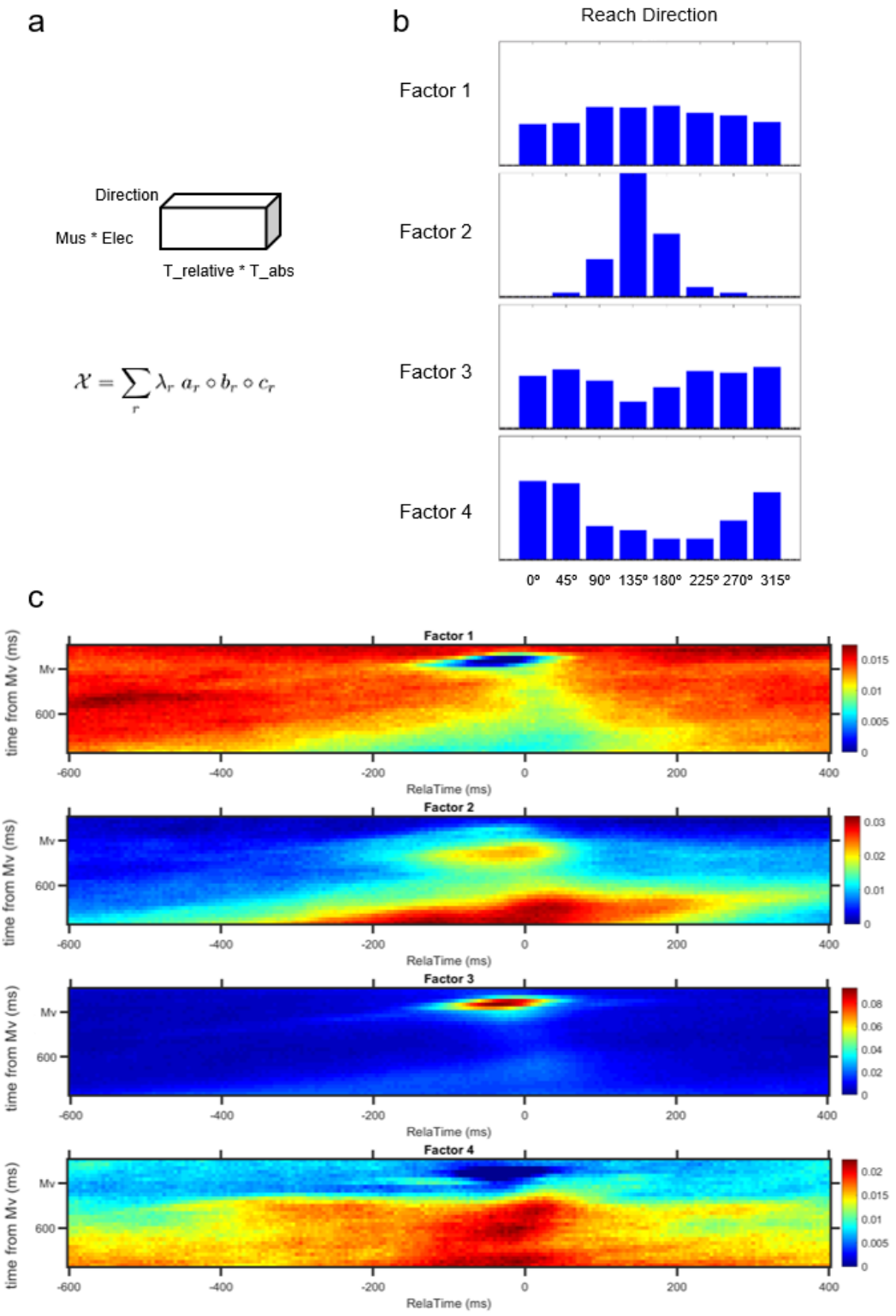

Figure 2.6 Non-negative factorization revealed common factors of representation dynamics among different reach direction. **a**. Tensor arrangement before decomposition. Three dimensions were reach direction, a merged time component, and a merged muscle & electrode component. **b**. Weights of the reach direction dimension, respectively for each of the four factors. **c**. Weights of the time dimension, respectively for each of the four factors.

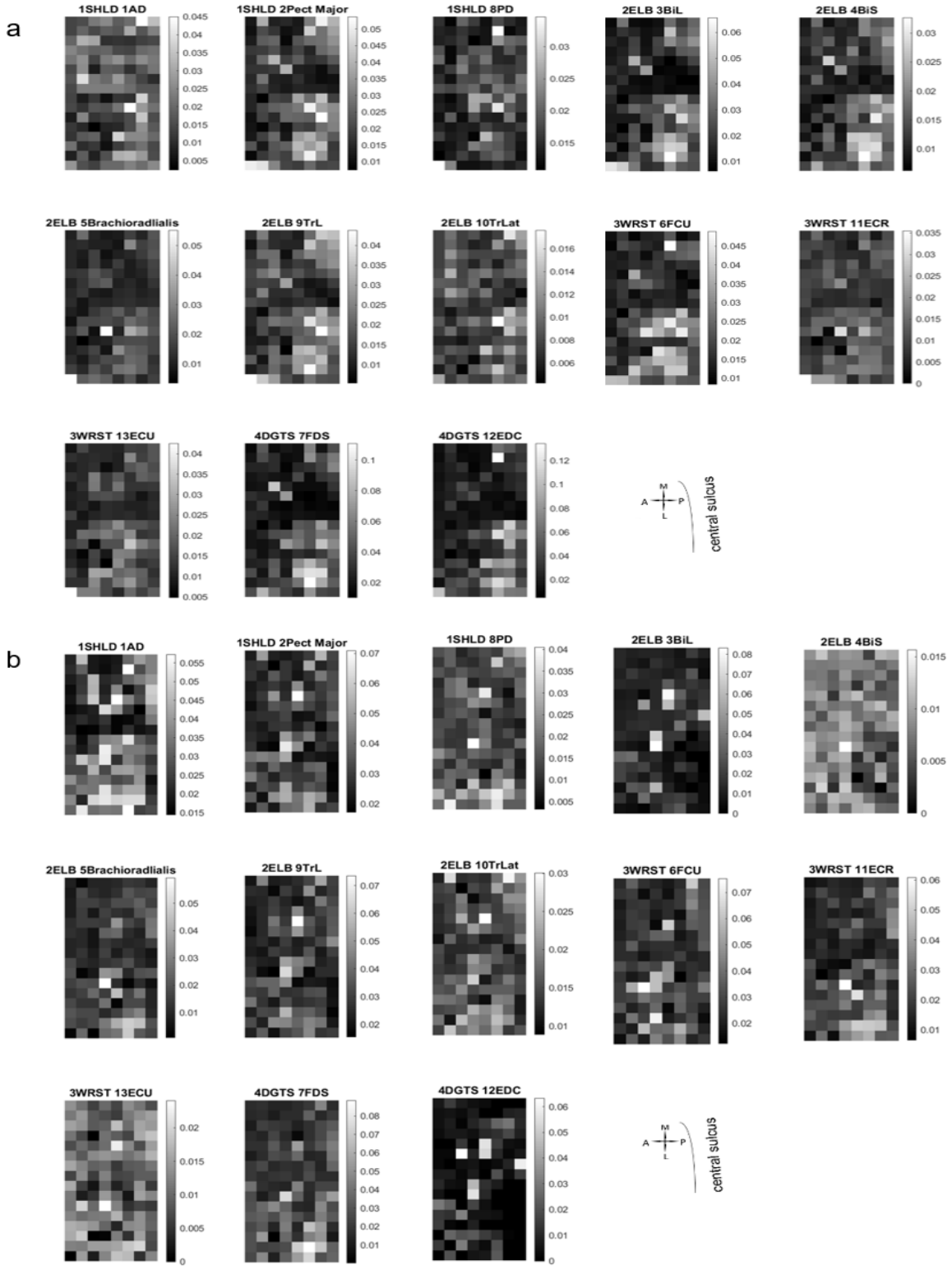

Figure 2.7 Spatial shift of information concentration. For most reach directions (except rightward-inward ones), concentration of information shifted from lateral posterior part of the cortical sheet of primary motor cortex implanted to more anterior and medial directions. **a**. Weights of the electrodes for each muscle for factor 3. **b**. Weights of the electrodes for each muscle for factor 4.

Discussion

Classic ICMS-based studies established crude somatotopic maps on the cortical sheet using short ICMS trains and, more recently, action and postural maps using long ICMS trains (Penfield & Boldrey, 1937; Woolsey, 1952; Park et al., 2001; Graziano et al., 2002), but these studies neglected a crucial temporal aspect. On the other hand, studies establishing the fluidity of movement representation generally did not consider the cortical sheet explicitly (Churchland & Shenoy, 2007; Sergio et al., 2005); in rare cases when the cortical sheet was explored, no spatial structure was found on a mesoscopic scale (Ben-Shaul et al., 2003; Hatsopoulos et al., 2007).

To our knowledge, this study is the first to discover large-scale spatial arrangements of movement representation on the cortical sheet in a time-resolved fashion. Using mutual information as the measurement of representation strength, we confirmed the ever-evolving nature of movement representation (more specifically, muscle representation) and illustrated each representation snapshot on the cortical sheet. Despite the distributed and overlapping nature of muscle encoding on the cortical sheet, a clear distal-proximal gradient was present throughout movement course. Furthermore, these dynamic representations on the cortex were movement-specific, with varying times of stability and topographic maps, possibly serving functional needs.

Temporal representation

Temporally, we characterized a special timepoint in the course of representational evolution — movement onset where the representations for individual muscles were usually strongest and most stable immediately prior to movement onset. This unique timepoint echoes to what others have found. Sergio et al. (2005) discovered that with the center-out movement task, single units

developed directional tuning upon force onset, which then continuously changed directional tuning. Using a similar task, Ben-shaul et al (2003) also discovered changing tunings of single units, which was particularly different between holding and execution. Those affirmative results were encouraging especially considering the complementary nature of their formulation of tuning versus our formation of representation (which will be discussed in more detail in later part of Discussion).

Another prominent feature for the temporal evolution of representation was its movement-specificity. We found that different movement directions had different representational changes; in other words, specific recruitment patterns of muscles strongly covaried with its instantaneous cortical representation. Moreover, the stabilized maps had strong representations for muscles that were heavily recruited at those times for those particular reach directions.

So what could be the underlying reason for representations to be movement-specific? Larger mutual information was not a trivial by-product from simply having larger EMG activity, since (1) in our observation, the largest EMG activity didn't always coincide in time exactly with the largest mutual information; and (2) in theory, mutual information is reparameterization-independent (Kraskov et al., 2004), so simple scaling of the amplitudes of the muscle signals and/or neural signals would not change their mutual information. Instead, this reorganized representation likely reflected actual *functional needs* – the need to represent finely the muscles that were mostly needed at this particular timepoint. This explains why we saw non-canonical time courses for representational stability in direction 135º (Fig. 2.4 b first row), where representation was stabilized as late as 450ms; most likely it was due to the need for later muscle activation (e.g. Extensor Carpi Radialis). There exists additional evidence in support for the argument for functional needs. Sergio et al. (2005) explored another task in the same study

mentioned above, which was isometric (requiring monotonic force ramping thus exhibiting monotonic muscle activity). Curiously, no change in tunings was observed once tunings were established upon force onset. Perhaps these relatively stable tunings in this task of theirs were precisely due to the scarce need of functional change of representation in this scenario. In contrast, the center-out movement task in their and our studies, where muscles tended to exhibit tri-phasic activities (Forget & Lamarre, 1987), required more stages of varying representation in order to fulfill varying recruitment needs. It would be illuminating to conduct our analyses with their isometric task to confirm this hypothesis.

Spatial representation

Regarding space, while Hatsopoulos et al. (2007) and Ben-shaul et al. (2003) discovered that the same site or neighboring sites tended to have relatively similar directional tuning, there was no systematic organization over cortical sheet on the mesoscopic scale. This study, in contrast, discovered that muscle representations were very clustered on a scale of tens of μms, also conforming to the proximal-distal (body part) gradient. This stark disparity was likely mostly due to the different choices of tuning features (preferred direction in the kinematic view versus muscle in the kinetic view). Despite constant fluidity, muscle representation is more spatially-organized on the cortical sheet than preferred directions, possibly because the former was to some extent developmentally hard-wired following gradients due to different timings of circuit development (in spinal cord and brain stem) for proximal versus distal limbs (Martin et al., 2005), while the latter was predominantly secondarily formed based off interactions with the physical surroundings, thus having to evolve under pre-existent representation constraints (Aflalo & Graziano, 2006).

As a side note, in a spatially-continuous manner, we discovered interleaved 'motor', 'sensory' and 'simultaneous' locations for the same muscles (Fig. 2.2). This perhaps seems puzzling at first glance, considering all recorded sites were in primary motor cortex, but is not too surprising in the literature (for a review, see Hatsopoulos & Suminski, 2011). Potentially, those 'simultaneous' and 'sensory' locations could serve in predictive control (Flament & Hore, 1988), feedback control (Pruszynski et al., 2011), kinesthetic perceptions (Naito et al., 2011) and movement observation (Suminski et al., 2009). The spatial continuity in those different lag groups pointed to the integrative and collaborative nature of motor representation.

Interplay between spatial and temporal representation

Not only was muscle representation spatially organized on the cortical sheet throughout movement, there existed interplay between cortical space and time in movement. Firstly, we discovered enlarged proximal-distal gradient encompassing more diverse body parts upon movement onset (Fig. 2.2). Interestingly, Ben-shaul et al. (2003) found that neighboring electrodes exhibited bigger tuning disparity during movement compared to preparation (75° vs. 45° of tuning disparity during movement vs. during preparation), which corresponded to an increase in representation diversity upon movement onset in our study. The preservation of proximal-distal gradient could potentially help to maintain a relatively stable representation on the mesoscopic spatial scale, thus reducing the efforts of having to make drastic movement-dependent changes in various anatomical and functional connections.

Secondly, we found that close to movement onset, the most informative locations on the cortical sheet were at the lateral-posterior part of the primary motor cortical sheet probed, for many

muscles distributed across forelimb; this information concentration later diffused to other locations on the sheet. To probe for those patterns, we intentionally kept muscle and electrode together in one dimension in the non-negative tensor decomposition, which allowed patterns between muscles and electrodes to form naturally. As commonality of spatial component among muscles was not forced in the dimensionality reduction, it is more meaningful that we discovered similar spatial components for different muscles, including distal and proximal muscles alike. This early 'universal' information hotspot in primary motor cortex we discovered here might indicate that at the early stage of movement this area was most direct in dictating muscle activities. For example, we know that there were more cortico-motoneuronal (CM) cells in caudal primary motor cortex, which made monosynaptic connections to motoneurons in the ventral horn; in comparison, the rostral area had fewer CM cells but more corticospinal (CST) neurons, mostly connecting to interneurons in the spinal cord (Rathelot & Strick, 2009). Importantly, the concentration of CM cells in caudal primary motor cortex not only connected to motoneurons controlling distal muscles, but also those controlling proximal muscles (Rathelot & Strick, 2009), which was reminiscent of what we found here. While further studies will be needed to elucidate the origin of this phenomenon, there are definitely advantages to such an arrangement. An early concentrated information hub could facilitate early coordination of muscle synergies, as different combinations of muscle recruitments can be flexibly used to achieve the same limb movement.

Lastly, an interesting observation is that the relative representation strength in the winner-take-all view and summation view did not always agree, especially as time evolved (Fig. 2.4 and 2.5, last two rows). This fact implied that information was distributed to different extents for different body groups, and for different timepoints throughout movement. Representation for digits tended

to be the more concentrated in single electrodes than for elbow or shoulder, perhaps due to less coordinative requirements for distal joints compared to connective joints. This observation is to some extent in line with the classical horseshoe shape of upper limb representation, where larger distal and intermediate representations encircled smaller distal representation (Park et al., 2001).

Measurement of representation

Crucial differences between our study and previous studies lie in our choice of representational measurement. Representation, or mapping, is supposed to be a relationship between (at least) two variables, which should be computed (at least) at 2nd-order. Traditionally, people used (stronger) neural activation to serve as proxy of (stronger) representation, studied at each movement or effector group, which could result in fragmented or biased understanding (e.g. neglecting inhibitory effects when studying tuning). In contrast, we directly measured the inter-dependence between effector of interest and neural activation, which is a 2nd-order measurement that directly speaks to the representation issue at hand. Furthermore, we chose to use mutual information in the continuous formulation as the measurement of inter-dependence (Kraskov et al., 2004; Holmes & Nemenman, 2019), which offers comprehensive characterization of representation encompassing all activity levels of the two variables without arbitrary binning or grouping. Despite popularity in other quantitative fields, this method of continuous mutual information calculation had just started to be utilized in neuroscience (Srivastava et al., 2017). We think the advantages of this method outweigh its computational encumbrance at least in studies of strongly continuous signals like ours, and encourage further attempts in the neuroscience community. Lastly, there was a potential caveat in our manipulation of mutual information after it was computed — to calculate the total representation in the electrodes studied, we summed up the

mutual information bits. Summation of mutual information here was not entirely justified, as we could not guarantee that the information obtained from different electrodes were not redundant. However, as it is hardly tractable to compute mutual information between high-dimensional variables, we hoped to provide a simple estimate for the total information in the system, assuming the level of non-redundancy did not differ too much among muscles or among electrodes. It would be useful to re-evaluate those hypotheses once techniques mature.

To summarize, we demonstrated the multiplexed and distributed nature of muscle representation on the cortical sheet of primary motor cortex, from the perspective of spatio-temporal information evolution. Representation constantly evolved in the course of single reaches and among different movements, but was mostly stable upon movement onset, likely reflecting functional needs. We also discovered temporal evolutions in the spatial gradient of body parts and in the information hotspot, emphasizing the added value of studying simultaneously space on cortical sheet and temporal evolution. Future directions include characterizing the representation stability at different spatial scales, linking evolving local networks to evolving representation at single sites, and developing online detection methods for informative sites to improve brain-machine-interfaces.

Acknowledgments

We thank Caroline M. Holmes and Ilya Nemenman for helpful discussions regarding the modified KSG mutual information estimator. We thank Stephanie Palmer, Jason MacLean and Yali Amit for helpful suggestions regarding analyses. We also thank the University of Chicago

research computing center for providing computing resources for intensive computations of mutual information. This study is supported by NIH R01 NS111982.

References

Aflalo, T. N., & Graziano, M. S. A. (2006). Possible origins of the complex topographic organization of motor cortex: reduction of a multidimensional space onto a two-dimensional array. *The Journal of Neuroscience : The Official Journal of the Society for Neuroscience*, *26*(23), 6288–6297. https://doi.org/10.1523/JNEUROSCI.0768-06.2006

Asanuma, H., & Sakata, H. (1967). Functional Organization of a Cortical Efferent System Examined with Focal Depth Stimulation in Cats. *Journal of Neurophysiology*, *30*(1), 35–54. https://doi.org/10.1152/jn.1967.30.1.35

Ben-Shaul, Y., Drori, R., Asher, I., Stark, E., Nadasdy, Z., & Abeles, M. (2004). Neuronal Activity in Motor Cortical Areas Reflects the Sequential Context of Movement. *Journal of Neurophysiology*, *91*(4), 1748–1762. https://doi.org/10.1152/jn.00957.2003

Ben-Shaul, Y., Stark, E., Asher, I., Drori, R., Nadasdy, Z., & Abeles, M. (2003). Dynamical organization of directional tuning in the primate premotor and primary motor cortex. *Journal of Neurophysiology*, *89*(2), 1136–1142. https://doi.org/10.1152/jn.00364.2002

Chakrabarty, S., & Martin, J. H. (2000). Postnatal development of the motor representation in primary motor cortex. *Journal of Neurophysiology*, *84*(5), 2582–2594. https://doi.org/10.1152/jn.2000.84.5.2582

Churchland, M. M., & Shenoy, K. V. (2007). Temporal complexity and heterogeneity of single-neuron activity in premotor and motor cortex. *Journal of Neurophysiology*, *97*(6), 4235–4257. https://doi.org/10.1152/jn.00095.2007

Darbellay, G. A., & Vajda, I. (1999). Estimation of the information by an adaptive partitioning of the observation space. *IEEE Transactions on Information Theory*, *45*(4), 1315–1321. https://doi.org/10.1109/18.761290

Evarts, E. V. (1968). Relation of pyramidal tract activity to force exerted during voluntary movement. *Journal of Neurophysiology*, *31*(1), 14–27. https://doi.org/10.1152/jn.1968.31.1.14

Ferrier, D. (1886). *The functions of the brain*. Smith, Elder.

Flament, D., & Hore, J. (1988). Relations of motor cortex neural discharge to kinematics of passive and active elbow movements in the monkey. *Journal of Neurophysiology*, *60*(4), 1268–1284. https://doi.org/10.1152/jn.1988.60.4.1268

Forget, R., & Lamarre, Y. (1987). Rapid elbow flexion in the absence of proprioceptive and cutaneous feedback. *Hum Neurobiol*, *6*(1), 27–37.

Fritsch, G., & Hitzig, E. (1870). On the electrical excitability of the cerebrum. In von Bonin G. *Some Papers on the Cerebral Cortex. Springfield, IL: Charles C Thomas*.

Georgopoulos, A. P., Merchant, H., Naselaris, T., & Amirikian, B. (2007). Mapping of the preferred direction in the motor cortex. *Proceedings of the National Academy of Sciences of the United States of America*, *104*(26), 11068–11072. https://doi.org/10.1073/pnas.0611597104

Glees, P., & Cole, J. (1950). recovery of skilled motor functions after small repeated lesions of motor cortex in macaque. *Journal of Neurophysiology*.

Graziano, M. S. A., Aflalo, T. N. S., & Cooke, D. F. (2005). Arm movements evoked by electrical stimulation in the motor cortex of monkeys. *Journal of Neurophysiology*, *94*(6), 4209–4223. https://doi.org/10.1152/jn.01303.2004

Graziano, M. S. A., Taylor, C. S. R., & Moore, T. (2002). Complex movements evoked by microstimulation of precentral cortex. *Neuron*, *34*(5), 841–851. https://doi.org/10.1016/S0896-6273(02)00698-0

Hatsopoulos, N. G., & Suminski, A. J. (2011). Sensing with the motor cortex. *Neuron*, *72*(3), 477–487. https://doi.org/10.1016/j.neuron.2011.10.020

Hatsopoulos, N. G., Xu, Q., & Amit, Y. (2007). Encoding of movement fragments in the motor cortex. *Journal of Neuroscience*, *27*(19), 5105–5114. https://doi.org/10.1523/JNEUROSCI.3570-06.2007

Holmes, C. M., & Nemenman, I. (2019). Estimation of mutual information for real-valued data with error bars and controlled bias. *Physical Review E*, *100*(2). https://doi.org/10.1103/PhysRevE.100.022404

Humphrey, D. R., Schmidt, E. M., & Thompson, W. D. (1970). Predicting Measures of Motor Performance from Multiple Cortical Spike Trains. *Science*, *170*(3959), 758–762.

Jackson, J. H. (1867). Remarks on the disorderly movements of chorea and convulsion, and on localisation. *Med Times Gazette*, *2*, 669–670.

Kim, J., & Park, H. (2012). Fast nonnegative tensor factorization with an active-set-like method. *High-Performance Scientific Computing: Algorithms and Applications*, *9781447124*, 311–326. https://doi.org/10.1007/978-1-4471-2437-5_16

Kola, T., Bader, B. W., Acar Ataman, E. N. M. N., Dunlavy, D., Bassett, R., Battaglino, C. J., Plantenga, T., Chi, E., & Hansen, S. (2017). *Tensor toolbox for MATLAB v. 3.0*.

Kraskov, A., Stögbauer, H., & Grassberger, P. (2004). Estimating mutual information. *Physical Review E - Statistical Physics, Plasmas, Fluids, and Related Interdisciplinary Topics*, *69*(6), 16. https://doi.org/10.1103/PhysRevE.69.066138

Martin, J. H., Engber, D., & Meng, Z. (2005). Effect of forelimb use on postnatal development of the forelimb motor representation in primary motor cortex of the cat. *Journal of*

Neurophysiology, *93*(5), 2822–2831. https://doi.org/10.1152/jn.01060.2004

Naito, E., Matsumoto, R., Hagura, N., Oouchida, Y., Tomimoto, H., & Hanakawa, T. (2011). Importance of precentral motor regions in human kinesthesia: a single case study. *Neurocase*, *17*(2), 133–147.

Nudo, R. J., Milliken, G. W., Jenkins, W. M., & Merzenich, M. M. (1996). *Use-Dependent Primary Motor Alterations of Movement Representations In Primary Motor Cortex of Adult Squirrel Monkeys*. *16*(2), 785–807.

Park, M. C., Belhaj-Saïf, A., & Cheney, P. D. (2004). Properties of primary motor cortex output to forelimb muscles in rhesus macaques. *Journal of Neurophysiology*, *92*(5), 2968–2984.

Park, M. C., Belhaj-Saïf, A., Gordon, M., & Cheney, P. D. (2001). Consistent features in the forelimb representation of primary motor cortex in rhesus macaques. *Journal of Neuroscience*, *21*(8), 2784–2792. https://doi.org/10.1523/jneurosci.21-08-02784.2001

Penfield, W., & Boldrey, E. (1937). Somatic Motor and Sensory Representation in Man. *Brain*, 389–443.

Penfield, W., & Rasmussen, T. (1950). *The cerebral cortex of man; a clinical study of localization of function.*

Pruszynski, J. A., Kurtzer, I., Nashed, J. Y., Omrani, M., Brouwer, B., & Scott, S. H. (2011). Primary motor cortex underlies multi-joint integration for fast feedback control. *Nature*, *478*(7369), 387–390. https://doi.org/10.1038/nature10436

Rathelot, J. A., & Strick, P. L. (2009). Subdivisions of primary motor cortex based on cortico-motoneuronal cells. *Proceedings of the National Academy of Sciences of the United States of America*, *106*(3), 918–923. https://doi.org/10.1073/pnas.0808362106

Rickert, J., Cardoso De Oliveira, S., Vaadia, E., Aertsen, A., Rotter, S., & Mehring, G. (2005). Encoding of movement direction in different frequency ranges of motor cortical local field potentials. *Journal of Neuroscience*, *25*(39), 8815–8824. https://doi.org/10.1523/JNEUROSCI.0816-05.2005

Rokni, U., Richardson, A. G., Bizzi, E., & Seung, H. S. (2007). Motor Learning with Unstable Neural Representations. *Neuron*, *54*(4), 653–666. https://doi.org/10.1016/j.neuron.2007.04.030

Sergio, L. E., Hamel-Pâquet, C., & Kalaska, J. F. (2005). Motor cortex neural correlates of output kinematics and kinetics during isometric-force and arm-reaching tasks. *Journal of Neurophysiology*, *94*(4), 2353–2378. https://doi.org/10.1152/jn.00989.2004

Srivastava, K. H., Holmes, C. M., Vellema, M., Pack, A. R., Elemans, C. P. H., Nemenman, I., & Sober, S. J. (2017). Motor control by precisely timed spike patterns. *Proceedings of the National Academy of Sciences of the United States of America*, *114*(5), 1171–1176. https://doi.org/10.1073/pnas.1611734114

Stark, E., Drori, R., & Abeles, M. (2009). Motor cortical activity related to movement kinematics exhibits local spatial organization. *Cortex*, *45*(3), 418–431. https://doi.org/10.1016/j.cortex.2008.03.011

Suminski, A. J., Tkach, D. C., & Hatsopoulos, N. G. (2009). Exploiting multiple sensory modalities in brain-machine interfaces. *Neural Networks*, *22*(9), 1224–1234. https://doi.org/10.1016/j.neunet.2009.05.006

Woolsey, C. N. (1952). Patterns of localization in precentral and" supplementary motor areas and their relation to the concept of a motor area. *Publ. Assoc. Res. Nerv. Ment. Dis.*, *30*, 238–264.

III. PROPAGATING SPATIO-TEMPORAL ACTIVITY PATTERNS ACROSS MOTOR CORTEX CARRY KINEMATIC INFORMATION

Abstract

Propagating spatio-temporal neural patterns are widely evident across sensory, motor and association cortical areas. However, it remains unclear whether any characteristics of neural propagation carry information about specific behavioral details. Here, we provide the first evidence for a link between the direction of cortical propagation and specific behavioral features of an upcoming movement on a trial-by-trial basis. We recorded local field potentials (LFPs) from multi-electrode arrays implanted in the primary motor cortex of two rhesus macaque monkeys while they performed a 2-D reach task. Propagating patterns were extracted from the information-rich high-gamma band (200-400Hz) envelopes in the LFP amplitude. We found that the exact direction of propagating patterns varied systematically according to initial movement direction, enabling kinematic predictions. Furthermore, characteristics of these propagation patterns provided additional predictive capability beyond the LFP amplitude themselves, which suggests the value of including mesoscopic spatio-temporal characteristics in refining brain machine interfaces.

Significance statement

Propagating activity patterns including waves are prevalent across cortical areas, but experimental evidence for their role in carrying behaviorally-relevant information is rare, and, when present, often reflects general behavioral state. This work provides the first evidence, to

our knowledge, of a spatially organized recruitment order of activity across the motor cortical sheet that informs details of the upcoming movement. Furthermore, characteristics of propagation provide additional predictive power in decoding kinematics beyond information-rich activity amplitudes. The non-redundant movement-specific information exhibited by these propagating patterns not only has scientific implications for the functional organization of motor cortex but also holds potential to aid translational brain machine interface research.

Introduction

The primary motor cortex (M1) is well known to possess a somatotopic organization such that movement representations of different body parts are segregated spatially across the cortical sheet (Penfield & Boldrey, 1937). However, particularly in the upper limb area of M1, the spatial organization is rather crude such that particular limb segment representations are highly distributed and partially overlapping with other limb segment representations (Park et al., 2004). Moreover, the somatotopic perspective is a static view of the function of M1 and does not consider both time and space. We have recently demonstrated that spatially organized propagating patterns of excitability signal the initiation of movement but do not specify the details of the particular movement (Balasubramanian et al., 2020, 2022). These propagating patterns of excitability were observed in the attenuation of beta oscillation (15-35 Hz) amplitude of the local field potential (LFP). Here, we examined high-gamma band (200-400 Hz) amplitude prior to movement execution and observed planar propagation in the onset times of high-gamma amplification across different sites in M1. Unlike beta oscillation attenuation propagation, however, the propagating

direction of high-gamma amplification times carried kinematic information about the upcoming movement. High-gamma amplitude is known to be a reasonable proxy for multi-unit activity (Flint, Ethier, et al., 2012; Flint, Lindberg, et al., 2012; Zhuang et al., 2010), and, therefore, these results suggest that a spatially organized recruitment order of neural activity across the cortical sheet occurs prior to executing movements, and properties of this recruitment order specify the detailed kinematics of the upcoming movement.

Methods

Electrophysiology

Neural recordings were collected from two male rhesus macaques (*Macaca Mulatta*), Bx and Ls. They were each implanted with a set of dual 64-electrode Utah multi-electrode arrays (Blackrock Microsystems, Salt Lake City, UT) in the left primary motor cortex (see Supplementary Fig. 3.S1). The electrode lengths were 1.5mm for Bx and 1mm for Ls, with a uniform inter-electrode distance of 400μm in the 8-by-8 grid. The arrays corresponded to the arm/hand areas of the limb trained for the task, as confirmed by electrically stimulating the cortex during surgery with surface electrodes and observing corresponding twitches prior to array implantation. All procedures regarding surgery, animal training and data collection were approved by the University of Chicago Institutional Animal Care and Use Committee (IACUC) and obey the Guide for the Care and Use of Laboratory Animals.

Behavioral task

The animals were trained to perform a reach task in different directions with their right upper limb constrained by a 2D exoskeletal robot (BKIN Technologies). All the reach directions were on a horizontal plane roughly at the height of their elbows when their upper limbs were naturally hanging. They performed the task by moving the joystick at the tip of the robot, while receiving simultaneous visual feedback of the cursor position on the screen in front of them. The task involves a hold period (600ms for Ls and 1000ms for Bx) during which the animal held the joystick steadily keeping the cursor within a central target. The peripheral target then appeared indicating the desired reach location. The animal moved the joystick to direct the cursor to the peripheral target. Each target had a radius of 1cm for Ls and 0.75cm for Bx; the distance from the central target to the peripheral target was 6cm For Ls and 5.5cm for Bx. The peripheral target could appear in one of 8 possible locations on a circle (in 45° intervals counterclockwise from 0° to 315°, where rightward movement was 0° and forward movement was 90°). A trial was considered successful once the cursor reached the peripheral target and remained in the target for a period of time (100ms for Ls, 400 - 600ms for Bx), upon which the animal received juice reward. In total, there were 3 sessions for each monkey.

Data collection and preprocessing

Neural signals were collected with Blackrock Microsystems (Salt Lake City, UT), bandpass filtered from 0.3Hz to 7.5 kHz with Butterworth filter and then digitized at 30kHz. For local field potentials, the 30kHz signal was further low-pass filtered below 500Hz with a Butterworth filter and downsampled to 2kHz. For multi-unit activity (MUA), the 30kHz signal was high-passed above 250Hz with a Butterworth filter and threshold crossing events were found when the voltage crossed negative 5.5 times of the root-mean-square (RMS).

Extracting signals from high-gamma band and beta band

From the 2kHz local field potentials, the high-gamma band signals were extracted by bandpass filtering within 200Hz - 400Hz with a Butterworth filter; the beta band signals were extracted by bandpass filtering within a monkey-specific range that corresponded to individual peak frequencies in the beta band power spectrum (18 - 24Hz for Ls and 28 - 34Hz for Bx). All band-pass filters had zero phase distortion. From those band-pass filtered signals, we computed the Hilbert transformation to obtain the amplitude envelopes. Individual trials were aligned on movement onset defined as the time point where 15% of the peak speed was reached for that trial.

Comparison of high-gamma band vs. multi-unit activity

The MUAs from different trials were aligned on movement onset and binned in 1ms windows, after which moving averages were computed in sliding windows of 150ms (in steps of 1ms). The high-gamma signal used for comparison with MUA was low-passed below 10Hz to match the smoothing of the MUA. Then, we compared the similarity of the two signal types based on the correlation of tuning curves and cross-correlation of single-trial activity.

Presence of modulation: for each signal type, the mean time-resolved activity was computed for each peripheral target for each electrode. For each electrode and each target direction, the baseline mean and standard deviation was computed over a time window of -700 to -250ms with respect to movement onset. If the average activity deviated from the baseline mean by at least 3

standard deviations at any time point between -200ms to 500ms (with respect to movement onset) for any target direction, then we considered this electrode to be modulated.

Robust firing: for MUA, the mean time-resolved activity was computed for each peripheral target for each electrode. If the maximal instantaneous average firing rate exceeded 1Hz at any time point between -200ms to 500ms (with respect to movement onset) for any target direction, then we considered this electrode to have robust firing.

Correlation of tuning curves of MUA and high-gamma activity: for each signal type, the mean time-resolved activity was computed for each peripheral target for each electrode, and the modulation strength for each target direction was determined by the integral of activity between -200ms to 500ms with respect to movement onset. The tuning curve was composed of eight modulation strengths, one for each target direction. The Pearson correlation between tuning curves of high-gamma and MUA was computed for each electrode that was modulated and had robust firing.

Cross-correlation of single-trial MUA and high-gamma activity: for each electrode that was modulated and had robust firing, the Pearson correlation between the two signal types was computed within a wide range of lags from -600ms to 600ms in steps of 5ms.

Computation of circular statistics

Descriptions of propagation directions and movement directions require proper treatments of angular variables. We computed angular means, medians and standard errors of the mean based on (Fisher et al., 1993; Jammalamadaka & Sengupta, 2001; Zar, 2009), implemented in the pycircstat package in python (https://github.com/circstat/pycircstat/tree/master/pycircstat).

Briefly, the angular mean is the direction of the mean of the vectors $(\cos(\alpha_i), \sin(\alpha_i))$, where α_i represent each angle in the distribution. The angular median is the angle which has the minimum total distance to all other angles in the distribution (in the case of even number of samples, it's the mean of the two angles with the minimal distance). The circular standard error of the mean is computed by halving the 68.27% confidence interval of the mean estimation - it only exists when data has enough concentration around the mean (in Zar, 2009, Equations 26.23-26).

As for statistical tests for multisample analysis of circular data (eg. different groups of propagation directions), we tested whether different groups of angles shared a common median, using a test suggested by Fisher (Fisher et al., 1993). This is a non-parametric test, serving as a circular analogue of the Kruskal-Wallis test (Berens, 2009). It was implemented with the same pycircstat package mentioned above.

Processing steps for denoising single trial activities

Given the temporal variability of high-gamma band and beta band amplitudes on individual trials, a series of steps were performed to denoise single-trial amplitudes. First, trials from multiple daily sessions of the same task of the same monkey were pooled together. For each pooled dataset, only trials with a reaction time within a canonical range were kept (200 - 600ms for Bx and 0 - 400ms for Ls), to ensure relative homogeneity of the behaviors. Next, we randomly divided the trials into a training set (90%) and a test set (10%). The complete procedures that will be explained in the following paragraphs are illustrated in Figure 3.1. We z-scored the activities for each electrode with signal mean and standard deviation from the baseline period of the training set (baseline period was defined as -700ms to -400ms for high-gamma and

-900ms to -600ms relative to movement onset for the beta band, during which signals were relatively steady on average). Then, we rearranged the training data to form a 2-D matrix (where all timepoints of all electrodes of one trial were flattened into one long column vector and different columns represented different trials) and reduced the dimensionality from 307328 (128 electrodes x 2401 time points) to 200 with principal component analysis (PCA, accounting for 30.7% ~ 39.4% of total variance). We applied the same transformations to the test set (accounting for 13.0% ~ 15.5% of total variance). This PCA step was used to reduce the number of parameters for later training of neural networks. We experimented with more principal components with this PCA step (400 and 800 components)- while they accounted for more total variance in the training set (40.6% ~ 59.1% with 400 components and 58.2% ~ 91.5% with 800 components), the total variance accounted for in the test set only increased minimally (13.8% ~ 16.3% with 400 components and 15.1% ~ 17.8% with 800 components), and the final denoising performance remained similar. We decided to go with 200 components primarily due to the limited trial count we had for training the later neural network.

To denoise the signal, we used a variant of autoencoders called the contractive autoencoder (Rifai et al., 2011) (implemented in Tensorflow with adaptions from https://github.com/zaouk/contractive_autoencoders). Briefly, the contractive autoencoder aims to reconstruct each 200-dimensional trial vector $\boldsymbol{Env_{reduced}}$ faithfully through operations of three hidden layers while reducing the sensitivities of the hidden layer representations with respect to the inputs (the latter is termed 'Jacobian loss') (see Equation 3.1 and 3.2: Equation 3.1 describes the total loss as a weighted sum of the reconstruction loss and Jacobian loss, while Equation 3.2 spells out the Jacobian loss to be the squared partial derivatives of the hidden layer activities with respect to the inputs). The autoencoder was fitted with a 2:1 cross-validation scheme for early

stopping using the 90% training set and then evaluated on the 10% test set. Results reported here were obtained with the following hyperparameters: tradeoff between Jacobian loss and reconstruction loss $\lambda = 0.1$, learning rate = 0.0001 and batch size = 8; hidden layers sizes were 100, 50, 100, with sigmoid transfer functions used in the encoder (f, for contraction) part and linear functions used in the decoder (g, for expansion) part of the autoencoder. This set of parameters was chosen to achieve a relatively proper level of compression and stable denoising, and the denoising performance and downstream results was quite stable across a wide range of hyperparameters we experimented. All bolded variables in this manuscript denote vectors (for example input vector $\boldsymbol{Env_{reduced}}$ here).

$$Loss_{total} = \sum \left(Loss_{recon}(\boldsymbol{Env_{reduced}}, g\left(f(\boldsymbol{Env_{reduced}})\right)) + \lambda \, Loss_{Jacobian} \right)$$

Equation 3.1

$$Loss_{Jacobian} = \sum_{i,j} \left(\frac{\partial h_j(\boldsymbol{Env_{reduced}})}{\partial \boldsymbol{Env_{reduced}}_i} \right)^2$$

Equation 3.2

After denoising with an autoencoder, we transformed the reconstructed 200-dimensional trial vectors back to the original space with the inverse PCA transformation. Notably, neither PCA nor autoencoder had any information regarding the spatial locations of the electrodes. Finally, we low-passed each temporal trace with a cutoff frequency of 5Hz for smoothing purposes.

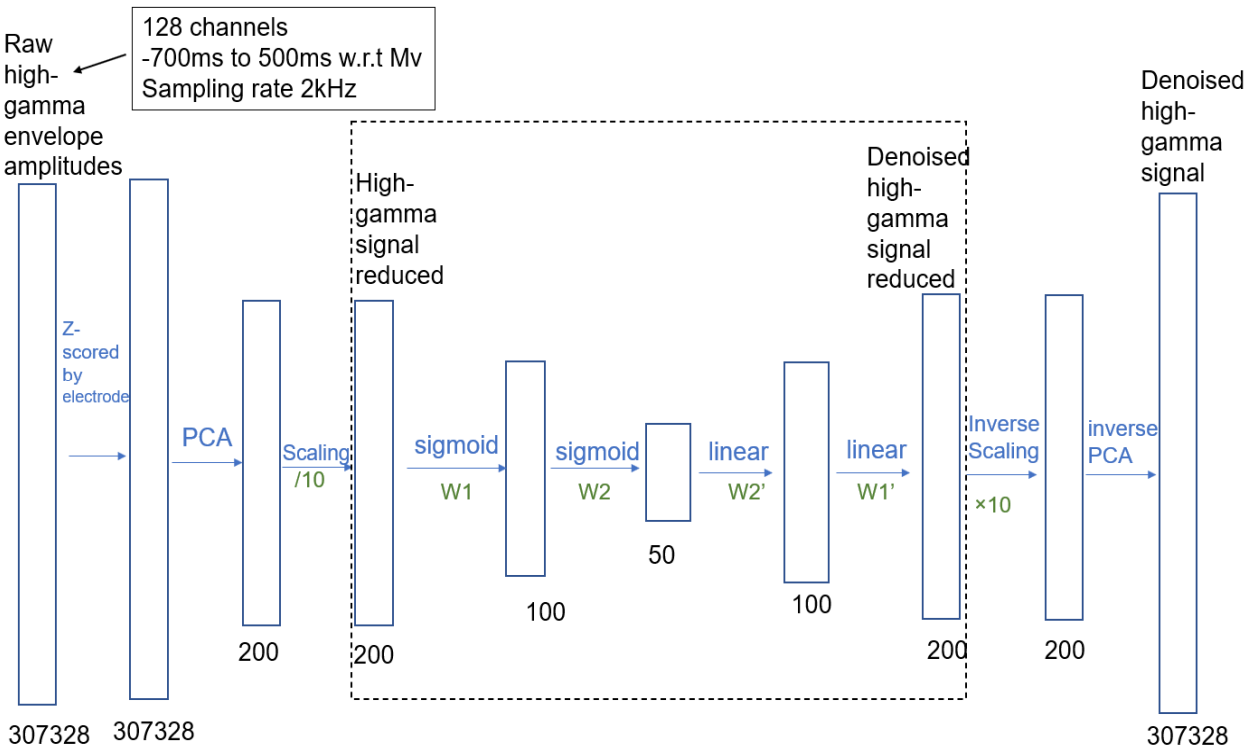

Figure 3.1 Procedure diagram for denoising high-gamming signals. Steps of denoising are illustrated in this flowchart, with sizes of dimensionality on the bottom. Briefly, for any trial, raw high-gamma envelope amplitudes from 1.2s of time in 128 channels were concatenated into a long vector, which was then z-scored per electrode. Then principal component analysis (PCA) was performed where the first 200 components were selected. Next, we scaled the data by 1/10. Then data is fed into a contractive autoencoder (in dotted box), which included two 'compressing' layers with sigmoid transfer functions and two 'expansion' layers with linear transfer functions, sequentially. Weights in the linear functions were transposed from those in the sigmoid functions. Then, data is scaled by 10 times and inversely transformed by the previous PCA to recover the dimensionality. See text for details.

Characterizing spatio-temporal patterns of single-trial activities

The high-gamma amplitude envelopes from different electrode locations tended to amplify around movement initiation but at slightly different times. To quantify the exact time of amplification for a particular electrode, we took the first derivative of the smoothed denoised

envelopes described above and took the time point of maximum within the canonical amplification window (-300ms to 100ms) as the amplification time, as long as that maximum exceeded the baseline mean by at least 2 baseline standard deviations (baseline was defined as [-700ms, -400ms] relative to movement onset). Once we computed those amplification times for different electrodes in a trial, we excluded outlier amplification times (outlier times defined as times that deviated from the median time by more than 6 times of the median of the deviations). If there were more than 33% of electrodes left, we fit the amplification times for all electrodes ($\boldsymbol{t_{amp}}$) with their x, y physical coordinates using linear regression (i.e. 2D planar fit). In Equation 3.3, β_0 denotes the offset and β_1 and β_2 denote the coefficients for x, y axes. The direction of the propagation $\varphi_{propagation}$ is determined by the angle formed by the two coefficients (Equation 3.4). The speed of the propagation $v_{propagation}$ is computed with Equation 3.5 with the inter-electrode distance $d_{interelec} = 0.4mm$.

$$\boldsymbol{t_{amp}} = \beta_0 + \beta_1 \boldsymbol{x} + \beta_2 \boldsymbol{y}$$

Equation 3.3

$$\varphi_{propagation} = \arctan\left(\frac{\beta_2}{\beta_1}\right)$$

Equation 3.4

$$v_{propagation} = \left(\frac{1}{\sqrt{\beta_1^2 + \beta_2^2}}\right) \cdot d_{interelec}$$

Equation 3.5

The fit for each trial was evaluated based on the fraction of variance explained (i.e. R^2) of the linear regression ($R^2_{propagation}$). To determine whether the fit was statistically significant, we randomly shuffled electrode locations 500 times for each trial, pooled together the shuffled $R^2_{propagation}$ values from all trials and determined an overall $R^2_{propagation}$ threshold based on the top 5% cutoff of shuffled $R^2_{propagation}$ values. A trial with less than 33% of electrodes left for planar regression was automatically considered an insignificant trial.

Decoding velocities with spatio-temporal patterns

This section explains the processes of evaluating whether the spatio-temporal propagating patterns could predict velocities.

For the *spatio-temporal model*, we used all parameters characterizing the spatio-temporal patterns ($\boldsymbol{v_{propagation}}, sin(\boldsymbol{\varphi_{propagation}}), \cos(\boldsymbol{\varphi_{propagation}}), \boldsymbol{R^2_{propagation}}$), here bolded as they are now vectors for all trials) to predict the x and y components of the hand velocities ($\boldsymbol{v_x}, \boldsymbol{v_y}$) respectively, using a generalized linear model (GLM) with linear link and Gaussian family distribution. The formulation is identical to linear regressions, except that the solution is found with iteratively reweighted least squares (IRLS) method. In Equation 3.6 and 3.7, the m and l denote the medial and lateral arrays respectively, while the x and y denote the x and y components of the velocity respectively. A different model is computed for different timepoints with respect to movement onset from all trials, which is noted by t_i in the equations ($t_i \in [-200,200]$ms), so that we could determine when those spatio-temporal variables attained the best predictive power.

spatio-temporal model:

$$\boldsymbol{v_{x\_t_i}} = \beta_{c\_x\_t_i} + \beta_{\sin\_x\_l\_t_i} sin(\boldsymbol{\varphi_{propagation\_l}}) + \beta_{\cos\_x\_l\_t_i} \cos(\boldsymbol{\varphi_{propagation\_l}}) + \beta_{v\_x\_l\_t_i} \boldsymbol{v_{propagation\_l}} + \beta_{fit\_x\_l\_t_i} \boldsymbol{R^2_{propagation\_l}} + \beta_{\sin\_x\_m\_t_i} sin(\boldsymbol{\varphi_{propagation\_m}}) + \beta_{\cos\_x\_m\_t_i} \cos(\boldsymbol{\varphi_{propagation\_m}}) + \beta_{v\_x\_m\_t_i} \boldsymbol{v_{propagation\_m}} + \beta_{fit\_x\_m\_t_i} \boldsymbol{R^2_{propagation\_m}}$$

Equation 3.6

$$\boldsymbol{v_{y\_t_i}} = \beta_{c\_y\_t_i} + \beta_{\sin\_y\_l\_t_i} sin(\boldsymbol{\varphi_{propagation\_l}}) + \beta_{\cos\_y\_l\_t_i} \cos(\boldsymbol{\varphi_{propagation\_l}}) + \beta_{v\_y\_l\_t_i} \boldsymbol{v_{propagation\_l}} + \beta_{fit\_y\_l\_t_i} \boldsymbol{R^2_{propagation\_l}} + \beta_{\sin\_y\_m\_t_i} sin(\boldsymbol{\varphi_{propagation\_m}}) + \beta_{\cos\_y\_m\_t_i} \cos(\boldsymbol{\varphi_{propagation\_m}}) + \beta_{v\_y\_m\_t_i} \boldsymbol{v_{propagation\_m}} + \beta_{fit\_y\_m\_t_i} \boldsymbol{R^2_{propagation\_m}}$$

Equation 3.7

To obtain the *shuffle control model*, we randomly shuffled the hand velocities across trials and refitted the velocity prediction models.

All models were fit and evaluated with a 10-fold cross-validation scheme. We adapted the definition of R^2 and arrived at a composite fit measure $R^2_{v\_pred\_composite}$ for each pair of models, taking into account performances of $\boldsymbol{v_x}$ and $\boldsymbol{v_y}$ predictions simultaneously. In Equation 3.8, $\widehat{\boldsymbol{v_x}}$ denotes the estimated $\boldsymbol{v_x}$, while $\overline{\boldsymbol{v_x}}$ denotes the average $\boldsymbol{v_x}$ (here suffix t_i is ignored from all variables for simplicity).

$$R^2_{v\_pred\_composite} = 1 - \frac{\sum((\boldsymbol{v_x} - \widehat{\boldsymbol{v_x}})^2 + (\boldsymbol{v_y} - \widehat{\boldsymbol{v_y}})^2)}{\sum((\boldsymbol{v_x} - \overline{\boldsymbol{v_x}})^2 + (\boldsymbol{v_y} - \overline{\boldsymbol{v_y}})^2)}$$

Equation 3.8

To compare the time-resolved performance of the *spatio-temporal model* versus the *shuffle control model*, we performed a single-tailed Wilcoxon test for the $R^2_{v\_pred\_composite}$ at the optimal time point for the *spatio-temporal model*.

Finally, to evaluate the relative importance of those spatio-temporal variables, we also computed reduced models that contained only a subset of the spatio-temporal propagating characteristics. For example, the *direction-only spatio-temporal model* only contained direction variables; the *speed-only spatio-temporal model* only contained speed variables; and the *fit-only spatio-temporal model* only contained R^2 variables. The rest is the same as described above with the *spatio-temporal model*. In Equation 3.9 to 3.11, again, the m and l denote the medial and lateral arrays respectively, while the x and y denote the x and y components of the velocity respectively; a different model is computed for different timepoints with respect to movement onset from all trials, which is noted by t_i in the equations ($t_i \in [-200,200]$ms).

direction-only spatio-temporal model (here we wrote down only the formulations for the x component of the velocity for brevity; same below):

$$\boldsymbol{v_{x\_t_i}} = \beta_{c\_x\_t_i} + \beta_{\sin\_x\_l\_t_i} sin\left(\boldsymbol{\varphi_{propagation\_l}}\right) + \beta_{\cos\_x\_l\_t_i} \cos\left(\boldsymbol{\varphi_{propagation\_l}}\right) + \beta_{\sin\_x\_m\_t_i} sin\left(\boldsymbol{\varphi_{propagation\_m}}\right) + \beta_{\cos\_x\_m\_t_i} \cos\left(\boldsymbol{\varphi_{propagation\_m}}\right)$$

Equation 3.9

speed-only spatio-temporal model:

$$\boldsymbol{v_{x\_t_i}} = \beta_{c\_x\_t_i} + \beta_{v\_x\_l\_t_i} \boldsymbol{v_{propagation\_l}} + \beta_{v\_x\_m\_t_i} \boldsymbol{v_{propagation\_m}}$$

Equation 3.10

fit-only spatio-temporal model:

$$\boldsymbol{v_{x\_t_i}} = \beta_{c\_x\_t_i} + \beta_{fit\_x\_l\_t_i}\boldsymbol{R}^{\boldsymbol{2}}_{\boldsymbol{propagation\_l}} + \beta_{fit\_x\_m\_t_i}\boldsymbol{R}^{\boldsymbol{2}}_{\boldsymbol{propagation\_m}}$$

Equation 3.11

Decoding velocities with envelopes and spatio-temporal patterns

To evaluate whether the spatio-temporal patterns contained additional information regarding kinematics that was non-redundant with what was contained in the high-gamma amplitude envelopes themselves, we built GLM models containing (a) only the instantaneous amplitude envelopes ('*envelope-only model'*); (b) only the spatio-temporal variables – including both 1st order variables and 2nd order interactions ('*spatiotemporal-1stAnd2nd-only model'*); and (c) both instantaneous amplitude envelopes and 1st & 2nd order spatio-temporal variables ('*envelope+spatiotemporal1stAnd2nd model*').

The *envelope-only model* was lag-specific, meaning that we used instantaneous envelopes at a particular fixed lag to the hand velocities, to predict the hand velocities at all time points (0ms - 200ms w.r.t. movement onset) of all trials; the *envelope+spatiotemporal1stAnd2nd models* was also lag-specific given that it contained the instantaneous envelopes. The lags are denoted with Δt_i in the equations below ($\Delta t_i \in [-300,100]$ms).

In contrast, the *spatiotemporal-1stAnd2nd-only model* was not lag-specific, as only one set of spatio-temporal variables was computed for any given trial. The 2nd order interactions terms were constructed from the product of each pair of z-scored 1st order spatio-temporal variables. The same model was also used to predict hand velocities of all time points (0ms - 200ms w.r.t.

movement onset) of all trials, instead of only at a particular time point as was done in the previous section ("Decoding velocities with spatio-temporal patterns").

envelope-only model (where p denotes electrode number and $\boldsymbol{Env}$ denotes instantaneous amplitude envelope):

$$\boldsymbol{v_{x\_\Delta t_i}} = \beta_{c\_x\_\Delta t_i} + \sum_{p=1}^{128} \beta_{env\_x\_\Delta t_i\_p} \cdot \boldsymbol{Env_p}$$

Equation 3.12

$$\boldsymbol{v_{y\_\Delta t_i}} = \beta_{c\_y\_\Delta t_i} + \sum_{p=1}^{128} \beta_{env\_y\_\Delta t_i\_p} \cdot \boldsymbol{Env_p}$$

Equation 3.13

spatiotemporal-1stAnd2nd-only model (where $\mathbf{Spt_m}$ denotes the m-th 1st order spatio-temporal variable among a total of 8 variables from both arrays, $\odot$ denotes element-wise product):

$$\boldsymbol{v_x} = \beta_{c\_x} + \sum_{m=1}^{8} \beta_{spt\_x\_m} \cdot \boldsymbol{Spt_m} + \sum_{m \neq n} \beta_{spt\_x\_m\_n} \cdot \boldsymbol{Spt_m} \odot \boldsymbol{Spt_n}$$

Equation 3.14

$$\boldsymbol{v_y} = \beta_{c\_y} + \sum_{m=1}^{8} \beta_{spt\_y\_m} \cdot \boldsymbol{Spt_m} + \sum_{m \neq n} \beta_{spt\_y\_m\_n} \cdot \boldsymbol{Spt_m} \odot \boldsymbol{Spt_n}$$

Equation 3.15

envelope+spatiotemporal1stAnd2nd model:

$$\boldsymbol{v_{x\_\Delta t_i}} = \beta_{c\_x\_\Delta t_i} + \sum_{p=1}^{128} \beta_{env\_x\_\Delta t_i\_p} \cdot \boldsymbol{Env_p} + \sum_{m=1}^{8} \beta_{spt\_x\_m} \cdot \boldsymbol{Spt_m}$$

$$+ \sum_{m \neq n} \beta_{spt\_x\_m\_n} \cdot \boldsymbol{Spt_m} \odot \boldsymbol{Spt_n}$$

Equation 3.16

$$\boldsymbol{v_{y\_\Delta t_i}} = \beta_{c\_y\_\Delta t_i} + \sum_{p=1}^{128} \beta_{env\_y\_\Delta t_i\_p} \cdot \boldsymbol{Env_p} + \sum_{m=1}^{8} \beta_{spt\_y\_m} \cdot \boldsymbol{Spt_m}$$

$$+ \sum_{m \neq n} \beta_{spt\_y\_m\_n} \cdot \boldsymbol{Spt_m} \odot \boldsymbol{Spt_n}$$

Equation 3.17

Except for the exact variables used in the model, all model specifications, numerical computations, cross-validation scheme and composite performance measure were the same as the previous section "Decoding velocities with spatio-temporal patterns".

Afterwards, we statistically tested whether the spatio-temporal variables added to the amplitude envelopes improved kinematic prediction. We first picked the best lag for the *envelope-only model* (i.e. the *envelope-only model* with the best mean $R^2_{v\_pred\_composite}$ across folds), then used the same lag for the *envelope+spatiotemporal1stAnd2nd model*. We compared the $R^2_{v\_pred\_composite}$ values obtained for both models with a single-tailed Wilcoxon test.

Lastly, we tested whether it was crucial to have the correct spatio-temporal variables corresponding to each trial to improve hand velocity prediction over the amplitude envelopes.

For that, we randomly shuffled the spatio-temporal variables among trials 1000 times, supplementing the correct instantaneous amplitude envelopes to predict hand velocities. Each shuffled prediction was fit and evaluated with a 4-fold scheme; upon averaging across folds, it forms a $R^2_{v\_pred\_composite}$ distribution consisting of 1000 samples. A top 5% threshold was determined from the distribution of shuffled $R^2_{v\_pred\_composite}$ values. We compared that threshold with the real $R^2_{v\_pred\_composite}$ from unshuffled spatio-temporal variables and amplitude envelopes after averaging across its 10 folds.

Results

Spatially organized amplification in the high-gamma envelope upon movement

Two rhesus macaques (Bx and Ls) were trained to perform reach tasks with their right upper limbs constrained in a 2D exoskeletal robot with the hand holding a joystick. In this reach task, they were required to hold the joystick stably for a length of time (600ms for Ls and 1000ms for Bx) at a center hold target, then move the joystick to one of eight peripheral targets upon presentation of a peripheral target (see the inset in Fig. 3.2 a). The mean (standard deviation) reach duration across trials was 669.8ms (253.0 ms) and 372.8ms (162.8ms) for Bx and Ls, respectively, and mean reaction time was 392.7ms (85.7ms) and 186.7ms (74.9ms) for Bx and Ls, respectively. While they were performing the task, we recorded multi-unit activity (MUA) and local field potentials (LFPs) from two 64-electrode arrays implanted in M1 (see Supplementary Fig. 3.S1 top panels for implant locations). We filtered LFPs from 200Hz to

400Hz and took the amplitude of their Hilbert transform – this is the signal which we refer to as high-gamma envelopes. Trial-averaged high-gamma envelopes were different for different reach directions (Fig. 3.2 a), exhibiting directional tuning. Tuning curves for the high-gamma envelopes and MUA were generally similar in shape for the same electrode (Fig. 3.2 b compares turning curves for a representative electrode). We correlated the tuning curves between MUA and high-gamma activity for the same electrodes, and found that the mean (standard deviation) tuning correlation was 0.75 (0.35) for Bx and 0.80 (0.29) for Ls (Fig. 3.2 c). We also looked at the cross-correlation of MUA and high-gamma activity on a single trial basis over a wide range of lags. In general, high-gamma activity preceded MUA – the mean (over electrodes) lag at peak correlation for each session ranged from 15.4 to 34.2ms across sessions for Bx and from 32.6 to 83.3ms for Ls; the mean peak correlation of the time-series ranged from 0.32 to 0.36 for Bx and from 0.41 to 0.57 for Ls.

While trial-averaged high-gamma envelopes generally exhibited directional-specificity and amplification upon movement onset, it was not possible to extract meaningful information from single-trial envelopes because of weak signal-to-noise. Thus, we denoised single-trial envelopes by using a contractive autoencoder (Rifai et al., 2011) and then smoothed the envelopes (Fig. 3.2 d) (see Methods for details). Note that all the electrodes at all timepoints were concatenated into a long vector for denoising so that no spatial information was used in the denoising process. The high-gamma envelopes from different electrode locations tended to amplify around movement initiation but at different times. To precisely quantify the amplification time for each electrode, we took the first derivative of the smoothed envelope and determined the maximum-attaining time within a time window of [-300ms, 100ms] relative to movement onset (Fig. 1d continued). We computed the median amplification time across electrodes within a trial and then averaged

those medians across trials. For Bx, the mean (standard deviation) of the median amplification times was -120.3ms (45.6ms) for the lateral array and -64.4ms (108.4ms) for the medial array. For Ls, the mean median amplification time was -81.1ms (60.0ms) for the lateral array and -81.5ms (67.9ms) for the medial array.

We then sought to characterize the spatial organization of these amplification times across each cortical array by fitting the amplification times to a 2D plane from which three propagating parameters were extracted: the direction of propagation, the speed of propagation, and the fitness (R^2) of the planar fit (Fig. 3.3 a middle and right panels). It should be emphasized that the definition of spatial patterning in our work contains only the times of amplification on each electrode and not their amplitudes. To determine statistical significance of the planar fit, we randomly shuffled the locations of the electrodes 500 times for each trial and fit a plane to each shuffle to form an overall distribution of shuffled R^2 values. We determined the significant threshold of R^2 as the top 5 percentile of the shuffled R^2 values - if the actual R^2 exceeded that threshold, we took that as a significant planar propagating pattern (see Methods for details). For the lateral arrays, 1235 out of 2460 trials (50%) exhibited significant planar propagation patterns for Bx and 898 out of 1050 trials (86%) for Ls exhibited significant planar propagation patterns. For the medial arrays, fewer trials exhibited significant planar propagation patterns in general (408 out of 2460 trials or 17% for Bx, 482 out of 1050 trials or 46% for Ls).

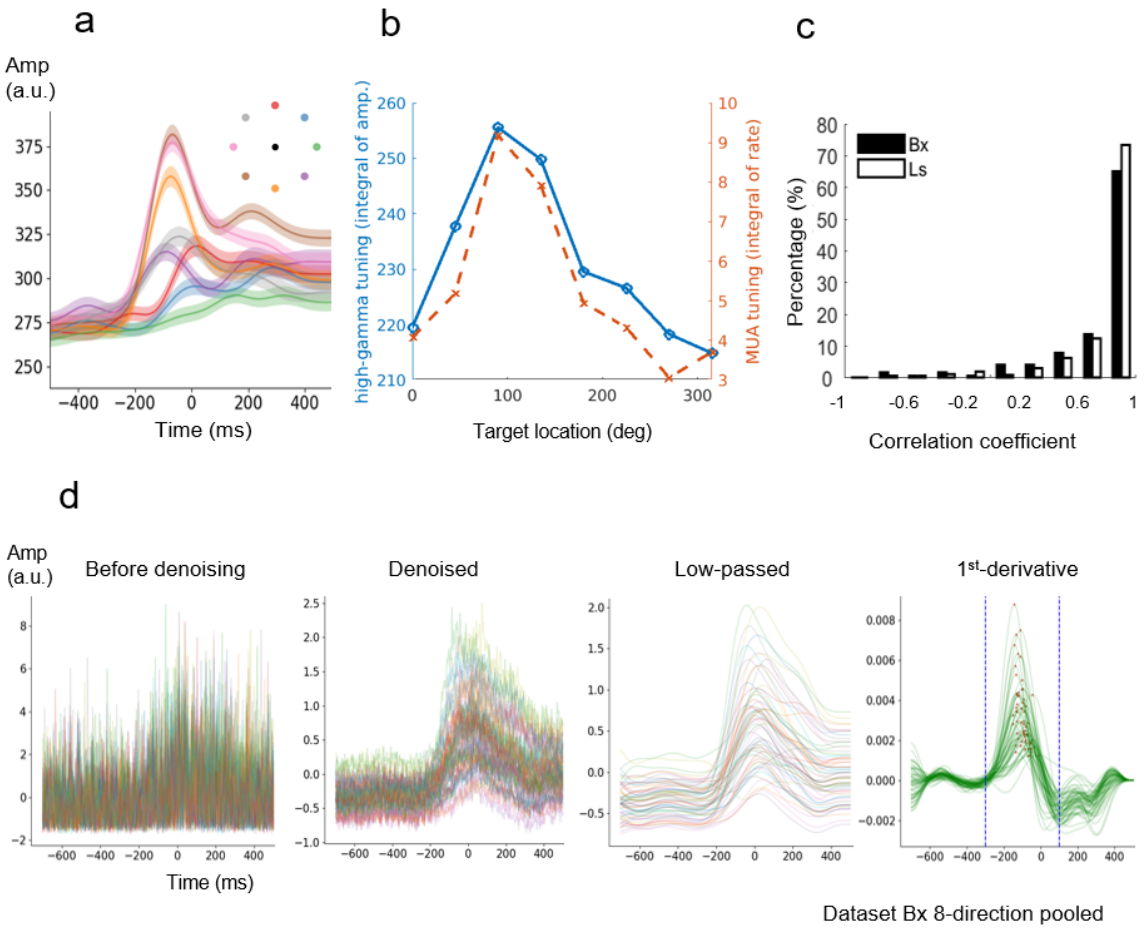

Figure 3.2 Processing information-rich high-gamma envelopes. **a**. Trial-averaged high-gamma amplitude envelopes amplify right before movement onset (0ms), modulating with target reach directions (targets distinguished by different colors). Results from a representative electrode are shown. Error shades represent standard error of mean (sem). Inset shows the target locations in different colors. **b**. Tuning properties of the high-gamma envelopes (in blue) closely track those of multi-unit activities (MUA in orange) on a representative channel. **c**. Distribution of correlation coefficients between the tuning curves of high-gamma envelopes and tuning curves of MUAs on the same electrodes, for monkey Bx (in black) and monkey Ls (in white). **d**. Sequential steps for processing single trial high-gamma envelopes, where each trace represents a single electrode: from left to right, envelopes are z-scored by electrode baselines, then PCA-ed and denoised with an autoencoder, and then low-passed below 5Hz. The amplification times (red dots) were determined from the maximums of their 1st-derivatives (in green) within the time window of interest (blue dotted window).

Movement-specific propagation patterns

As the monkey reached for targets in different directions (Fig. 3.3 a,b left panels), the propagating directions of the high-gamma envelope varied (Fig. 3.3 a,b middle and right panels), indicating that there might be movement- or goal-related information expressed in the propagation patterns. There were, in fact, systematic and significant differences in propagation direction ($p<0.001$ for both monkeys, non-parametric test for common median for multiple groups of angles) across trials with significant planar propagation in the lateral arrays (Fig. 3.4 a,b, top panels). The probability density (Supplementary Fig. 3.S2 a, top panel) and mean propagating directions for monkey Bx primarily formed two modes (0,45,90,135 deg targets versus 180,225,270,315 deg targets; see Methods for target degree assignment), each corresponding to four adjacent reach directions, one centered ~210 degrees and one centered ~0 degrees (Fig. 3.4 a, bottom panel). We also examined the probability density of propagation speed for the significant trials (Supplementary Fig. 3.S2 a, bottom panel), which also differed by reach directions and followed similar grouping as the propagating directions (see Table 3.1a for descriptive statistics of propagation characteristics for Bx). For monkey Ls, the probability densities of propagation direction and speed did not exhibit clear clustering (Supplementary Fig. 3.S2 b) although mean propagation directions clustered into two modes albeit not as distinct as with Bx (Fig. 3.4 b, bottom panel; see Table 3.1b for descriptive statistics of propagation characteristics for Ls).

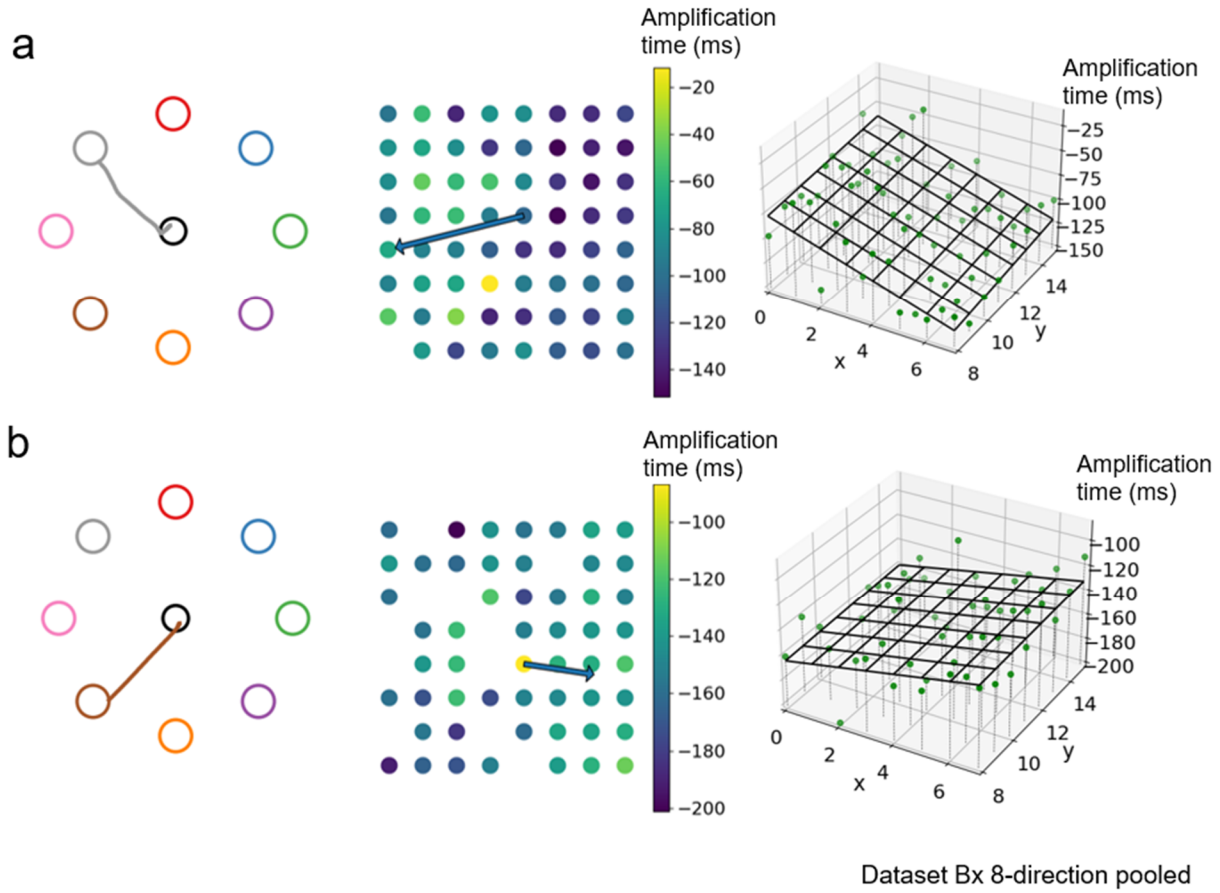

Figure 3.3 Single-trial propagation directions were different for different movement directions. **a** & **b** are two different trials for monkey Bx. Left: movement path plotted on the target map. Middle: the amplification times (w.r.t. movement onset) of electrodes from the lateral array were color-coded, with the propagation direction marked with the arrow (the length of the arrow represents the R^2 of the fit: **a**: R^2=0.390, **b**: R^2=0.210). Right: The amplification times (w.r.t. movement onset) of electrodes from the lateral array were represented as heights of the green dots in a 3D space where x and y axes represent electrode locations. Black grid represents planar fit.

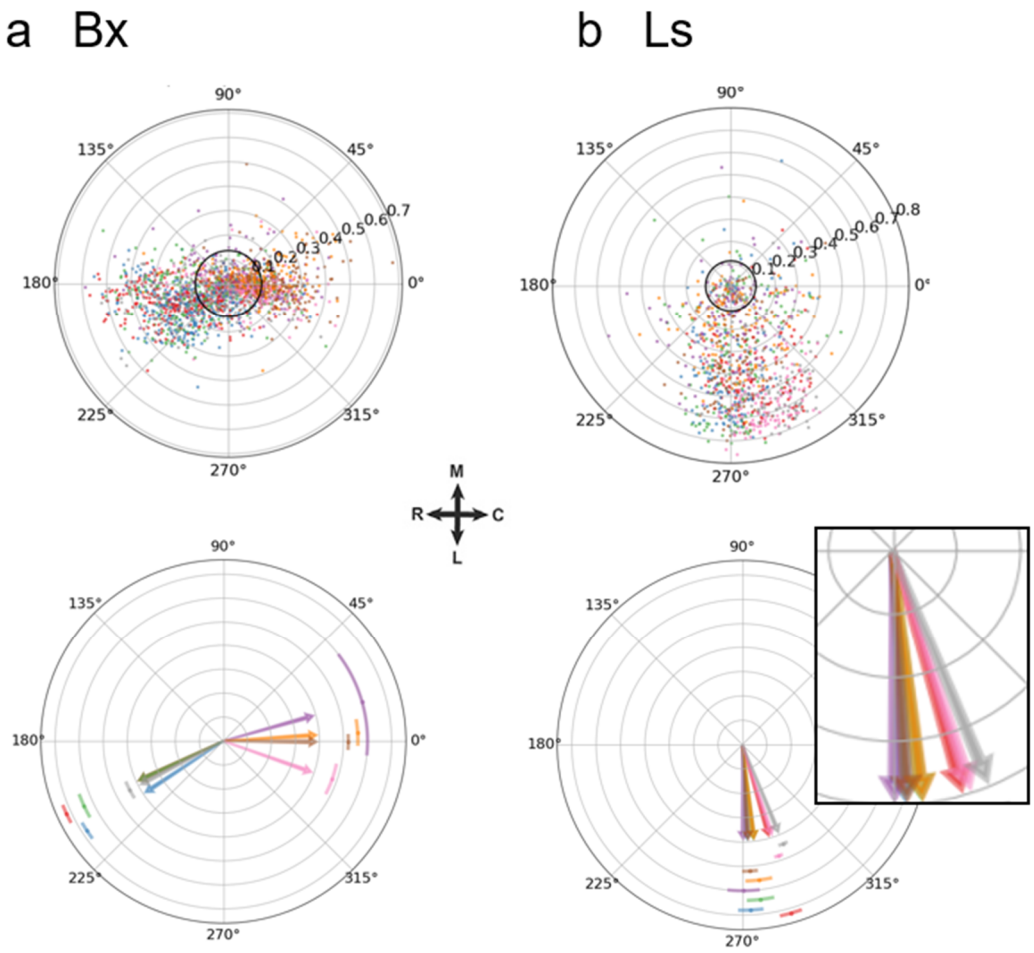

Figure 3.4 Summary of single-trial spatio-temporal propagation directions for the lateral arrays. **a** & **b** are for Monkey Bx and Ls respectively. Top: polar scatter plot of propagation directions. Each dot is a single trial color-coded by reach direction. Angle represents propagation direction, while radius represents the associated R^2. Black solid circle represents the threshold of significant R^2 values. Bottom: summary of propagation directions for significant trials for each reach direction. Angle of arrow represents the mean propagation direction, while the error bar represents the 68.27% confidence interval for the mean. The bottom summary plot in **b** was zoomed in to show details.

Table 3.1a 200-400Hz Propagation characteristics of trials with significant planar propagation on the lateral array for monkey Bx. sem is standard error of mean. r is length of the mean resultant vector of angles, which is a measure of concentration.

Reach target (deg)	Propagating direction (deg) (mean±sem) (r)	Propagating speed (m/s) (mean±sem) (median)	Sample size
0	205.0±4.2 (r=0.67)	0.065±0.004 (0.051)	162
45	213.4±2.8 (r=0.81)	0.061±0.003 (0.047)	220
90	205.0±2.7 (r=0.83)	0.052±0.003 (0.037)	212
135	207.7±4.2 (r=0.66)	0.059±0.003 (0.055)	170
180	340.6±7.2 (r=0.52)	0.088±0.005 (0.079)	104
225	359.6±2.9 (r=0.88)	0.098±0.003 (0.094)	162
270	3.7±5.0 (r=0.68)	0.100±0.004 (0.091)	111
315	15.7±20.8 (r=0.20)	0.094±0.006 (0.086)	94

Table 3.1b 200-400Hz Propagation characteristics of trials with significant planar propagation on the lateral array for monkey Ls. sem is standard error of mean. r is length of the mean resultant vector of angles, which is a measure of concentration.

Reach target (deg)	Propagating direction (deg) (mean±sem) (r)	Propagating speed (m/s) (mean±sem) (median)	Sample size
0	276.7±4.4 (r=0.74)	0.078±0.004 (0.072)	113
45	272.9±3.8 (r=0.81)	0.084±0.003 (0.081)	120
90	286.1±3.1 (r=0.88)	0.085±0.003 (0.082)	134
135	292.3±1.7 (r=0.95)	0.084±0.002 (0.081)	132
180	288.0±1.4 (r=0.97)	0.079±0.002 (0.078)	123
225	273.4±2.7 (r=0.91)	0.089±0.004 (0.085)	88
270	277.0±4.9 (r=0.71)	0.075±0.004 (0.068)	100
315	270.5±5.6 (r=0.67)	0.071±0.004 (0.067)	88

The formation of these two modes in the propagation characteristics can be explained by the biased kinematic trajectories generated by the monkeys due to training history. The monkeys were heavily trained on the blue and brown targets; thus Bx tended to generate initial trajectories for other adjacent reach targets that were clustered around the trajectories of the heavily trained targets. This was evident from the initial mean paths for each target (Fig. 3.5a, top panel inset) and the mean velocity angles for each target (Fig. 3.5a, top panel) suggesting the propagation properties were more closely linked to movement execution rather than movement goal. The relationship between mean launch angles and mean propagation directions for each target is shown more clearly in Fig. 3.5a, bottom panel. For monkey Ls, initial mean kinematic paths (Fig. 3.5b, top panel inset) and mean velocity angles (Fig. 3.5b, top panel) also roughly formed two groups (45, 90, 135 and 180 deg targets versus 225, 270, 315 and 0 deg targets), which corresponded to the grouping of the propagation directions with the exception of the 45 deg target (Fig. 3.5b, bottom panel).

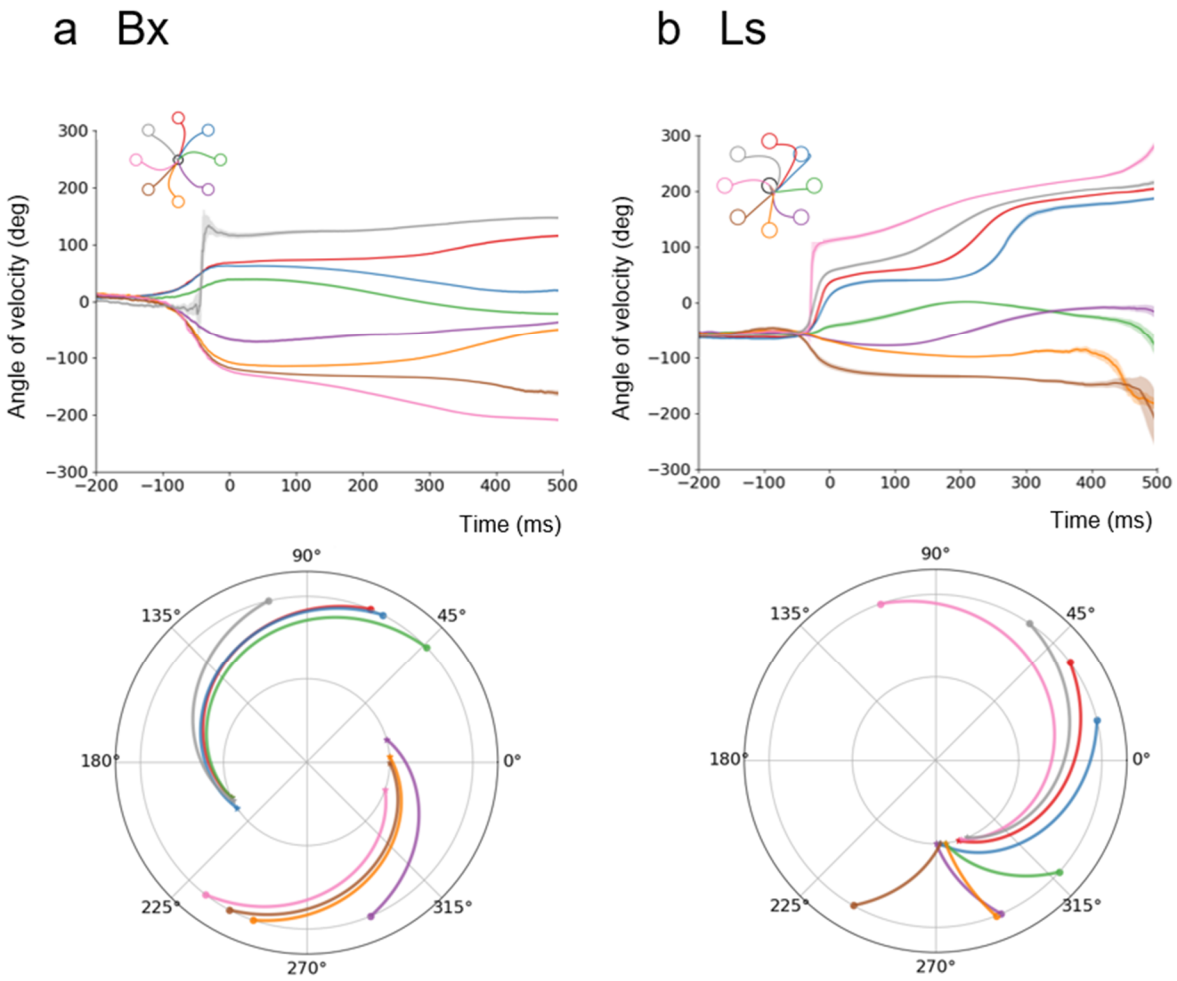

Figure 3.5 Clustering of hand kinematics and corresponding propagation directions for the lateral arrays. **a** & **b** are for Monkey Bx and Ls respectively. Top: mean angle of velocity traces across time (error shade represents the 68.27% confidence interval for the mean). The mean hand paths are shown in the inset. Colors represent different targets. Bottom: stars on the inner circle represent mean propagation directions for each reach target, while dots on the outer circle represent mean launch direction at movement onset (0 ms) for each reach target. The lines connecting the inner and outer dots were linearly interpolated for visualization purposes. Clusters of propagation directions correspond to clusters of kinematic launch directions for all targets in both monkeys, except for the blue direction in Ls (**b**).

For the medial arrays, although there was not an obvious correspondence between kinematics groupings and propagation characteristics (Fig. 3.6 a,b; Supplementary Fig. 3.S3), propagation directions were significantly different (or borderline significantly different) across target

directions ($p<0.001$ for Ls, $p=0.064$ for Bx, non-parametric test for common median for multiple groups of angles). The descriptive statistics for propagation characteristics can be found in Table 3.2a,b.

Although we examined planar propagation in medial and lateral arrays separately, the propagation characteristics of the lateral array and medial array were not isolated. The propagation speed in the medial array was correlated with the propagation speed in the lateral array for both monkeys (for Bx, Pearson correlation coefficient $r= 0.377$, $p<0.001$, $n=248$; for Ls, $r=0.473$, $p<0.001$, $n=415$, see Supplementary Fig. 3.S5, top panel). Also, the median amplification times in the medial array were correlated with the median amplification times in the lateral array for both monkeys (for Bx, Pearson correlation coefficient $r= 0.610$, $p<0.001$, $n=248$; for Ls, $r=0.838$, $p<0.001$, $n=415$, see Supplementary Fig. 3.S5, bottom panel). These results suggest that the propagating patterns we examined in isolated arrays are part of a more global pattern that extends across the upper limb area of M1.

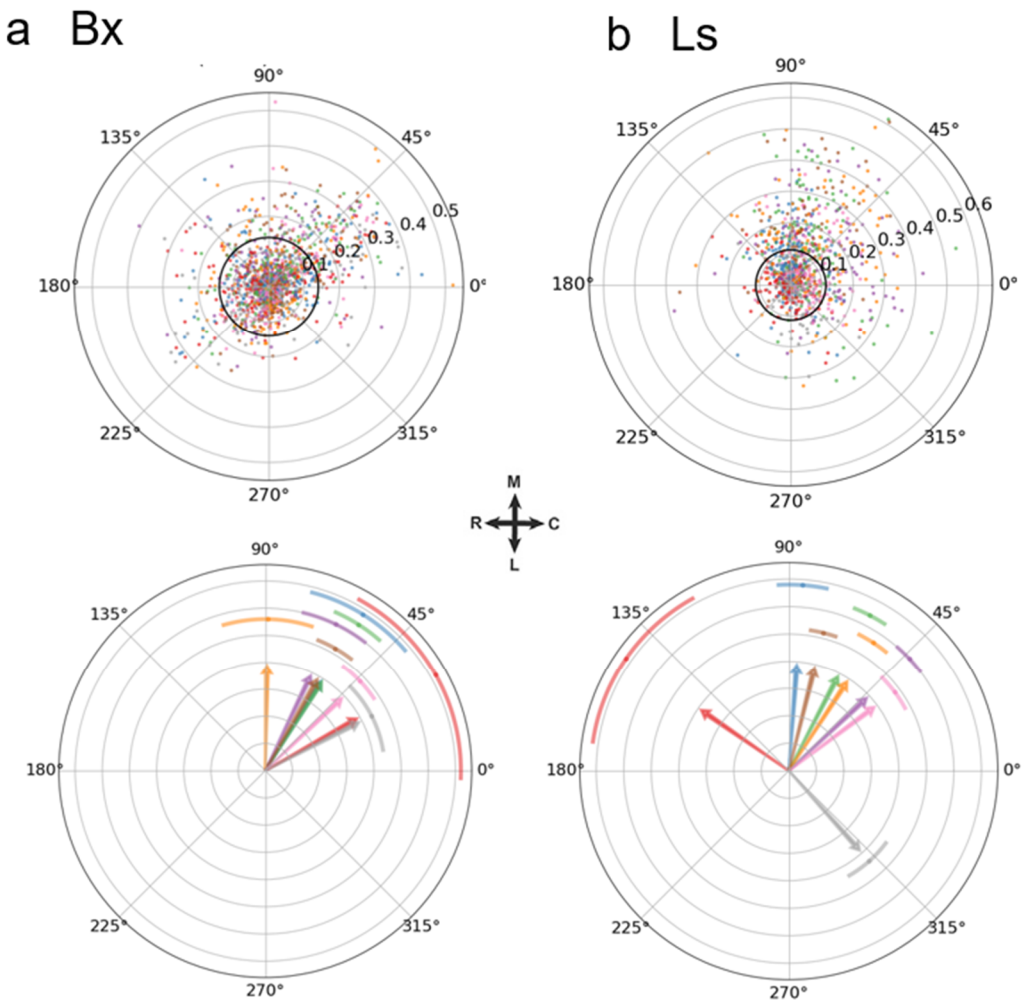

Figure 3.6 Summary of single-trial spatio-temporal propagation directions for the medial array. **a** & **b** are for Monkey Bx and Ls respectively. Top: polar scatter plot of propagation directions. Each dot is a single trial color-coded by reach direction. Angle represents propagation direction, while radius represents the associated R^2. Black solid circle represents the threshold of significant R^2 values. Bottom: summary of propagation directions for significant trials of each reach direction. Angle of arrow represents the mean propagation direction, while the error bar represents the 68.27% confidence interval for the mean.

Table 3.2a 200-400Hz Propagation characteristics of trials with significant planar propagation on the medial array for monkey Bx. sem is standard error of mean. r is length of the mean resultant vector of angles, which is a measure of concentration.

Reach target (deg)	Propagating direction (deg) (mean±sem) (r)	Propagating speed (m/s) (mean±sem) (median)	Sample size
0	57.6±8.5 (r=0.58)	0.229±0.021 (0.205)	56
45	58.1±17.2 (r=0.35)	0.199±0.022 (0.167)	44
90	29.6±31.7 (r=0.18)	0.170±0.018 (0.157)	54
135	27.3±17.3 (r=0.30)	0.187±0.015 (0.167)	61
180	43.4±9.7 (r=0.57)	0.223+0.017 (0.238)	45
225	60.3±7.6 (r=0.66)	0.210±0.017 (0.200)	52
270	89.1±16.8 (r=0.33)	0.186±0.018 (0.145)	51
315	64.4±12.0 (r=0.48)	0.198±0.020 (0.160)	45

Table 3.2b 200-400Hz Propagation characteristics of trials with significant planar propagation on the medial array for monkey Ls. sem is standard error of mean. r is length of the mean resultant vector of angles, which is a measure of concentration.

Reach target (deg)	Propagating direction (deg) (mean±sem) (r)	Propagating speed (m/s) (mean±sem) (median)	Sample size
0	62.5±5.4 (r=0.68)	0.133±0.006 (0.129)	92
45	85.7±7.4 (r=0.65)	0.156±0.008 (0.155)	57
90	145.3±26.2 (r=0.31)	0.148±0.012 (0.160)	25
135	311.6±11.6 (r=0.63)	0.167±0.013 (0.174)	25
180	36.7±8.3 (r=0.64)	0.182±0.010 (0.175)	47
225	76.0±5.1 (r=0.84)	0.133±0.008 (0.120)	60
270	56.9±5.9 (r=0.65)	0.111±0.007 (0.097)	89
315	43.1±5.7 (r=0.68)	0.099±0.006 (0.104)	87

Decoding kinematics with propagation patterns

Given the relationship between kinematics and propagation patterns observed above, we set out to test if that relationship could be useful in kinematic decoding. We used propagation parameters (propagation direction, propagation speed and planar regression goodness-of-fit, R^2) from both arrays to decode hand velocity at particular times with generalized linear models. We built a different model for each time point relative to movement onset, as there existed only one set of propagation parameters for each trial, and we sought to determine where in time over the trial these propagating parameters best predicted the hand velocity. For monkey Bx, the fraction of variance explained (or R^2) of this prediction (plotted in red) reached a peak average R^2 of 0.427 at 100ms, which was significantly better than shuffled control (p=0.001 for single-tailed Wilcoxon test, w=0.0; Fig. 3.7a, top panel); in other words, the spatiotemporal variables were most predictive of velocities at 100ms after movement onset for Bx. For monkey Ls, the fraction of variance explained of this prediction (in red) reached a peak average R^2 of 0.268 at 40ms, which was significantly better than shuffled control (p=0.001 for single-tailed Wilcoxon test, w=0.0; Fig. 3.7b)

Next, we looked at the contributions of each type of propagating parameter by using each separately to predict velocities. For Bx, models using only propagation direction reached performance levels nearly as good as the complete set of parameters, and R^2 also had some predictive power (Fig. 3.7a, bottom panel). For Ls, models using propagation direction parameters only and using R^2 only both had similar predictive power, though not as good as the complete set (Fig. 3.7b, bottom panel). For both monkeys, the propagation speed lacked predictive power when used alone. Those consistent prediction results across monkeys indicated that despite the different extents of spread in the propagation parameters, the spatial patterns

provided meaningful kinematic information regarding velocity. It might be argued that the propagation patterns were, in fact, predicting movement speed rather than velocity, and our prediction of velocity could be accounted for by a potential link between movement speed and velocity. However, in this task movement speed only weakly accounted for movement velocity (the composite R^2 using instantaneous speed to predict instantaneous velocity was 0.03 for Bx and 0.16 for Ls, which were much lower than the performance of velocity prediction using spatial variables for the majority of time points in Figure 3.7).

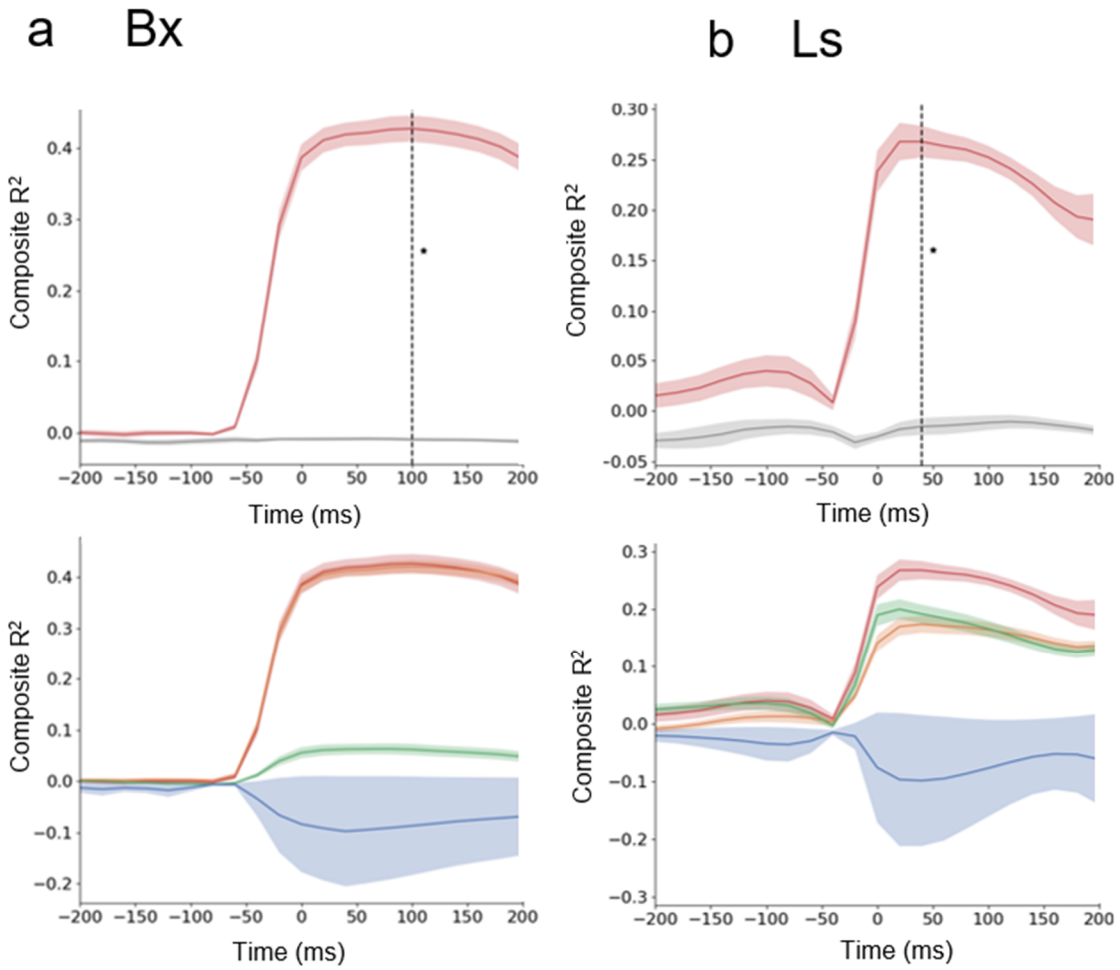

Figure 3.7 Propagation parameters can be used to decode hand velocities. **a** & **b** are for Monkey Bx and Ls respectively. Top: Prediction performance (composite R^2) for hand velocities at different time points w.r.t. movement onset using all propagation parameters (i.e. propagation direction, speed and planar fitness from both arrays), where a different model was built for each

(**Figure 3.7** continued) time point. Red traces represent actual performance and gray line represents performance from the trial-shuffled control. Error shade represents sem from 10 folds. Optimal time where velocity prediction achieves best results is marked with the dotted vertical line (100ms in Bx and 40ms in Ls). Star denotes that propagation parameters can predict kinematics significantly better than chance at the optimal time point from single-tailed Wilcoxon test. Bottom: breakdown of contributions from individual propagation parameters on hand velocity prediction. Red trace - all parameters as above; orange trace – propagation direction only; green trace – planar fitness only; blue – propagation speed only. For both monkeys, propagation direction and planar fitness were more useful than propagation speed when used alone to predict movement velocities. For Bx, the red and orange traces largely overlapped.

High-gamma band amplitude is known to carry rich kinematic information and has been used in online and offline motor output decoding (Flint et al., 2013; Flint, Ethier, et al., 2012; Flint, Lindberg, et al., 2012; Zhuang et al., 2010). Thus, we wanted to test whether characteristics of the spatio-temporal propagation patterns contain additional non-redundant kinematic information beyond the high-gamma amplitude envelopes themselves. For this purpose, we compared the performance of three types of models: a. an instantaneous envelope-amplitude-only model; b. a propagation-parameter-only model (including both first-order parameters and second-order interactions); c. instantaneous amplitude envelope + propagation parameter model. With these models, we then decoded hand velocity continuously throughout the trial. Thus, we had to determine the optimal lag between the continuous amplitude envelope and continuous hand velocity which occurred at -180 ms and -120 ms for Bx and Ls, respectively, indicating that envelope led the hand velocity as expected in M1 (Fig. 3.8a,b, top panels). At those optimal lags, the performances of the amplitude envelope + propagation parameter model were significantly better than the envelope-amplitude-only model ($p=0.001$ for single-tailed Wilcoxon test, $w=0.0$ for both monkeys). A trial-shuffling procedure also demonstrated a significant increase in decoding performance when including the propagation parameters to the amplitude envelopes (Fig. 3.8a,b, bottom panels). These results demonstrate that the spatio-temporal organization of

these high-gamma envelopes provide additional, non-redundant kinematic information beyond the envelope magnitudes alone.

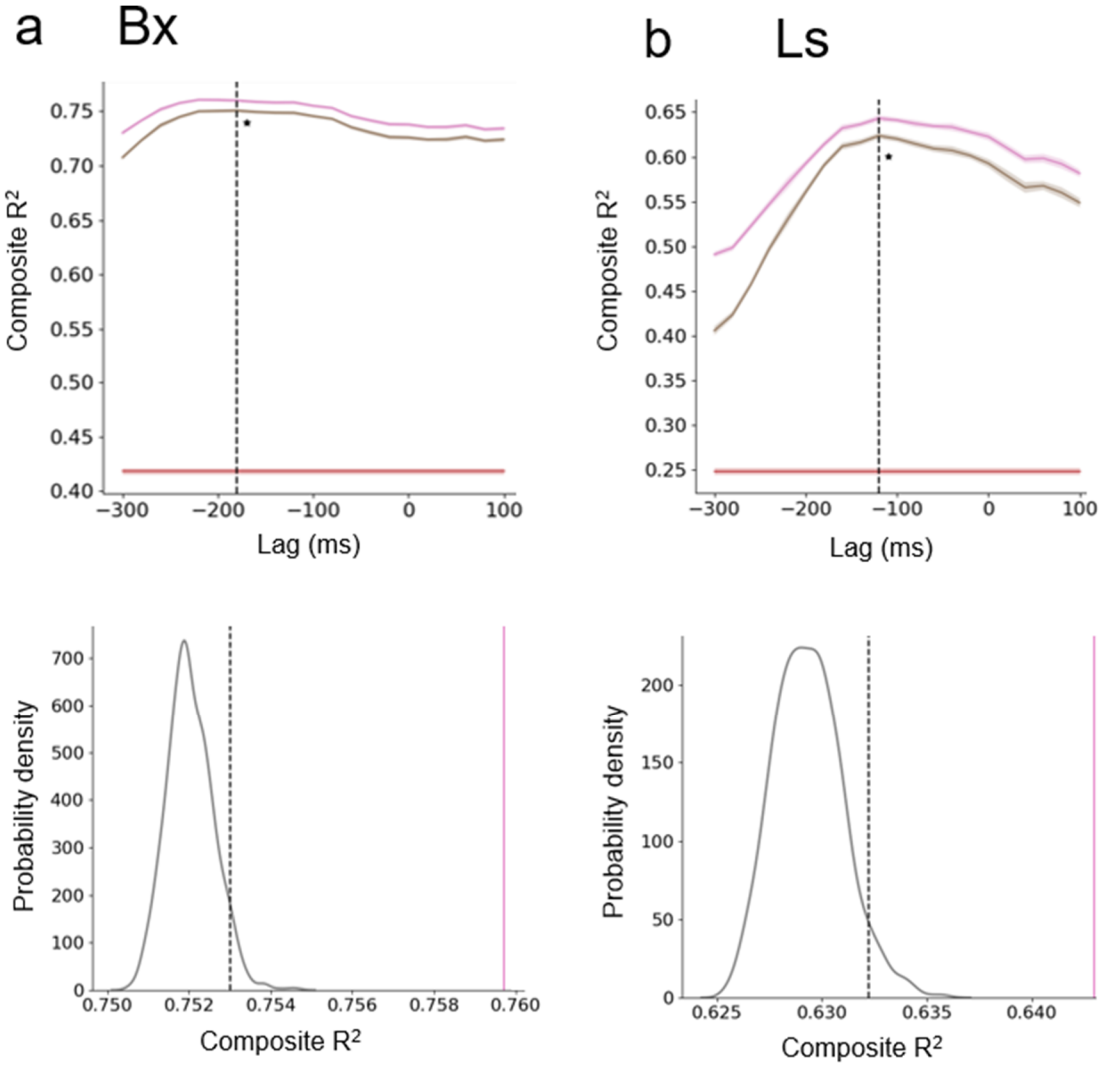

Figure 3.8 Propagation parameters provided additional decoding performance on top of amplitude envelopes. **a** & **b** are for Monkey Bx and Ls respectively. Propagation parameters here include not only 1st order parameters, but also 2nd order interactions terms. Top: prediction performance (composite R^2) for hand velocities at different lags from the instantaneous amplitude envelope (negative lags means neural signals precede hand velocity), where brown trace denotes using instantaneous envelopes only as predictors; red trace denotes using propagation parameters only (1st and 2nd orders) as predictors (performance was lag-independent as there was only one set of spatial variables for the whole trial); pink trace denotes using both instantaneous envelopes and propagation parameters as predictors. Error shade denotes sem from 10 folds. The time lag where the best mean envelope-amplitude-only performance was achieved was marked by the dotted vertical line (-180ms for Bx and -120ms for Ls). Star denotes that amplitude + propagation (pink) achieves significantly better prediction than amplitude-only

(**Figure 3.8** continued) (brown) at the best lag using a single-tailed Wilcoxon test. Lower: the improved performance from including the propagation parameters together with the amplitude envelopes could not be obtained by merely adding propagation parameters from a random trial. The gray distribution shows the decoding performances of random additions of propagation parameters from other trials together with the correct envelopes, with the top 5% threshold marked in dotted vertical black line. The solid pink vertical line denotes the real performance (i.e. addition of corresponding propagation parameters), which exceeds the dotted black line for both monkeys.

Movement-specific propagating patterns in MUA encode kinematics

Our choice of using the high-gamma LFP to analyze spatio-temporal patterning was motivated by the fact that it served as a useful proxy for MUA activity, and it was present on all electrodes to allow for adequate spatial coverage. In contrast, MUA activity was not consistently present on all electrodes. Moreover, some electrodes had sparse MUA activity (defined as average firing rate below 1Hz throughout movement even for the most modulated direction). This was particularly true for Bx where a quarter of electrodes had sparse MUA activity. Here we aimed to replicate our findings using MUA activity from Ls where only ~4% of electrodes had sparse MUA activity. For Ls, the mean median MUA amplification time was -55.3ms (31.6ms) for the lateral array and -15.4ms (43.3ms) for the medial array. These amplification times were later than the amplification times of the 200-400Hz high-gamma signal (-81.1ms (60.0ms) for the lateral array and -81.5ms (67.9ms) for the medial array), consistent with the cross-correlation lag between the two signals discussed above.

Next, we computed propagation patterns based on MUA for Ls. For the lateral array, 572 out of 1167 trials (53%) exhibited significant planar propagation patterns. For the medial array, 205 out of 1167 trials (18%) exhibited significant planar propagation patterns. These proportions of

significant propagations were substantially smaller compared to the corresponding proportions from 200-400Hz signal (86% and 46%). Propagation directions were significantly different across target directions ($p<0.001$ for both arrays in Ls, non-parametric test for common median for multiple groups of angles). Although propagation directions were similar to those using the high-gamma signal only for certain directions, the global distribution of propagation directions was largely similar when considering all trials. The speed of MUA propagation was in general lower than high-gamma propagation (especially for the medial array). For those trials exceeding the R^2 threshold, planar propagation fits were generally worse than those for the high-gamma signal, which might have led to lower propagation speed (See Supplementary Figure 3.S7 and Supplementary Table 3.S1 for more details on the propagation patterns).

Kinematic decoding using MUA propagation parameters was also evident (see Supplementary Figure 3.S8) and, in fact, was moderately better than when using their high-gamma counterparts. The highest kinematic prediction performance using first-order propagation parameters of MUA was a composite R^2 of 0.332 instead of 0.268 from the high-gamma signal (a 24% increase in performance). Decoding performance using both MUA firing rates and MUA propagation variables (1^{st} and 2^{nd} order) was slightly better than using the high-gamma amplitude envelopes and high-gamma propagation variables (1^{st} and 2^{nd} order), with a ~0.06 increase in composite R^2 (a 9% increase in performance).

Discussion

Despite extensive evidence of traveling waves and, more generally, propagating spatio-temporal patterns in cortex (Balasubramanian et al., 2020; Besserve et al., 2015; Gabriel & Eckhorn, 2003; Lubenov & Siapas, 2009; Muller & Destexhe, 2012; Nauhaus et al., 2012; Patel et al., 2012; Sato et al., 2012; Wu et al., 2008; Xu et al., 2007; Zanos et al., 2015), experimental evidence for their role in carrying behaviorally-relevant information is rare, and, when present, often reflects general behavioral state. At the macroscopic scale, forward-directed waves in the 8-13 Hz band of human EEG have been documented to propagate from occipital to frontal lobes during visual processing while backward-directed waves from frontal to occipital lobes occur in the absence of sensory input (Pang et al., 2020). Forward- and backward-directed waves measured in the 2-13 Hz band of human ECoG recordings tend to correspond to the encoding and retrieval stages of episodic memory tasks, respectively (Mohan et al., 2022). However, in these cases, wave direction does not provide detailed information about the visual stimulus identity or memory content.

At the mesoscopic scale, traveling phase waves mediated by beta oscillations in M1 propagate in a stereotyped fashion along a rostro-caudal axis in non-human primates (Rubino et al., 2006; Takahashi et al., 2015). While it was found that information about reach target was larger in sequential activity of pairs of neurons whose spatial orientation on the cortical sheet matched the traveling wave axis, characteristics of the waves including their direction and speed did not vary with behavior (Takahashi et al., 2015). Moreover, traveling waves mediated by beta oscillations in area V4 have been shown to be triggered by saccadic eye movements (Zanos et al., 2015). While the wave amplitude correlated with the saccade direction, the propagation direction remained invariant propagating from foveal to peripheral locations. Spontaneous traveling waves in area MT of marmosets have been shown to improve target detection by temporally aligning a

highly excitable state in the receptive field of the target but again wave propagation direction did not carry information about perceptual sensitivity (Davis et al., 2020).

In this study, we demonstrate, for the first time to our knowledge, a link between neural propagation direction and specifics of movement behavior. We showed that the propagation direction of high-gamma band recruitment timing carries kinematic information by demonstrating that hand launch velocity (and potentially later movement kinematics, see supplementary material including Supplementary Figure 3.S6) can be decoded on a trial-by-trial basis. Moreover, the fact that spatially organized propagation patterns provided additional predictive power in decoding kinematics beyond the high-gamma LFP amplitudes (or MUA firing rate) themselves may have implications for improving brain-machine interfaces (BMIs). Previous offline decoding studies have used high frequency LFP amplitudes to decode movements and have found decoding performance of kinematics and muscle activity was nearly equal to that of spikes (Flint, Ethier, et al., 2012; Flint, Lindberg, et al., 2012; Zhuang et al., 2010). However, these studies did not consider the spatio-temporal organization of high frequency LFP amplitude modulation.

More importantly, these findings have fundamental scientific implications as they suggest that there is a dynamic spatial organization of activity on the motor cortical sheet that may serve a functional role in executing movements that goes beyond the static view of somatotopy (Park et al., 2004; Penfield & Boldrey, 1937). Given that high-gamma LFP amplitude serves as a close proxy to multi-unit activity, these results imply that there is an orderly recruitment sequence of activity across the motor cortical sheet that informs details of the upcoming movement. In fact, we were able to replicate the same analyses with multi-unit activity in monkey Ls, and found that MUA propagation patterns contained movement-specific spatio-temporal organization that was

useful for kinematic decoding. In contrast, propagation direction of beta frequency amplitude attenuation provides no information about upcoming movement kinematics (see Supplementary Fig. 3.S4) and only signals movement initiation in a condition-independent manner (Balasubramanian et al., 2020, 2022; Kaufman et al., 2016); we also examined an alternative definition of high-gamma using a lower 100-200Hz frequency band, where we also found propagation patterns, but they provided only limited kinematic information (see supplementary material).

In order to extract and characterize single-trial propagation patterns, a number of pre-processing steps were required. First of all, despite the obvious amplitude envelope amplification on trial-averaged data, high-gamma amplitude amplification was too noisy to reliably extract amplification signatures on a single-trial basis. To robustly denoise single trials given the constraint of limited trial counts, we used a combination of principal components analysis (PCA) followed by an autoencoder. A pure autoencoder denoising method was prone to getting stuck at local minima resulting in poorer reconstruction, while a pure-PCA denoising method was poor at rejecting severe noise due to lack of a non-linearity transformation. In the whole denoising process, no spatial information was provided, thus eliminating the possibility of introducing any spatial smoothness. Secondly, to identify the amplification time on each channel, we chose the time point where the first derivative of the cleaned envelope reached its maximum thus avoiding the use of an arbitrary threshold on the envelope. Thirdly, after excluding outlier channels (see Methods), we fit a plane to the amplification times in order to compute its propagation properties. The use of a planar fit served as a local approximation to make propagations more tractable, but we acknowledge the possibility that this local pattern could be part of a larger pattern that might be more complex (e.g., rotary or spiral). In fact, when looking at both the

lateral and medial arrays simultaneously, the speeds of the two propagating patterns were significantly correlated in both monkeys with the propagation speed of the medial array being approximately twice of that of the lateral array (see Supplementary Fig. 3.S5). Moreover, the amplification times across both arrays were significantly correlated in both monkeys. Although beyond the scope of the current study, this suggests the potential of more complex propagation patterns at a larger spatial scale.

The exact propagation directions differed across the two monkeys particularly on the lateral arrays. This is likely due to the differences in the exact placement of the arrays and individual cerebral organization. Intra-cortical microstimulation (ICMS) of sites on the lateral array for Bx evoked either hand or wrist movements, while the majority of sites on the lateral array for Ls evoked hand movements (see Supplementary Fig. 3.S1). As explained above, the patterns we observed from single arrays were most likely part of larger spatio-temporal patterns; thus, propagating directions would naturally be different if the spatial windows were slightly shifted, even if the larger patterns were generally similar. Another possible reason for the difference across the two monkeys is the fact that electrode lengths in Bx were 1.5 mm whereas in Ls they were 1.0 mm. The longer electrodes may have reached the upper portion of layer 5 whereas the shorter electrodes were likely in layers 2/3. Nevertheless, despite the individual differences in propagation patterns, these patterns both provided meaningful kinematic decoding in both monkeys.

In future studies, we plan on extending this investigation to more complex movements with multiple submovements such as sequential movements that are either planned or unplanned. We hypothesize that there should be multiple distinct propagation patterns in the high-gamma band associated with each submovement, especially in the unplanned case.

Data availability

The data supporting the findings of this study is available at

https://doi.org/10.5061/dryad.j6q573nj1

Code availability

The code used for analyses in this study is available at https://github.com/hatsopoulos-lab/macaque-spatio_temporal_pattern

Acknowledgments

This study is supported by NIH R01 NS111982. We thank Carrie Anne Balcer for animal training, and Caleb Sponheim, Kazutaka Takahashi, Paul Aparicio and all other members of the lab for helpful discussions.

References

Balasubramanian, K., Arce-McShane, F. I., Dekleva, B. M., Collinger, J. L., & Hatsopoulos, N. G. (2022). Propagating motor cortical patterns of excitability are ubiquitous across human and non-human primate movement initiation. https://papers.ssrn.com/sol3/papers.cfm?abstract_id=4108216

Balasubramanian, K., Papadourakis, V., Liang, W., Takahashi, K., Best, M. D., Suminski, A. J., & Hatsopoulos, N. G. (2020). Propagating Motor Cortical Dynamics Facilitate Movement Initiation. *Neuron*, *106*(3), 526-536.e4. https://doi.org/10.1016/j.neuron.2020.02.011

Berens, P. (2009). CircStat : A MATLAB Toolbox for Circular Statistics . *Journal of Statistical Software*, *31*(10). https://doi.org/10.18637/jss.v031.i10

Besserve, M., Lowe, S. C., Logothetis, N. K., Schölkopf, B., & Panzeri, S. (2015). Shifts of

Gamma Phase across Primary Visual Cortical Sites Reflect Dynamic Stimulus-Modulated Information Transfer. *PLoS Biology*, *13*(9), 1–29. https://doi.org/10.1371/journal.pbio.1002257

Davis, Z. W., Muller, L., Martinez-Trujillo, J., Sejnowski, T., & Reynolds, J. H. (2020). Spontaneous travelling cortical waves gate perception in behaving primates. *Nature*, *587*(7834), 432–436. https://doi.org/10.1038/s41586-020-2802-y

Fisher, N. I., Lewis, T., & Embleton, B. J. J. (1993). *Statistical analysis of spherical data*. Cambridge university press.

Flint, R. D., Ethier, C., Oby, E. R., Miller, L. E., & Slutzky, M. W. (2012). Local field potentials allow accurate decoding of muscle activity. *Journal of Neurophysiology*, *108*(1), 18–24. https://doi.org/10.1152/jn.00832.2011

Flint, R. D., Lindberg, E. W., Jordan, L. R., Miller, L. E., & Slutzky, M. W. (2012). Accurate decoding of reaching movements from field potentials in the absence of spikes. *Journal of Neural Engineering*, *9*(4). https://doi.org/10.1088/1741-2560/9/4/046006

Flint, R. D., Wright, Z. A., Scheid, M. R., & Slutzky, M. W. (2013). Long term, stable brain machine interface performance using local field potentials and multiunit spikes. *Journal of Neural Engineering*, *10*(5). https://doi.org/10.1088/1741-2560/10/5/056005

Gabriel, A., & Eckhorn, R. (2003). A multi-channel correlation method detects traveling γ-waves in monkey visual cortex. *Journal of Neuroscience Methods*, *131*(1–2), 171–184. https://doi.org/10.1016/j.jneumeth.2003.08.008

Jammalamadaka, S. R., & Sengupta, A. (2001). *Topics in circular statistics* (Vol. 5). world scientific.

Kaufman, M. T., Seely, J. S., Sussillo, D., Ryu, S. I., Shenoy, K. V., & Churchland, M. M. (2016). The largest response component in the motor cortex reflects movement timing but not movement type. *ENeuro*, *3*(4). https://doi.org/10.1523/ENEURO.0085-16.2016

Lubenov, E. V., & Siapas, A. G. (2009). Hippocampal theta oscillations are travelling waves. *Nature*, *459*(7246), 534–539. https://doi.org/10.1038/nature08010

Mohan, U. R., Zhang, H., & Jacobs, J. (2022). The direction and timing of theta and alpha traveling waves modulate human memory processing. *BioRxiv*, 2022.02.07.479466. https://www.biorxiv.org/content/10.1101/2022.02.07.479466v1%0Ahttps://www.biorxiv.org/content/10.1101/2022.02.07.479466v1.abstract

Muller, L., & Destexhe, A. (2012). Propagating waves in thalamus, cortex and the thalamocortical system: Experiments and models. *Journal of Physiology Paris*, *106*(5–6), 222–238. https://doi.org/10.1016/j.jphysparis.2012.06.005

Nauhaus, I., Busse, L., Ringach, D. L., & Carandini, M. (2012). Robustness of traveling waves in ongoing activity of visual cortex. *Journal of Neuroscience*, *32*(9), 3088–3094. https://doi.org/10.1523/JNEUROSCI.5827-11.2012

Pang, Z., Alamia, A., & Vanrullen, R. (2020). Turning the stimulus on and off changes the direction of α traveling waves. *ENeuro*, *7*(6), 1–11. https://doi.org/10.1523/ENEURO.0218-

20.2020

Park, M. C., Belhaj-Saïf, A., & Cheney, P. D. (2004). Properties of primary motor cortex output to forelimb muscles in rhesus macaques. *Journal of Neurophysiology*, *92*(5), 2968–2984.

Patel, J., Fujisawa, S., Berényi, A., Royer, S., & Buzsáki, G. (2012). Traveling Theta Waves along the Entire Septotemporal Axis of the Hippocampus. *Neuron*, *75*(3), 410–417. https://doi.org/10.1016/j.neuron.2012.07.015

Penfield, W., & Boldrey, E. (1937). Somatic Motor and Sensory Representation in Man. *Brain*, 389–443.

Rifai, S., Vincent, P., Muller, X., Glorot, X., & Bengio, Y. (2011). Contractive auto-encoders: Explicit invariance during feature extraction. *Proceedings of the 28th International Conference on Machine Learning, ICML 2011*, *1*, 833–840.

Rubino, D., Robbins, K. A., & Hatsopoulos, N. G. (2006). Propagating waves mediate information transfer in the motor cortex. *Nature Neuroscience*, *9*(12), 1549–1557. https://doi.org/10.1038/nn1802

Sato, T. K., Nauhaus, I., & Carandini, M. (2012). Traveling Waves in Visual Cortex. *Neuron*, *75*(2), 218–229. https://doi.org/10.1016/j.neuron.2012.06.029

Takahashi, K., Kim, S., Coleman, T. P., Brown, K. A., Suminski, A. J., Best, M. D., & Hatsopoulos, N. G. (2015). Large-scale spatiotemporal spike patterning consistent with wave propagation in motor cortex. *Nature Communications*, *6*(May), 1–11. https://doi.org/10.1038/ncomms8169

Wu, J. Y., Huang, X., & Zhang, C. (2008). Propagating waves of activity in the neocortex: What they are, what they do. *Neuroscientist*, *14*(5), 487–502. https://doi.org/10.1177/1073858408317066

Xu, W., Huang, X., Takagaki, K., & Wu, J. young. (2007). Compression and Reflection of Visually Evoked Cortical Waves. *Neuron*, *55*(1), 119–129. https://doi.org/10.1016/j.neuron.2007.06.016

Zanos, T. P., Mineault, P. J., Nasiotis, K. T., Guitton, D., & Pack, C. C. (2015). A Sensorimotor Role for Traveling Waves in Primate Visual Cortex. *Neuron*, *85*(3), 615–627. https://doi.org/10.1016/j.neuron.2014.12.043

Zar, J. H. (2009). *Biostatistical Analysis. Fifth edn, 960*. Pearson.

Zhuang, J., Truccolo, W., Vargas-Irwin, C., & Donoghue, J. P. (2010). Decoding 3-D reach and grasp kinematics from high-frequency local field potentials in primate primary motor cortex. *IEEE Transactions on Biomedical Engineering*, *57*(7), 1774–1784. https://doi.org/10.1109/TBME.2010.2047015

Supplementary material

Propagation patterns encoded for not only the launch angle but also later kinematics

In the main text, we established that propagation patterns encoded for launch velocities. Here we probe whether the patterns also contained information regarding later parts of the trajectory, controlling for the autocorrelation in the velocities.

We used launch velocities (x velocity and y velocity at movement onset) to predict velocities at other time points (from 20 to 400ms in steps of 20 ms, one model for each time point), and compared its performance with using both launch velocities and high-gamma spatial variables to predict velocities. For monkey Bx, there was no significant difference in the performance including or excluding high-gamma spatial variables on top of launch velocities, because he had been making relatively straight trajectories and there was a strong autocorrelation in the velocities (Supplementary Figure 3.S6a, top panel). Thus for Bx, we could not rule out the fact that all the prediction for later velocities came from prediction of launch velocities. However, for monkey Ls, there were two targets where he made bent trajectories (90° and 135° targets, mean trajectories shown in the inset of Supplementary Figure 3.S6b, top panel), in which cases high-gamma spatial variables provided significant additional prediction power on top of launch velocities, precisely at those time when he was transitioning from moving forward to moving to the left in the curved trajectory (several time points from 80~180ms; stars indicate that propagation parameters can predict kinematics significantly better than using launch velocities at the time points from single-tailed Wilcoxon test, Bonferroni-corrected for multiple comparisons). This improved prediction was primarily driven by the propagation direction (orange trace in

Supplementary Figure 3.S6b, bottom panel) and planar fitness (green trace in Supplementary Figure 3.S6b, bottom panel).

Granted that this center-out task was not the best to detect such encoding for later parts of the trajectory, we still found that high-gamma spatial patterns possessed such information at least when velocities were less autocorrelated, in the form of planned curved trajectories. We plan to study this phenomenon more thoroughly with other movement tasks which included multiple submovements or ongoing corrections that are either planned or unplanned, to establish this concretely.

Analyses of 100-200Hz high-gamma band

For Bx, the mean (standard deviation) of the median amplification times was -111.9ms (68.8ms) for the lateral array and -82.5ms (92.5ms) for the medial array. For Ls, the mean median amplification time was -82.8ms (53.2ms) for the lateral array and -60.1ms (71.0ms) for the medial array. These amplification times were similar to results from 200-400Hz within variation.

Next, we computed the propagation patterns based on 100-200Hz signal. For the lateral arrays, 1269 out of 2435 trials (52%) exhibited significant planar propagation patterns for Bx and 687 out of 1079 trials (64%) for Ls exhibited significant planar propagation patterns. For the medial arrays, 599 out of 2435 trials (25%) exhibited significant planar propagation patterns for Bx, and for Ls 449 out of 1079 trials (42%). These ratios of significant propagations were largely similar to the results from 200-400Hz. Propagation directions were significantly different across target directions in both arrays for both monkeys (lateral array: $p=0.003$ for Bx, $p<0.001$ for Ls; medial array: $p=0.017$ for Bx, $p<0.001$ for Ls, non-parametric test for common median for multiple

groups of angles). Nevertheless, there was often larger variance in propagation direction for a given movement direction (sometimes bimodal), resulting in lower mean vector lengths (i.e. lower r values in Supplementary Table 3.S2 and 3.S3).

Like the 200-400Hz results, the propagation in the two arrays were related. The propagation speed in the medial array was correlated with the propagation speed in the lateral array for both monkeys (for Bx, Pearson correlation coefficient r= 0.682, $p<0.001$, n=402; for Ls, r=0.581, $p<0.001$, n=277). Also, the median amplification time in the medial array was correlated with the median amplification time in the lateral array for both monkeys (for Bx, Pearson correlation coefficient r= 0.783, $p<0.001$, n=401; for Ls, r=0.775, $p<0.001$, n=277).

All the kinematic decoding conclusions qualitatively held as well, though all the decoding performances were weaker than using their 200-400Hz counterparts. The highest kinematic prediction performance using first order spatial parameters of 100-200Hz was a composite R^2 of 0.127 instead of 0.427 from 200-400Hz for Bx (a 70% drop of performance) and a composite R^2 of 0.151 instead of 0.268 from 200-400Hz for Ls (a 44% drop of performance). The prediction performance using both envelope amplitudes and spatial variables (1st and 2nd order) were also lower than using 200-400Hz, with a ~0.38 decrease in composite R^2 for Bx (a 50% drop of performance) and a ~0.15 decrease for Ls (a 23% drop of performance).

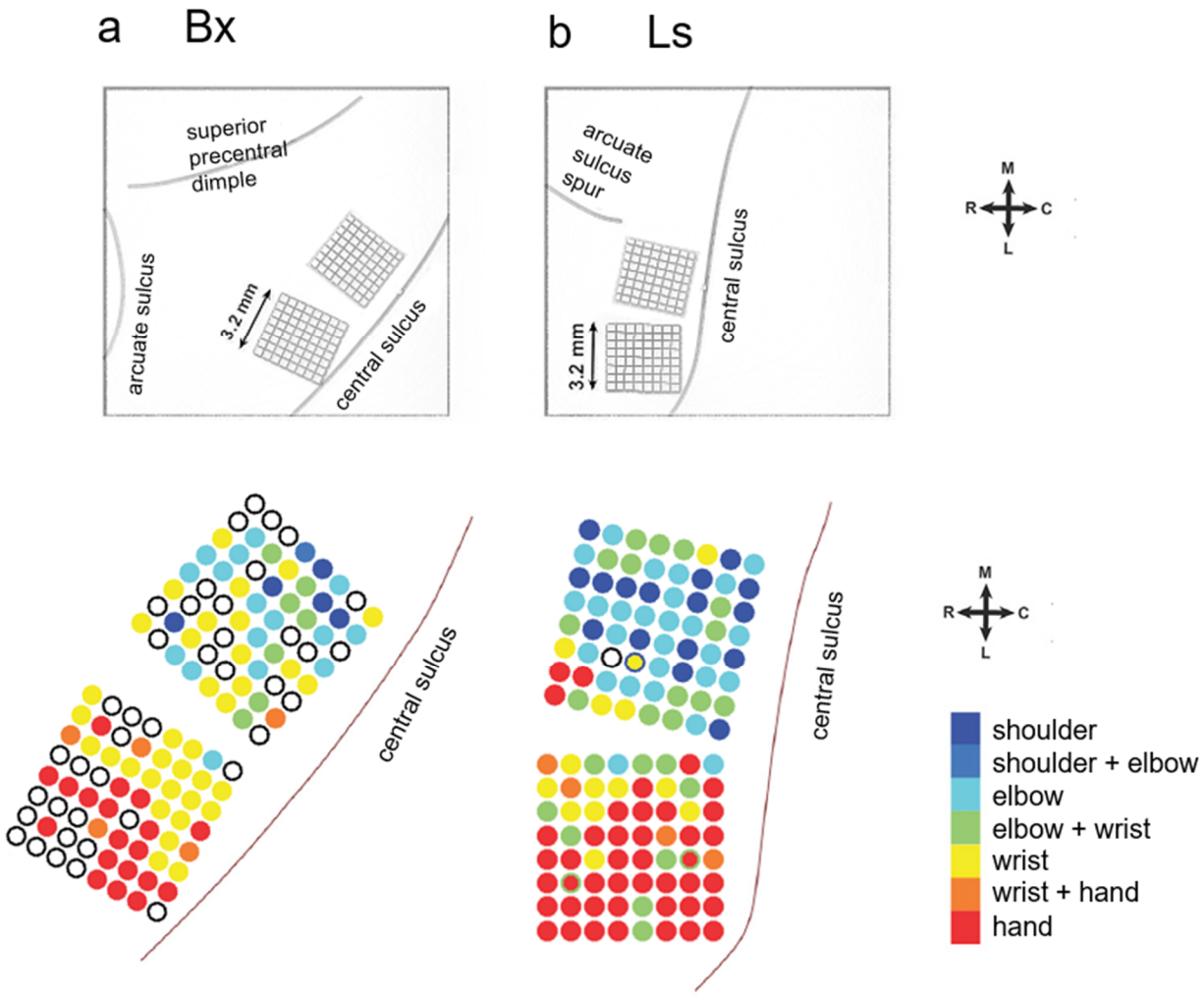

Fig. 3.S1 Array implant locations and somatotopy. **a** & **b** are for Monkey Bx and Ls respectively. Top: two 8-by-8 Utah arrays were implanted in the primary motor cortex for each monkey. Bottom: somatotopic maps were obtained through suprathreshold intra-cortical microstimulation. Colors represent twitches on different body parts evoked during stimulation at the site, where mixed representations were illustrated as single intermediate colors (in cases of twitches of adjacent body parts) or different inner + outer colors (in cases of activations of non-adjacent body parts). Empty circles denote absence of observed twitches.

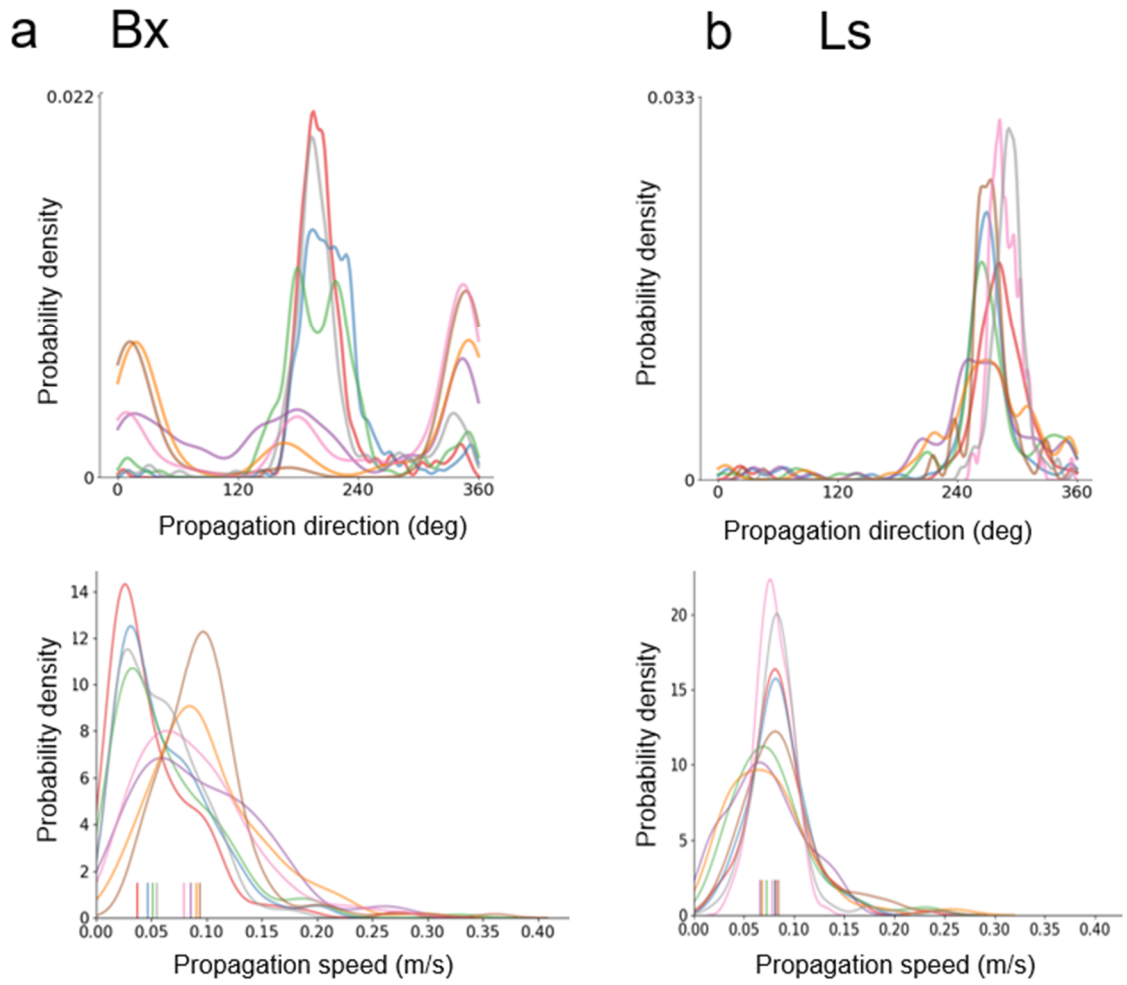

Fig. 3.S2 Distributions of propagation properties for the lateral arrays. **a** & **b** are for monkeys Bx and Ls respectively. Colors represent target directions. Top: distribution of propagation directions for each target direction. Bottom: distribution of propagation speeds for each target direction (ticks represent median propagation speeds for individual target directions).

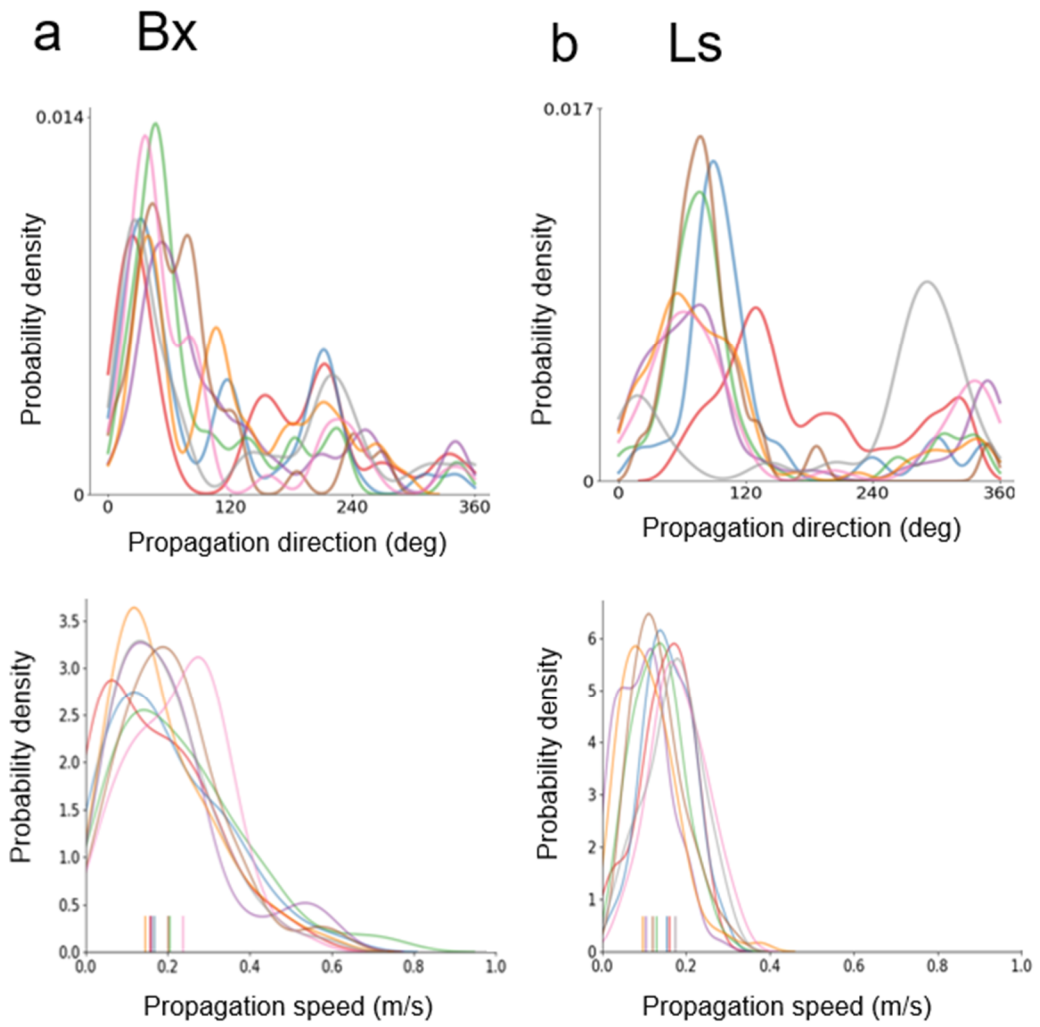

Fig. 3.S3 Distributions of propagation properties for the medial arrays. **a** & **b** are for monkeys Bx and Ls respectively. Colors represent target directions. Top: distribution of propagation directions for each target direction. Bottom: distribution of propagation speeds for each target direction (ticks represent median propagation speeds for individual target directions).

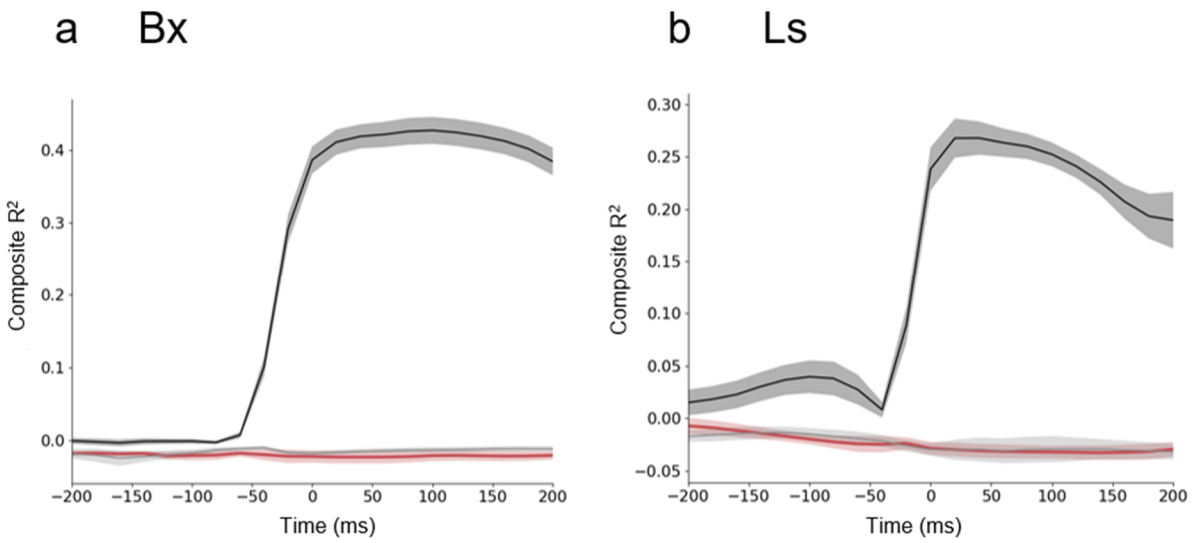

Fig. 3.S4 Propagation parameters in the beta band cannot predict movement velocities. **a** & **b** are for monkeys Bx and Ls respectively. Red traces denote prediction performance (composite R^2) for hand velocities at different time points (w.r.t. movement onset) using all propagation parameters (i.e. propagation direction, speed and planar fitness from both arrays) in the beta band, which is indistinguishable from the gray traces denoting the performance from the trial-shuffled control. For reference, black traces represent the decoding performance from high-gamma band from **Fig. 3.7**. Error shade denotes sem from 10 folds.

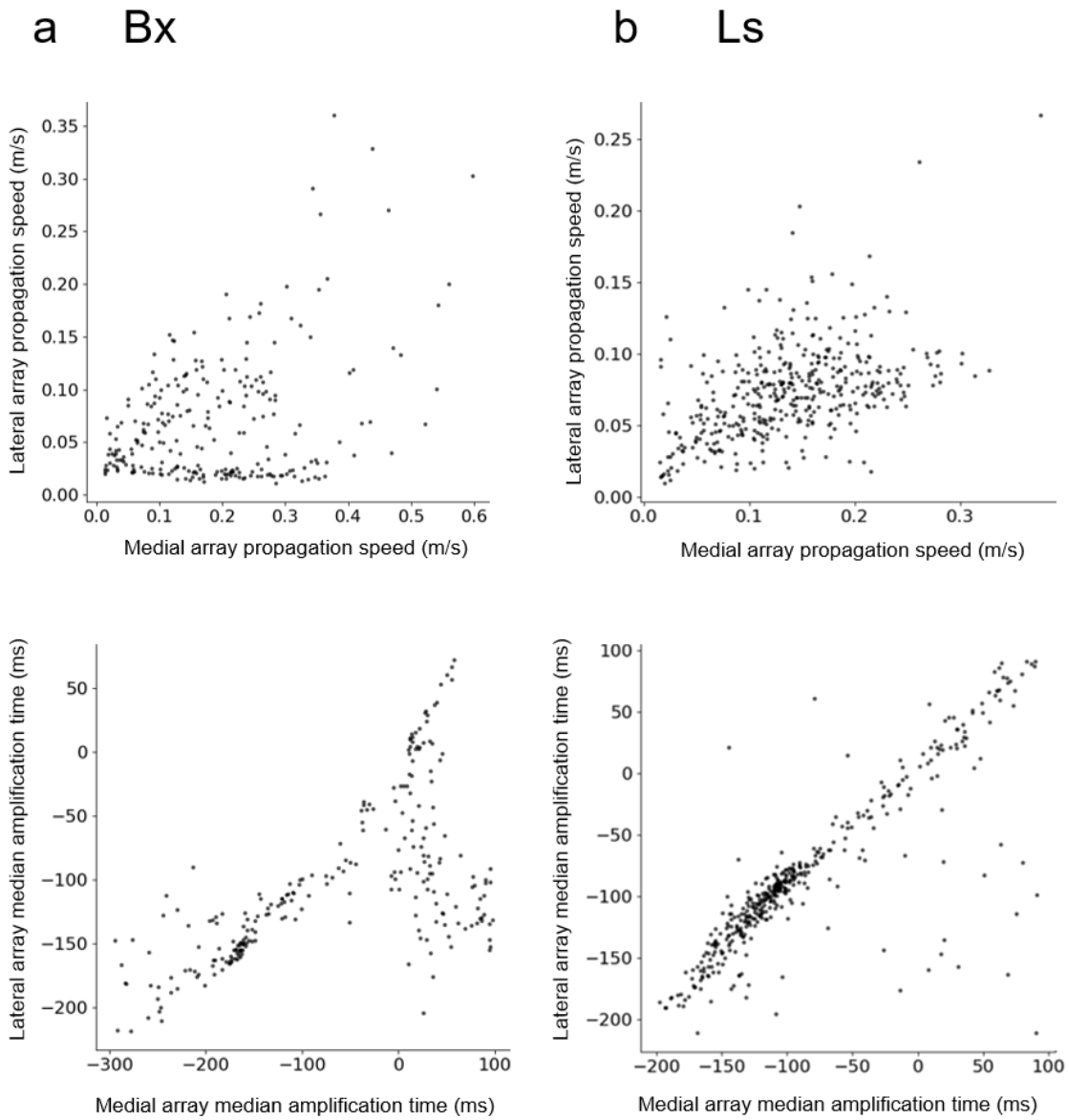

Fig. 3.S5 Propagation patterns of the medial and lateral array were correlated on a trial-by-trial basis. **a** & **b** are for monkeys Bx and Ls respectively. Top: Scatter plots of the propagation speeds from the medial and lateral arrays for trials with significant propagation on both arrays, showing positive correlation between the two arrays (for Bx, $r=0.377$, $p<0.001$, $n=248$; for Ls, $r=0.473$, $p<0.001$, $n=415$; Pearson correlations test). Bottom: Scatter plots of the median amplification times (w.r.t. movement onset) from the medial and lateral arrays for trials with significant propagation on both arrays, showing positive correlation between the two arrays (for Bx, $r=0.610$, $p<0.001$, $n=248$; for Ls, $r=0.838$, $p<0.001$, $n=415$; Pearson correlations test).

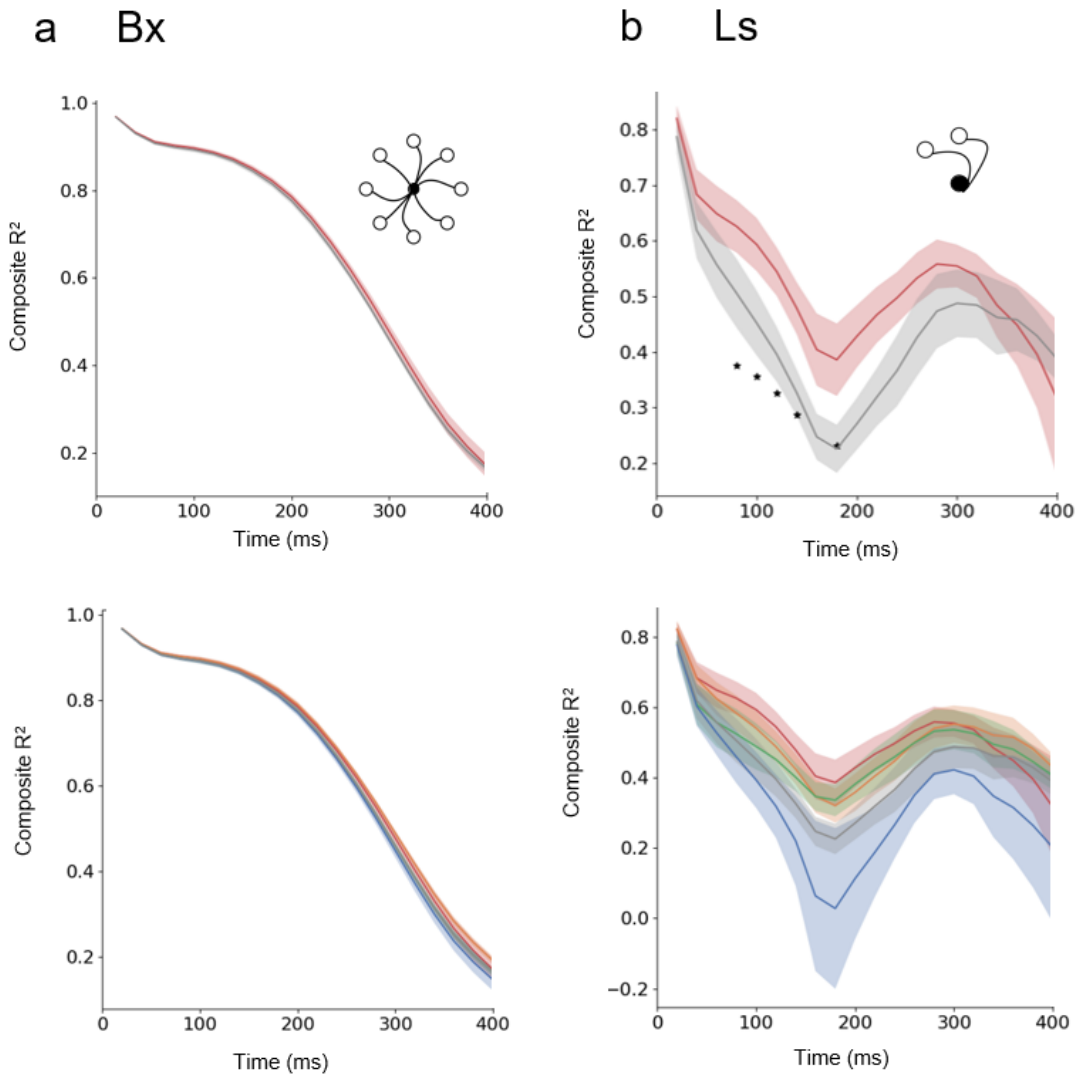

Fig. 3.S6 Propagation parameters encoded for updating of hand velocities when trajectories were bent. a & b are for Monkey Bx and Ls respectively. Top: Prediction performance (composite R^2) for hand velocities at different time points (w.r.t. movement onset) using all propagation parameters (i.e. propagation direction, speed and planar fitness from both arrays) and launch velocities (red traces); gray line represents prediction performance (composite R^2) for hand velocities at different time points using launch velocities only. Error shade represents sem from 10 folds. Stars indicate that propagation parameters can predict kinematics significantly better than using launch velocities at the time points from single-tailed Wilcoxon test, Bonferroni-corrected for multiple comparisons. Insets show the mean trajectories to targets that were used in this prediction. For Bx, trials from all targets were used; for Ls, only trials from the two targets with bent trajectories were used. Bottom: breakdown of contributions from individual propagation parameters on hand velocity prediction. Red trace - all parameters as above, including launch velocities; orange trace – propagation direction and launch velocity; green trace – planar fitness and launch velocity; blue – propagation speed and launch velocity; gray — launch velocity only. For Ls, the added performance from high-gamma spatial variables primarily came from propagation direction and planar fitness.

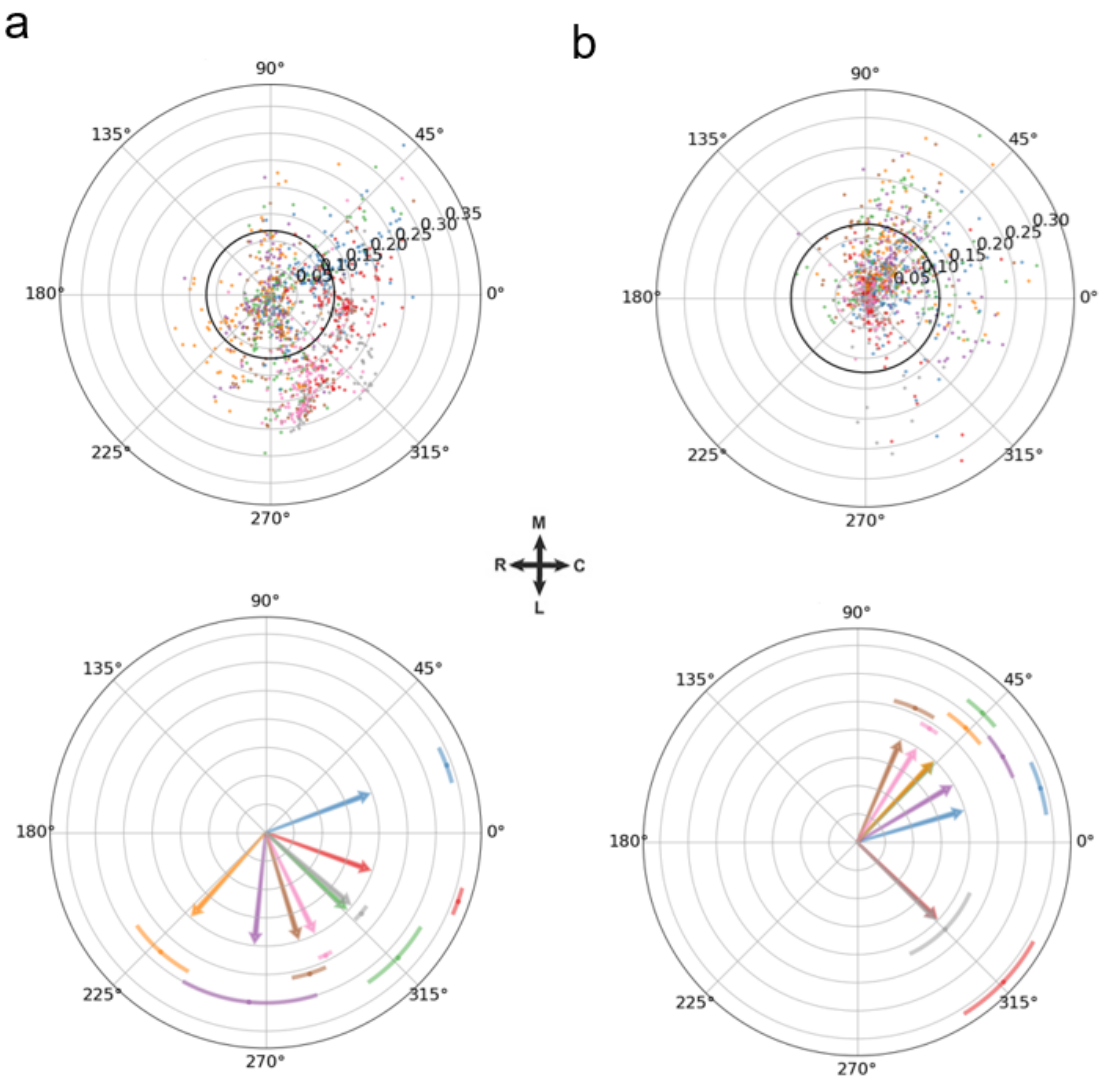

Fig. 3.S7 Summary of MUA-based single-trial spatio-temporal propagation directions for Ls. **a** & **b** are for the lateral array and the medial array respectively. Top: polar scatter plot of propagation directions. Each dot is a single trial color-coded by reach direction. Angle represents propagation direction, while radius represents the associated R^2. Black solid circle represents the threshold of significant R^2 values. Bottom: summary of propagation directions for significant trials for each reach direction. Angle of arrow represents the mean propagation direction, while the error bar represents the 68.27% confidence interval for the mean.

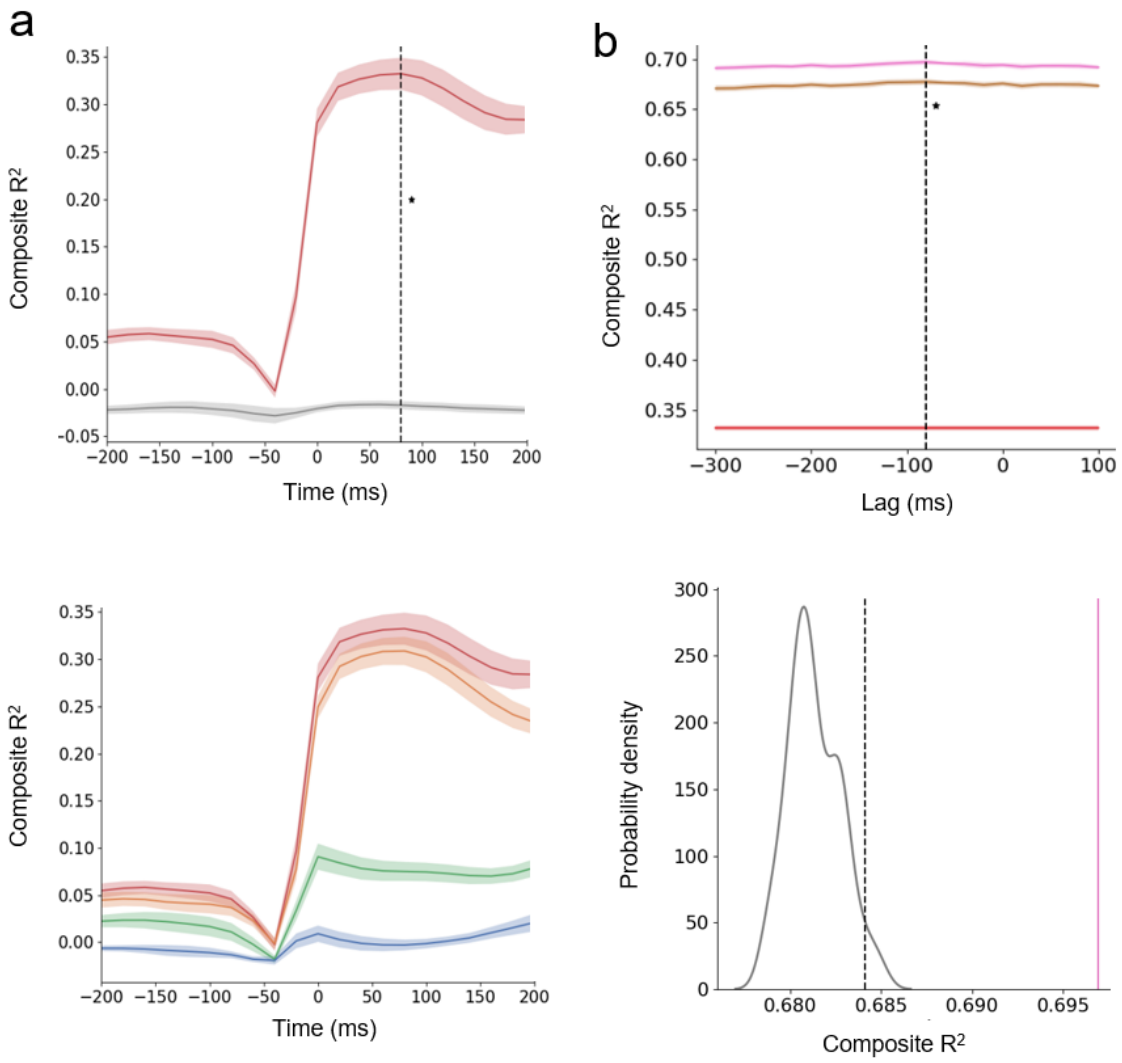

Fig. 3.S8 MUA propagation parameters in Ls can be used to decode hand velocities and provided additional decoding performance on top of firing rates. **a**. Top: Prediction performance (composite R^2) for hand velocities at different time points (w.r.t. movement onset) using all MUA propagation parameters (i.e. propagation direction, speed and planar fitness from both arrays, all were 1st order). Red traces represent actual performance and gray line represents performance from the trial-shuffled control. Error shade represents sem from 10 folds. Optimal time where velocity prediction achieves best results is marked with the dotted vertical line (80ms w.r.t. movement onset). Star denotes that propagation parameters could predict kinematics significantly better than chance at the optimal time point from single-tailed Wilcoxon test. **a**. Bottom: breakdown of contributions from individual MUA propagation parameters on hand velocity prediction. Red trace - all parameters as above; orange trace – propagation direction only; green trace – planar fitness only; blue – propagation speed only. MUA propagation direction was more useful than propagation speed when used alone to predict movement velocities. **b.** Top: prediction performance (composite R^2) for hand velocities at different lags from the instantaneous MUA firing rate (negative lags means neural signals precede hand velocity), where brown trace denotes using instantaneous MUA firing rate only as predictors; red trace denotes using MUA propagation parameters only (1st and 2nd orders) as predictors

(**Figure 3.S8** continued) (performance was lag-independent as there was only one set of spatial variables for the whole trial); pink trace denotes using both instantaneous MUA firing rate and MUA propagation parameters as predictors. Propagation parameters here include not only 1st order parameters, but also 2nd order interactions terms. Error shade denotes sem from 10 folds. The time lag where the best mean envelope-amplitude-only performance was achieved was marked by the dotted vertical line (-80ms). Star denotes that MUA firing rate + propagation (pink) achieves significantly better prediction than firing rate-only (brown) at the best lag using a single-tailed Wilcoxon test. **b.** Lower: the improved performance from including the MUA propagation parameters together with the MUA firing rate could not be obtained by merely adding propagation parameters from a random trial. The gray distribution shows the decoding performances of random additions of MUA propagation parameters from other trials together with the correct envelopes, with the top 5% threshold marked in dotted vertical black line. The solid pink vertical line denotes the real performance (i.e. addition of corresponding propagation parameters), which exceeds the dotted black line.

Supplementary Table 3.S1a MUA Propagation characteristics of trials with significant planar propagation on the lateral array for monkey Ls. sem is standard error of mean. r is length of the mean resultant vector of angles, which is a measure of concentration.

Reach target (deg)	Propagating direction (deg) (mean±sem) (r)	Propagating speed (m/s) (mean±sem) (median)	Sample size
0	316.6±11.6 (r=0.48)	0.057±0.009 (0.038)	48
45	20.5±5.0 (r=0.84)	0.045±0.005 (0.035)	60
90	340.3±3.4 (r=0.86)	0.056±0.004 (0.048)	119
135	319.8±3.3 (r=0.87)	0.052±0.002 (0.049)	123
180	295.9±2.3 (r=0.92)	0.052±0.002 (0.048)	117
225	287.2±6.1 (r=0.78)	0.050±0.006 (0.043)	51
270	228.2±11.9 (r=0.51)	0.049±0.008 (0.028)	39
315	264.2±5.6 (r=0.45)	0.044±0.009 (0.035)	15

Supplementary Table 3.S1b MUA Propagation characteristics of trials with significant planar propagation on the medial array for monkey Ls. sem is standard error of mean. r is length of the mean resultant vector of angles, which is a measure of concentration.

Reach target (deg)	Propagating direction (deg) (mean±sem) (r)	Propagating speed (m/s) (mean±sem) (median)	Sample size
0	46.1±5.5 (r=0.84)	0.035±0.002 (0.030)	50
45	16.4±7.6 (r=0.79)	0.045±0.004 (0.039)	31
90	316.2±13.8 (r=0.82)	0.047±0.010 (0.057)	9
135	315.5.6±19.4 (r=0.55)	0.046±0.009 (0.025)	13
180	57.7±3.4 (r=0.99)	0.069±0.005 (0.072)	5
225	66.8±7.8 (r=0.89)	0.059±0.018 (0.030)	21
270	46.7±7.4 (r=0.79)	0.036±0.003 (0.031)	33
315	30.7±7.5 (r=0.71)	0.046±0.003 (0.042)	43

Supplementary Table 3.S2a 100-200Hz Propagation characteristics of trials with significant planar propagation on the lateral array for monkey Bx. sem is standard error of mean. r is length of the mean resultant vector of angles, which is a measure of concentration.

Reach target (deg)	Propagating direction (deg) (mean±sem) (r)	Propagating speed (m/s) (mean±sem) (median)	Sample size
0	185.8±9.0 (r=0.36)	0.119±0.010 (0.084)	147
45	224.8±6.5 (r=0.40)	0.111±0.006 (0.088)	226
90	221.9±5.1 (r=0.50)	0.114±0.006 (0.092)	217
135	219.8±6.4 (r=0.44)	0.121±0.008 (0.094)	187
180	267.8±20.9 (r=0.18)	0.137±0.012 (0.109)	119
225	5.4±23.1 (r=0.16)	0.152±0.010 (0.128)	124
270	58.1±20.0 (r=0.18)	0.135±0.010 (0.106)	130
315	90.3±22.1 (r=0.17)	0.139±0.011 (0.105)	119

Supplementary Table 3.S2b 100-200Hz Propagation characteristics of trials with significant planar propagation on the lateral array for monkey Ls. sem is standard error of mean. r is length of the mean resultant vector of angles, which is a measure of concentration.

Reach target (deg)	Propagating direction (deg) (mean±sem) (r)	Propagating speed (m/s) (mean±sem) (median)	Sample size
0	291.4±7.9 (r=0.54)	0.080±0.006 (0.064)	76
45	273.6±5.3 (r=0.70)	0.102±0.007 (0.084)	92
90	294.4±4.1 (r=0.79)	0.098±0.004 (0.093)	105
135	291.6±3.3 (r=0.88)	0.093±0.005 (0.085)	118
180	287.1±2.5 (r=0.91)	0.088±0.004 (0.081)	111
225	290.0±7.6 (r=0.61)	0.090±0.006 (0.085)	64
270	306.4±13.7 (r=0.36)	0.095±0.010 (0.075)	66
315	319.9±13.2 (r=0.40)	0.094±0.009 (0.081)	55

Supplementary Table 3.S3a 100-200Hz Propagation characteristics of trials with significant planar propagation on the medial array for monkey Bx. sem is standard error of mean. r is length of the mean resultant vector of angles, which is a measure of concentration.

Reach target (deg)	Propagating direction (deg) (mean±sem) (r)	Propagating speed (m/s) (mean±sem) (median)	Sample size
0	231.3±11.9 (r=0.37)	0.327±0.025 (0.264)	82
45	No reliable mean or confidence interval due to low concentration (r=0.01)	0.343±0.024 (0.298)	80
90	185.2±42.3 (r=0.12)	0.333±0.022 (0.313)	77
135	No reliable mean or confidence interval due to low concentration (r=0.05)	0.320±0.024 (0.287)	63
180	259.1±16.9 (r=0.28)	0.313±0.023(0.290)	70
225	208.0±14.7 (r=0.27)	0.360±0.024 (0.299)	103
270	206.3±17.0 (r=0.32)	0.290±0.023 (0.251)	53
315	257.6±12.3 (r=0.38)	0.322±0.024 (0.239)	71

Supplementary Table 3.S3b 100-200Hz Propagation characteristics of trials with significant planar propagation on the medial array for monkey Ls. sem is standard error of mean. r is length of the mean resultant vector of angles, which is a measure of concentration.

Reach target (deg)	Propagating direction (deg) (mean±sem) (r)	Propagating speed (m/s) (mean±sem) (median)	Sample size
0	45.2±11.3 (r=0.43)	0.115±0.012 (0.097)	61
45	56.2±31.7 (r=0.19)	0.128±0.012 (0.123)	49
90	231.0±14.5 (r=0.35)	0.138±0.013 (0.120)	61
135	No reliable mean or confidence interval due to low concentration (r=0.07)	0.159±0.013 (0.139)	60
180	76.5±9.2 (r=0.68)	0.142±0.010 (0.138)	33
225	67.8±9.9 (r=0.53)	0.124±0.010 (0.116)	53
270	19.3±8.1 (r=0.58)	0.112±0.010 (0.100)	61
315	22.3±7.7 (r=0.57)	0.119±0.011 (0.107)	71

IV. DISCUSSION

In this dissertation, I provided two pieces of evidence to challenge the static view of motor representation in the primary motor cortex. Namely, the mapping strength between local neural activity and motor output (in the form of muscle activity) is constantly changing. In addition, I have shown that neural activity unfolds over space and time whose spatio-temporal properties encode motor output.

Those results contribute to a congruent narrative, regardless of the direction of mapping being considered. On the one hand, we can consider the mapping from motor output to neural activity: in the information dynamics story (Chapter 2), one muscle was preferentially encoded by different cortical locations at different time points; while in the spatio-temporal neural code story (Chapter 3), to execute a coherent reach movement, neural activity swept over the cortical sheet, involving many sites. On the other hand, we can also consider the mapping from neural activity to motor output: in the information dynamics story (Chapter 2), neural activity at one cortical site encodes activities from multiple muscles, with preferential encoding for different muscles at different times; while in the spatio-temporal neural code story (Chapter 3), one cortical region is involved in the execution of reaches in multiple movement directions, being most active for different movement directions at different times. Together, they support the dynamic view of motor representation in M1.

Notably, in addition to time, space on the cortical sheet is an important subject of interest in both stories. In contrast to most motor cortical encoding studies which ignore space, we explicitly factor in cortical space as a crucial independent variable in defining the patterns (Chapter 3), and constantly tie back to cortical space when exploring the dynamic representation (Chapter 2). As a result, not only does space provide the passive substrate where neural activity resides, it also gets

to interact with time to allow for characterization of a richer repertoire of neural activity (Chapter 3) and relationship between neural activity and motor output (Chapter 2). Inclusion of space also allows for a better comparison between the somatotopy-based static view and the dynamic view.

Reconciling the static and dynamic view of motor representation

How can we reconcile the dynamic view with the traditional static view of motor representation? Wu, Huang and Zhang (2008) had an interesting discussion on a similar issue, comparing functional maps and waves obtained with voltage-sensitive dyes mostly in the context of sensory cortex. Inspired by that, I will present analogous arguments in the context of motor cortex, with additional considerations.

First of all, static and dynamic motor representations were obtained in different experimental contexts, using different methods. Traditional somatotopic maps are generally obtained with supra-threshold micro-stimulation while the subject is at rest, while dynamic motor representations in this dissertation were obtained during active movement without electrical perturbations. Relatively natural movement scenarios (as opposed to resting state) seem to facilitate the discovery of multiplexed/dynamic motor representations. For example, with electrical stimulation of low current (15 μA) and low frequency (15Hz) on M1 during motor task, Park et al. (2001, 2004) found EMG-based motor maps with finer-scale structures that were more overlapping than those using traditional high-current and high-frequency stimulation paradigms during rest. This setup should have allowed them to discover dynamic maps, if not for their heavily trial-averaged processing (to be expounded later in this section).

Furthermore, in the process of obtaining a map, a more stringent 'threshold' was used in the case of static maps, while such a threshold was often more relaxed in the case of dynamic maps. For example, to obtain traditional somatotopic maps, procedures are usually carefully designed to find the lowest current that could elicit the smallest muscle twitch, in an attempt to isolate the co-activated effectors as much as possible. In contrast, a much more relaxed threshold was set in the spatio-temporal code story (Chapter 3), where the derivative of the smoothed denoised high-gamma amplitude envelope only had to exceed the baseline mean fluctuation by 2 standard deviations for a site to be considered in the spatio-temporal pattern, resulting in a large pool of sites involved in each pattern. Similarly for the information dynamics story (Chapter 2), although we did pick a 'muscle winner' for each site at different time windows for visualization purposes, mutual information post-analyses remained quantitative for the most part. In other words, although many sites were responsible for encoding a certain muscle to various degrees (by standards of significantly non-zero mutual information), stimulating each of those sites at minimal currents might not have been enough to elicit twitches in that exact muscle in the traditional somatotopic mapping paradigm. On the other hand, for analyses where we did pick the 'muscle winner' in the information dynamics story, the information-based somatotopic gradient was largely similar to the somatotopic gradient in ICMS-based static map.

Additionally, static representations were usually obtained through robust single instances (for suprathreshold electrical stimulations) or trial-averages (for neuronal tuning preferences), while dynamic representations were usually obtained with full account of trial-to-trial variability. In the information dynamics story (Chapter 2), although at first glance it appears that no single-trial differentiations have been considered, mutual information by nature is based on the entropy (which can be understood as variabilities or uncertainties), both within and between trials in our

formulation; furthermore, we considered different reach directions and different time windows separately in the computation of mutual information. In the spatio-temporal code story (Chapter 3), substantial efforts were made to extract single-trial patterns in the high-gamma band and MUA; in other spatio-temporal pattern studies, such as patterns in beta amplitude envelopes and in beta phase waves, single-trial variabilities were considered as well (Balasubramanian et al., 2020; Rubino et al., 2006; Takahashi et al., 2011). In an effort to explain the differences between propagating patterns and functional maps, it is believed by some that trial-averages triggered by a stimulus will emphasize common input to the area, while removing spontaneous dynamical components within the area of interest itself that might not be related to the stimulus (Arieli et al., 1996; Xu et al., 2007). In my opinion, this argument can be revised and strengthened in that those spontaneous dynamical components removed by averaging could just as well be related to the stimulus/movement on some population level, which were removed erroneously through trial-averaging on an individual level or not at the correct population level. As a result, only when single trial variability is carefully preserved and examined would potentially different spatio-temporal neural patterns and dynamic neural-muscle relationships manifest. Trial-averages would mask dynamical processes that changes from time to time and from trial to trial, giving a static illusion.

Mechanisms and benefits of dynamic spatial representations

How did a dynamic motor representation scheme come into existence? Although the complete mechanisms have not been unresolved, both natural developmental processes and interactions with physical surroundings should play important roles.

Natural developmental processes give rise to the limb layout and a pre-wired over-connected brain. Even if neurons at this stage are only randomly and weakly selective, as body starts to actively interact with the physical surroundings, neuronal connections are trimmed to be more efficient with lowered threshold for eliciting movements. Through neural plasticity, movement representations are gradually formed on the cortical sheet that are roughly spatially separable (Eyre et al., 2000; Singleton et al., 2021). Given constraints in the limb structure, and regularities in physical surroundings, a movement repertoire is formed with species-similar natural statistics. This repertoire interacts with the cortical motor representation layout, constantly remolding and adjusting each other throughout lifetime (in the same spirit as in Aflalo & Graziano, 2006). Until now, the story seems similar with the formation of a traditional static representation. Importantly, however, several factors contributed to this representation being dynamic rather than static.

First of all, movement repertoires are usually consisting of sequences of different movement motifs involving multiple joints/limbs unfolding over time. Thus, natural statistics of movement repertoire would naturally be time- and situation-dependent. Corresponding to the varying natural statistics, to efficiently execute motor repertoire, cortical organization would naturally adapt to a representation scheme that unfolds over time, with built-in sensitivity to different situations. Situation sensitivity could be achieved with selections among multiplexed neural representations.

From another perspective, it is known that distributed population representations (loosely defined here, in contrast to single-cell representations) increase the robustness and capacity of neural codes (Abbott et al., 1996). Traditionally, the distributive property was taken to refer to different neurons, analogous to space. Here, dynamic codes that unfold over time like temporal patterns additionally utilize time in the distributive property, extending the code length, further serving to

increase encoding capacity and robustness. Thus, it is not surprising that brain utilizes a code distributed over both space and time.

Then, what is a natural way to construct a code that is distributed both in space and time? Bear in mind that the quantities and strengths of neural connections on the cortical sheet are generally distance-dependent and sometimes also spatially anisotropic. In this context, electrical and chemical signals naturally transmit to nearby regions to different extents with various distance-dependent delays. Thus, it is energy- and time-efficient to utilize the natural space and time delays on the cortical sheet to build the distributive code in space and time. With further interactions with physical surroundings under neural plasticity, the rough spatio-temporal code will be further refined and strengthened.

More concretely, how might the spatio-temporal patterns as we saw in Chapter 3 come into place? Wu et al. (2008) noted that (1) cortical propagation patterns in visual, auditory and barrel cortex usually initiate from locations of thalamic afferents and then propagate to surrounding areas (Song et al., 2006; Xu et al., 2007), e.g. in the form of a ring pattern; and (2) ring-type patterns can split into two wave fronts, and the two wave fronts could form spiral waves when colliding at particular timing and angle (Huang et al., 2004). With a rough layout of muscle selectivity on the cortical sheet, as well as a movement execution plan that unfolds over time, it is not hard to imagine that one or more selective motor cortical areas might be activated not too far apart in time, either for the planning or execution of the movement. From there, one or more propagation patterns could originate from those selective cortical areas. Given limited brain real estate, these patterns could easily collide into each other, forming complex patterns such as spiral waves. In fact, in Chapter 3, we saw that the speeds of propagation in the two arrays examined were related to each other with a ratio of 2, which could be indicative of spiral waves. If this

hypothesis holds, the array with larger speed (medial array in our case, representing the proximal limb), could sit closer to the spiral singularity.

Future work

This dissertation opened up some new avenues into the exploration of dynamic motor representation in M1 and reaffirmed its value compared with the traditional static view. In the future, it will be fruitful to extend current work in the following directions: (1) more thoroughly characterize the propagation patterns; (2) study the formation mechanism and adaptation of dynamic representation during motor learning or consolidation; and (3) probe the casual role of the propagation patterns in shaping behaviors.

Thorough characterization of propagation patterns

Since our work was the first documentation, to our knowledge, of propagation patterns encoding for fine behavioral details, more thorough characterizations are needed.

For example, in light of the likely presence of a larger pattern, we should record using bigger cortical coverage (encompassing more of M1 or even including premotor areas) and fit patterns with a bigger pool of patterns including ring and spiral patterns (Townsend & Gong, 2018). This way, the exact initiation regions, as well as potential pattern interactions and transformations would be more clearly revealed.

Additionally, we could study multi-stage movements where more than one set of propagation patterns are likely present, where we can observe the correspondence between kinematics and spatio-temporal patterns as a sequence of movements unfolds.

Related to this, are spatio-temporal patterns purely an execution signal, a planning signal, or a combination of both? The fact that we saw the initial propagation pattern encoding for later trajectories beyond the initial launch stage indicated that it might be more than an execution signal. To test this, we can compare the spatio-temporal patterns in several variants of a task, where the first variant includes mid-stage roadblocks forcing a shift in movement direction, a second variant where two pre-defined targets are presented tracing a similar curved trajectory that the subject knows before movement initiation they will have to cross, and a third variant where one where two pre-defined targets tracing a straight trajectory were presented before during preparation.

Lastly, since we currently only extract a pattern during the initial strong amplification of high-gamma signal, we arrived at only one propagation pattern per movement, limiting our ability to track continuous movements. Ideally, we would want to be able find another definition of spatio-temporal patterning which is more instantaneous and resolved on a fine time scale. From an applied perspective, those spatial patterns with higher temporal resolution would likely increase the prediction power for kinematics, thus holding more potential for robust chronic brain-machine interfaces. From a scientific perspective, they will enable us to compare more directly with instantaneous unit activity to arrive at potential mechanisms. We can even use the same modification of spatial pattern definition on single-unit activity, to probe previously unobserved spatial organizations of neuronal ‘tuning’ on a single-trial basis.

Formation and active adaptation of dynamic motor representation

Potential mechanisms proposed in the "Mechanisms and benefits of dynamic spatial representations" section remain to be tested. Specifically, would the spatio-temporal patterns accompanied with sequential recruitment of proximal to distal upper limb muscles differ in a predictable way from those accompanied with the recruitment of the same muscles in the reverse order? How malleable and adaptive are propagation patterns under various learning or consolidation scenarios with a movement repertoire of different natural statistics, and what are the associated time scales? Do representations or spatio-temporal patterns change on a trial-by-trial basis, and if so, in what context and to what extent? How is stable performance ensured if the representation is constantly changing? Many of these questions would be best answered with a combination of experimental and theoretical means.

To elaborate on the discussion regarding trial-to-trial changes in propagation patterns, we observed a small gradual shift in the propagation directions for the same reach direction within a subset of individual sessions. According to our analyses, this shift was not related to any of the behavioral variables examined, including various kinematics-related, task-related and performance-related variables. Might this shift reflect compensation for altered attentional states or fatigue? Additional measurements such as pupil size or eye movement tracking would be needed to address those possibilities. If those are ruled out, perhaps more interestingly, this shift might reflect some active online learning or consolidation process. Echoing what we discovered, Rokni et al. (2007) found that as primates carried out a familiar task, the directional tuning properties of motor neurons underwent a slow random drift; while during a novel task, the random shift was accompanied by systematic shifts. With the help of controlled simulations, they attributed those random shifts to local noise and high redundancy, and emphasized that those changes had to be slow to allow learning. They also hypothesized that there exists an optimal

manifold of synaptic configurations for each task, and that the brain learns several tasks with the same circuitry by moving synaptic configurations to the intersection of multiple task-optimal manifolds. Random shift signifies active explorations in the neural space, which when coupled with motor variability, could drive motor learning under reinforcement learning scheme (Dhawale et al., 2017). To concretely test these hypotheses, we could construct tasks where different levels of continuous learning is required and compare the amount of potential shifting in spatio-temporal patterning as well as in the information dynamics.

Causal influence of propagation patterns on behavior

Beyond correlative evidence, we can probe whether propagation patterns indeed play a casual role in shaping behaviors through experimental perturbations. For example, during uni-directional movements, we can electrically elicit alternative propagation patterns that correspond to other movement motifs, to see if trajectories are biased accordingly. Also, we can test if electrically-induced propagation patterns during the movement preparation stage would affect the choice of movement plans later compared with the choice of movement plans in an undisturbed situation. Additionally, we can elicit different spatio-temporal patterns while subject is at resting state, and compare the resultant muscle activities. Lastly, we could silence part of the cortical area or perturb natural patterns to different degrees, to observe the effect on movement planning and execution. For any of those artificially induced patterns, we can also manipulate its magnitude and sparseness (i.e. number of sites involved), to see if the quality of movement is affected.

Lastly, mechanistic questions could be addressed at the same time with similar paradigms. For example, we can study the mechanism of pattern formation concurrently with behaviors, by artificially stimulating two separate regions at a certain delay (to mimic the formation condition

of collision-based spiral patterns), and observe actual cortical patterns formed and associated behavioral consequences. We can also elicit patterns during several time points in an active learning process where the spatio-temporal code is constantly changing, to see if the behavior consequences change accordingly in a predictable way.

References

Abbott, L. F., Rolls, E. T., & Tovee, M. J. (1996). Representational capacity of face coding in monkeys. *Cerebral Cortex*, *6*(3), 498–505. https://doi.org/10.1093/cercor/6.3.498

Aflalo, T. N., & Graziano, M. S. A. (2006). Possible origins of the complex topographic organization of motor cortex: reduction of a multidimensional space onto a two-dimensional array. *The Journal of Neuroscience : The Official Journal of the Society for Neuroscience*, *26*(23), 6288–6297. https://doi.org/10.1523/JNEUROSCI.0768-06.2006

Arieli, A., Sterkin, A., Grinvald, A., & Aertsen, A. (1996). Dynamics of ongoing activity: Explanation of the large variability in evoked cortical responses. *Science*, *273*(5283), 1868–1871. https://doi.org/10.1126/science.273.5283.1868

Balasubramanian, K., Papadourakis, V., Liang, W., Takahashi, K., Best, M. D., Suminski, A. J., & Hatsopoulos, N. G. (2020). Propagating Motor Cortical Dynamics Facilitate Movement Initiation. *Neuron*, *106*(3), 526-536.e4. https://doi.org/10.1016/j.neuron.2020.02.011

Dhawale, A. K., Smith, M. A., & Ölveczky, B. P. (2017). The Role of Variability in Motor Learning. *Annual Review of Neuroscience*, *40*, 479–498. https://doi.org/10.1146/annurev-neuro-072116-031548

Eyre, J. A., Miller, S., Clowry, G. J., Conway, E. A., & Watts, C. (2000). Functional corticospinal projections are established prenatally in the human foetus permitting involvement in the development of spinal motor centres. *Brain*, *123*(1), 51–64. https://doi.org/10.1093/brain/123.1.51

Huang, X., Troy, W. C., Yang, Q., Ma, H., Laing, C. R., Schiff, S. J., & Wu, J. Y. (2004). Spiral waves in disinhibited mammalian neocortex. *Journal of Neuroscience*, *24*(44), 9897–9902. https://doi.org/10.1523/JNEUROSCI.2705-04.2004

Park, M. C., Belhaj-Saïf, A., & Cheney, P. D. (2004). Properties of primary motor cortex output to forelimb muscles in rhesus macaques. *Journal of Neurophysiology*, *92*(5), 2968–2984.

Park, M. C., Belhaj-Saïf, A., Gordon, M., & Cheney, P. D. (2001). Consistent features in the forelimb representation of primary motor cortex in rhesus macaques. *Journal of Neuroscience*, *21*(8), 2784–2792. https://doi.org/10.1523/jneurosci.21-08-02784.2001

Rokni, U., Richardson, A. G., Bizzi, E., & Seung, H. S. (2007). Motor Learning with Unstable

Neural Representations. *Neuron*, *54*(4), 653–666. https://doi.org/10.1016/j.neuron.2007.04.030

Rubino, D., Robbins, K. A., & Hatsopoulos, N. G. (2006). Propagating waves mediate information transfer in the motor cortex. *Nature Neuroscience*, *9*(12), 1549–1557. https://doi.org/10.1038/nn1802

Singleton, A. C., Brown, A. R., & Teskey, G. C. (2021). Development and plasticity of complex movement representations. *Journal of Neurophysiology*, *125*(2), 628–637. https://doi.org/10.1152/jn.00531.2020

Song, W. J., Kawaguchi, H., Totoki, S., Inoue, Y., Katura, T., Maeda, S., Inagaki, S., Shirasawa, H., & Nishimura, M. (2006). Cortical intrinsic circuits can support activity propagation through an isofrequency strip of the guinea pig primary auditory cortex. *Cerebral Cortex*, *16*(5), 718–729. https://doi.org/10.1093/cercor/bhj018

Takahashi, K., Saleh, M., Penn, R. D., & Hatsopoulos, N. G. (2011). Propagating waves in human motor cortex. *Frontiers in Human Neuroscience*, *5*(APRIL), 1–8. https://doi.org/10.3389/fnhum.2011.00040

Townsend, R. G., & Gong, P. (2018). Detection and analysis of spatiotemporal patterns in brain activity. *PLoS Computational Biology*, *14*(12), 1–29. https://doi.org/10.1371/journal.pcbi.1006643

Wu, J. Y., Huang, X., & Zhang, C. (2008). Propagating waves of activity in the neocortex: What they are, what they do. *Neuroscientist*, *14*(5), 487–502. https://doi.org/10.1177/1073858408317066

Xu, W., Huang, X., Takagaki, K., & Wu, J. young. (2007). Compression and Reflection of Visually Evoked Cortical Waves. *Neuron*, *55*(1), 119–129. https://doi.org/10.1016/j.neuron.2007.06.016

APPENDIX: PROPAGATING MOTOR CORTICAL DYNAMICS FACILITATE MOVEMENT INITIATION

Abstract

Voluntary movement initiation involves the modulations of large groups of neurons in the primary motor cortex (M1). Yet, similar modulations occur during movement planning when no movement occurs. Here, we show that a sequential spatio-temporal pattern of excitability propagates across M1 prior to the movement initiation in one of two oppositely oriented directions along the rostro-caudal axis. Using spatiotemporal patterns of intracortical microstimulation, we find that reaction time increases significantly when stimulation is delivered against but not with the natural propagation direction. Functional connections among M1 units emerge at movement that are oriented along the same rostro-caudal axis but not during movement planning. Finally, we show that beta amplitude profiles can more accurately decode muscle activity when they conform to the natural propagating patterns. These findings provide the first causal evidence that large-scale, propagating patterns of cortical excitability are behaviorally relevant and may be a necessary component of movement initiation.

Keywords: Motor cortex, movement initiation, propagating patterns, intracortical microstimulation, beta oscillations

Introduction

The initiation of voluntary skeletal movements is often associated with large-scale modulations of neurons in the primary motor cortex (M1) (Churchland et al., 2012; Maynard et al., 1999). It remains a mystery, however, how similar modulations in M1 neurons during movement preparation, visual observation of action, and motor imagery occur in the absence of movement (Churchland et al., 2006; Hatsopoulos and Suminski, 2011; Riehle and Requin, 1993; Solodkin et al., 2004; Tkach et al., 2007). One possibility is that modulations are weaker during these conditions and fail to exceed non-linear thresholds in downstream spinal circuitry, thus resulting in no movement (Hanes and Schall, 1996; Tkach et al., 2007; Vigneswaran et al., 2013). Yet, preparatory activity as measured during an instructed-delay paradigm often equals or exceeds movement-related activity particularly in premotor cortex which is known to provide substantial projections to the spinal cord (Hatsopoulos et al., 2004; He et al., 1993). Another possibility is that there is an active inhibitory gating mechanism preventing movement initiation that is released when movement needs to begin (Bullock and Grossberg, 1988) as has been shown during REM sleep (Chase, 1983; Pompeiano, 1967). There is, however, no evidence that such a gate exists in the context of voluntary skeletomotor behaviors. A third possibility argues that the motor cortex resides in a very high dimensional state space that allows patterns of ensemble activity related to preparation to evolve in dimensions that do not generate movement (i.e. the "output null space") in contrast to movement-relevant activity patterns that reside in an "output potent space" (Kaufman et al., 2014). Aligned with this idea, we argue that a specific spatio-temporal pattern of M1 excitability and unit modulation is a necessary component for voluntary movement initiation.

Oscillations in the beta frequency range (i.e. 15-35 Hz) as measured by the local field potential (LFP) are prevalent in various motor structures including the cerebellum, basal ganglia, and

cortical areas such as M1 (Donoghue et al., 1998; Murthy and Fetz, 1992; Sanes et al., 1995). Immediately prior to movement onset when single units begin modulating, the amplitude of these beta oscillations attenuates (Figure A.1a), and neurons lose their spiking preference to a particular phase of the beta oscillation suggesting local spike desynchronization in M1 (Chen et al., 1998; Georgopoulos et al., 1982) (Figure A.1b,c). The degree of beta oscillation attenuation in M1 is positively correlated with the magnitude of motor-evoked potentials by transcranial magnetic stimulation, indicating that beta attenuation is a mesoscopic signature of motor cortical excitability (Lepage et al., 2008; Mäki and Ilmoniemi, 2010; Schulz et al., 2014). Furthermore, the timing of beta attenuation with respect to the go signal varies with reaction time but is fixed with respect to movement onset, indicating that beta attenuation is a neural correlate of movement initiation (Figure A.1d; Figure A.S2a; see (Kühn et al., 2004; Williams et al., 2005)).

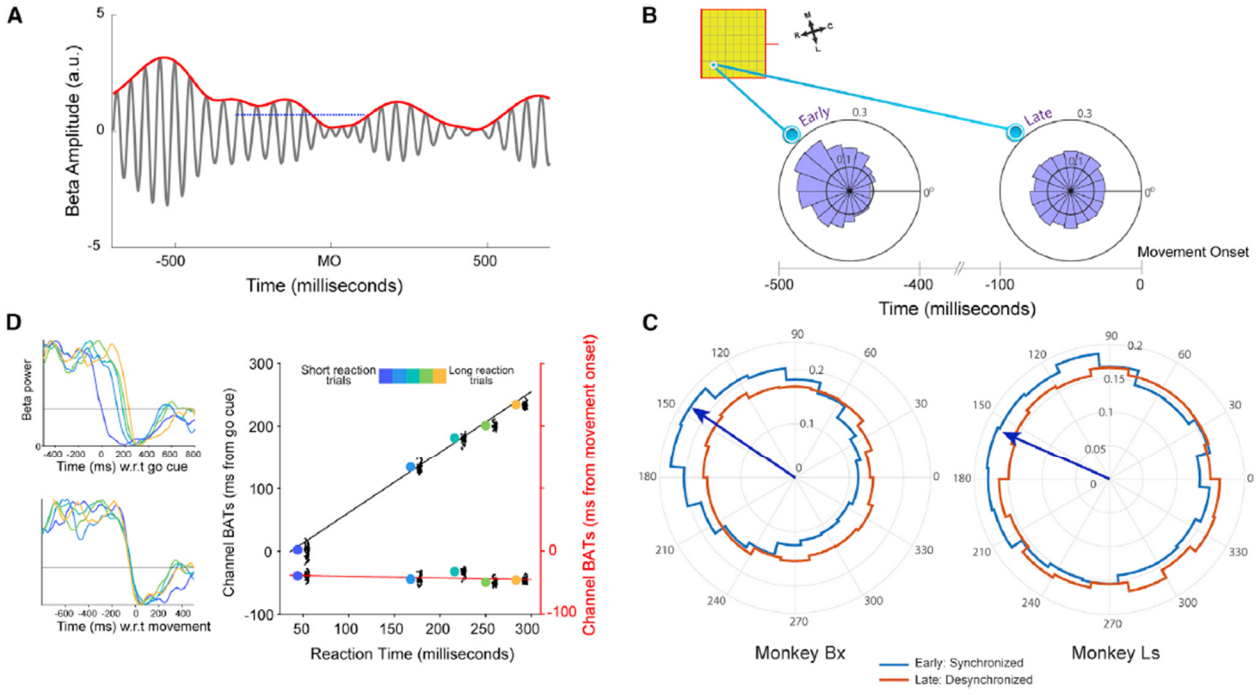

Figure A.1 Beta band power and synchrony during rest and movement. a. Beta frequency oscillations (gray) and amplitude envelope (red) on one trial from one electrode. When beta envelope drops below a threshold amplitude (blue dotted line shows a hypothetical threshold),

(**Figure A.1** continued) the corresponding timestamp denotes beta attenuation timing (BATs; see Methods on how BATs were determined). MO-movement onset. **b.** Spike-triggered beta phase histograms (see Methods) from multi-unit activity on a single electrode during movement preparation (early; -500 to -400 millisecond window w.r.t. MO) and during movement initiation (late; -100 to 0 millisecond window w.r.t. MO). **c.** Spike-triggered beta phase histograms pooled over electrodes showing a beta phase preference angle of 120 to 180 degrees in the early window (blue) exhibited desynchronization during the late window prior to movement initiation (red). Monkeys Bx and Ls showed biased distributions (Rayleigh's test; p=1.5e-309 for Bx and p=3.2e-15 for Ls; resultant direction (blue arrow) of 146^0 for Bx and 156^0 for Ls) during the early window, and, as neurons desynchronized, both resulted in uniform distributions (Rayleigh's test; p=0.504 for Bx and p=0.73 for Ls) during the late window. **d.** Normalized beta envelopes averaged over different trial groups (trials sorted by reaction time, 50 trials per group) aligned on the GO cue (top left) or on movement onset (bottom left) from one session in Ls. (Right) Channel-averaged beta attenuation time (BAT) regressed on mean reaction times (big colored dots) in each trial group with respect to the GO cue (black line, r^2= 0.996, p=0.00018) or movement onset (red line, r^2= 0.126, p=0.558). Black dots represent single channel values (offset by 10ms and jittered for clarity).

We have previously documented that trial-averaged, beta attenuation timing (BAT) does not occur synchronously across the upper limb area of M1 but rather forms a propagating sequence of cortical desynchronization (Best et al., 2017). Here, we extract single-trial beta amplitude attenuation profiles and find that attenuation propagates along one of two oppositely oriented directions along the rostro-caudal axis. By applying propagating patterns of subthreshold intracortical microstimulation (ICMS) prior to movement onset, we significantly delayed reaction time when ICMS patterns were incongruent with the natural propagating patterns. Using a network analysis on spiking activities of simultaneously recorded units, we observe that functional connections emerge immediately prior to movement onset that are oriented along the same rostro-caudal axis. Finally, by decoding muscle EMG activity from patterns of beta amplitude profiles and then applying spatial perturbations, we provide evidence that these natural propagating sequential patterns lead to normal recruitment of muscle activity.

Methods

Lead contact and material availability

Further information and requests for neural and behavioral data, and computer code should be directed to and will be fulfilled by the Lead Contact, Dr. Nicholas G Hatsopoulos (nicho@uchicago.edu).

Electrophysiology

Three male Rhesus (*Macaca Mulatta*) monkeys (Bx, Ls, and Mk) were implanted with Utah multi-electrode arrays (1.5 electrode length for Bx; 1.0 mm electrode length for Ls and Mk and 400 µm pitch from Blackrock Microsystems, Inc. Salt Lake City, UT) in the upper limb region of primary motor cortex (M1), on the contralateral side of the active limb used in the task. Monkeys Bx and Ls received two arrays with 64 recording electrodes per array (8 × 8 grid), positioned on the precentral gyrus along the medio-lateral axis and monkey Mk was implanted with one array of 100 electrodes (10 × 10 grid) (see Figure A.S1a). Surface electrical stimulation during surgical implantation was performed to guide the placement of each electrode array in the arm/hand area of primary motor cortex. Monkeys Bx and Ls were implanted with bi-polar electromyographic (EMG) electrodes in 13 individual muscles (*Anterior Deltoid, Posterior Deltoid, Pectoralis Major, Biceps Lateral, Biceps Medial, Triceps Long head, Triceps Lateral, Brachioradialis, Flexor Carpi Ulnaris, Flexor Digitorum Superficialis, Extensor Carpi Radialis, Extensor Digitorum Communis, Extensor Carpi Ulnaris*). The surgical and behavioral procedures involved in this study were

approved by the University of Chicago Institutional Animal Care and Use Committee and conform to the principles outlined in the Guide for the Care and Use of Laboratory Animals.

Neural data recorded as analog signals were amplified with a gain of 5000, bandpass filtered between 0.3Hz and 7.5 kHz, and digitized at 30 kHz. For Bx and Ls, the local field potentials were zero-phase low-pass filtered with a 10^{th} order Butterworth filter and a cut-off frequency of 500 Hz, and down-sampled to 2 kHz. For monkey Mk, the local field potentials were sampled at 2 kHz from the digitized data after low-pass filtering the signals with a 4^{th} order Butterworth filter and a cut-off frequency of 500 Hz. Multi-unit activity (MUA) was extracted as threshold crossings from the raw data after high-pass filtering with a cut-off frequency of 250 Hz. The threshold limit was set to be -5.5 times of the signal RMS value. For EMG recordings, signal from the thirteen muscles were amplified individually and bandpass filtered between 0.3 and 1 kHz prior to digitization and sampled at 10 kHz.

Behavioral Task

The animals were operantly trained to perform a center-out planar reaching task using a two-link exoskeletal robot (BKIN Technologies). The tool-tip of the robot determined the position of a cursor on a screen, and the monkeys were able to freely move the robot in the horizontal plane using their upper limb. Monkeys Bx and Ls had a vertical screen facing them such that the horizontal movements forward and back corresponded to upward and downward cursor movements. Monkey Mk used a horizontal screen with his arm and robot underneath the screen. The animals had to hold the cursor on a center target for a fixed duration (1000 ms for Bx, 900 ms for Ls, and 600 ms for Mk) to trigger a peripheral target appearance (GO cue). The animal had to

move the cursor to reach the peripheral target to get a juice reward. Monkey Bx was trained with two peripheral targets, one at 45^{o} and another at 225^{o} on a circle of radius 6 cm (where 0^{o} corresponded to rightward movements and 180^{o} corresponded to leftward movements). For monkey Ls the peripheral target was at 45^{0}, and monkey Mk was presented with targets at 270^{o}. The choice of target directions for each monkey was based on the observation that movement paths were generally straighter and were less variable across trials for these target directions.

Beta Band and Single-trial Beta Attenuation Orientation

Average power spectrograms (see Figure A.S1b) were computed with a multi-taper spectrum estimation method (time-bandwidth product and number of tapers were 3 and 5 respectively) ("Chronux Home," n.d.). Spectrograms were constructed by computing spectra over a moving window of 1000 ms with a step size of 50ms. For each window, the aperiodic "background" 1/f component was fitted and subtracted using the algorithm described in (Haller et al., 2018).

The frequency associated with the peak power in the beta frequency range (15-35 Hz) was estimated from the channel-averaged power spectral density of the neural signals from each array over a large number of trials. For monkeys Bx and Mk the beta peak occurred at 31 Hz, and for monkey Ls, the peak occurred at 21 Hz (approximated to the nearest integer value). For the Bx and Mk, a second smaller peak also occurred at 21 Hz but was not used for further analysis. The signal was then band-pass filtered with a bandwidth of 6 Hz centered on the peak beta, i.e., 31±3 Hz for monkeys Bx and Mk and 21±3 Hz for monkey Ls. The beta envelopes of the signal were computed using the magnitude of the Hilbert transformation applied to the band-pass filtered signal (see Figure A.1a).

To compute spike-triggered beta phase histograms, the instantaneous phase angle of the Hilbert transformed signal was determined whenever a spike had occurred on the same electrode. Polar histograms of those angles during the early window (-500 to -400 milliseconds with respect to movement for Bx and -700 to -600 milliseconds with respect to movement for Ls) and the late window (-100 to 0 milliseconds with respect to movement for both Bx and Ls) were used to infer synchronization/desynchronization.

Single-trial beta envelopes were extracted using an auto-encoder neural network where the inputs are the same as the targets. Segments of the signal (-500 ms to 600 ms with respect to the GO cue) from all the recorded channels were extracted for each trial and decimated to 100 Hz. A vector of length nChannels × mSamples was created for each trial and fed through the auto-encoder (see Figure A.S1c). The hidden layer was set to be half the size of the input layer so as to form a bottleneck architecture, and the data were projected to the output layer. With training, the auto-encoder was able to reconstruct the signal that preserved both spatial patterns and significant temporal variance of the signal. The output beta envelopes from the auto-encoder were then low-pass filtered with a 10^{th} order filter and cut-off frequency of 5 Hz. The filtered signals were normalized to have an amplitude range of [0, 1].

The normalized single-trial beta envelope attenuates and crosses an amplitude threshold value at a particular time (referred to as beta attenuation time or BAT) which varies depending on the channel (see Figure A.2a). These BATs, when arranged spatially on their corresponding electrode locations on the array, exhibit a propagating pattern with a particular orientation. The orientation of the beta attenuation (BAO) was estimated using a linear regression fit to the BATs as follows,

$$\widehat{BAT_{rc}} = \beta_r r + \beta_c c + \alpha$$

Equation A.1

where, β_r and β_c are the coefficients of the rows and columns of the array, and α denotes the constant offset time. The direction of BAO was then estimated as,

$$\widehat{BAO} = \arctan\left(\frac{\beta_r}{\beta_c}\right)$$

Equation A.2

The F-statistic of the model was used to ascertain statistical significance of the fit. For each trial, a BAO and its associated coefficient of determination (R^2) were calculated. On any given trial, the amplitude threshold for determining the BATs was determined by varying the amplitude from 0.5 to 0.15 in steps of 0.05 and finding the threshold with the largest associated R^2.

Patterned Electrical Stimulation

A spatio-temporal pattern of intracortical microstimulation (ICMS) was delivered to a fixed set of electrodes on the single array in Mk and the medial arrays for Bx and Ls with a fixed onset latency after the GO cue (200 ms for Bx, 50 ms for Ls, and 150 ms for Mk). Onset latency across animals varied in part because their average reaction times (under no stimulation) varied from 107 ms in Ls to 372 ms for Bx. Our goal was to perturb the natural spatio-temporal attenuation pattern which is locked to movement onset (see Figure A.1d). Because it was impossible to predict reaction time online, we stimulated at a certain fixed latency after the go cue, depending on the animal's average reaction time. Stimulation onset latency was therefore guided by the animal's behavior. The patterned ICMS propagated either rostro-caudally or caudo-rostrally which was either congruent or incongruent to the BAO for a given trial (see Figure A.3a). The directions of propagating patterned stimulation were not perfectly aligned with the BAO axis partly due to variability from

session to session but were within 45 degrees of the pooled BAO modes. As a control, there were also trials without stimulation. These three conditions (congruent, incongruent, and no stimulation) were randomly interleaved across trials for monkeys Bx and Ls. For monkey Mk, each of the three conditions was presented in multiple 25-trial blocks where each block was randomly given. The patterned ICMS consisted of trains of biphasic (200 µs negative and positive pulses with an interphase latency of 55 µs) pulses with constant subthreshold amplitude (12 µA for Bx and 5 µA for Ls). The subthreshold current for Mk during the experiments was set to be 2 µA lesser than the current levels that resulted in evoked movement during the two stimulation conditions, tested immediately prior to the experimental session. For one data set, the current per electrode was set as 14 µA for the congruent stimulation and 13 µA for the incongruent condition while in the other stimulation data set, the currents were 12 µA and 14 µA for the congruent and incongruent conditions, respectively. For monkeys Bx and Ls, a set of 8 or 16 electrodes were stimulated simultaneously at any given time (see Pattern A in Figure A.3a). Pulse trains on a successive column were initiated at a latency of 10 milliseconds relative to the previous column. For Mk, 3 or 6 electrodes were stimulated at any instance, with inter-stimulation latency of 4 milliseconds (see Pattern B in Figure A.3a). Inter-stimulation latencies for each monkey were determined by the approximate propagation speeds of trial-averaged, beta attenuation patterns that differed across animals.

Determining BAO for Trials with Stimulation

For trials that received patterned stimulation, recovering the complete beta envelopes was not possible due to large saturating electrical artifacts during stimulation. For monkey Ls the bimodal BAO distribution was highly asymmetric on non-stimulation trials (i.e. nearly unimodal). Also,

for one data session examined in Mk, the BAO distribution was highly unimodal. Therefore, we could assume a single BAO direction across stimulation trials. To determine the BAOs for the stimulation trials in monkey Bx and for the second session in Mk, an alternative approach was taken by examining the dynamics of the beta envelopes in trials when no stimulation occurred. Typically, the channel-averaged beta envelope exhibits a local peak in amplitude at different times prior to attenuation depending on the trial. The approach was to find a time window around the GO cue where the local beta peaks occurred on a subset of no stimulation trials such that their BAO distribution was highly unimodal. This time window (set to 300 ms in duration; 150 ms for monkey Mk) was found by sliding the window in 100 ms steps starting at -300 ms with respect to the GO cue, selecting no stimulation trials whose local beta peak occurred in that window, and computing the BAO distribution. The window whose selected trials were highly unimodal (where at least two thirds of the trials in the window were oriented along one BAO mode) in their BAO was chosen and then used to select stimulation trials whose local beta peak occurred in the same window. The assumption was that these stimulation trials exhibited a similar unimodal BAO distribution and, therefore, all these stimulation trials had BAOs pointing roughly in the same direction. To detect local beta peaks in stimulation trials, partial beta envelopes (-500 ms to 200 ms with respect to the GO cue for Bx and Ls; -500 to 25 ms for monkey Mk) that were not corrupted by electrical artifacts were extracted using the auto-encoder. Whenever multiple time windows exhibited unimodal BAOs in the no stimulation trials, the window that was closer to or overlapping the GO cue was chosen. To compute reaction time means and distributions for all three conditions, we excluded trials whose movement onset times occurred before the onset of the stimulation as well as trials with very long reaction times (>500 ms for Bx and Mk and >300 ms for Ls).

Computing Reaction Times of Single Trials

Tangential velocity trajectories estimated from the Cartesian position of the reaching kinematics data sampled at 2 kHz were used for reaction time computation. From the normalized trajectories of each trial, movement onset times were computed when the velocity crossed 10% of the peak velocity. When there were smaller velocity peaks that exceeded the 10% threshold prior to final velocity peak associated with the actual movement to the target, movement onset was computed using the final threshold crossing.

Firing rates

Multi-unit firing rates were calculated for each trial in 150 ms temporal windows, shifted over time with steps of 10 ms. Rates were then averaged over trials to obtain the mean firing rate of each channel's multi-unit. For the heatmaps of Figure A.4a, mean firing rates were normalized by dividing by the multi unit's maximum rate. A different normalization procedure was used to compare the firing rates of each mode (Figure A.S3). First the average baseline activity over all trials (500ms prior to the go cue) was subtracted from each trial's firing rate. Then, trials were separated into three groups according to the BAO mode (rostro-to-caudal BAO, caudo-to-rostral BAO, outside of the 2 modes) and the average firing rate of each group was calculated. If the multi-unit displayed suppressed modulation, its rates were converted to the additive inverse. Finally, the three average rates were divided by the global maximum, in order to retain possible mode differences. Population responses for the three groups were then estimated by averaging over multi-units. To compare the population responses between groups, we used the normalized unit

responses at two different epochs: reaction (from go cue to movement onset) and movement (from movement onset to movement end). A one-way AVOVA was done separately at each epoch [factor: BAO mode (three levels), sample size: number of multi units] to determine differences between the population firing rate across the three groups.

Directed Functional Connectivity

A granger-type causality estimation technique generalized for point-processes was used to infer directed connectivity among simultaneously recorded neurons. For each candidate multi-unit, the instantaneous spiking was modeled as its conditional intensity function (CIF), $\lambda(t|H(t))$, where $H(t)$, is the spiking history of all the multi-units in the ensemble up to time t. Using a generalized linear model, the log CIF of each multi-unit was modeled in terms of the spiking of its covariate (i.e. source) multi-units, initially with a history of 60 milliseconds binned at 3 millisecond resolution for each source multi-unit. The final model was then found by optimizing the length of the history term using the AIC (Akaike information criterion). To determine the influence of a source multi-unit on a candidate multi-unit, the log-likelihood ratio between models (i) including and (ii) excluding the source multi-unit was computed, and when the model performance decreased significantly ($p \leq 0.05$, χ^2-test, false detection rate corrected for multiple comparison) with the source multi-unit excluded, a directed connectivity from the source multi-unit to the candidate neuron was inferred.

Decoding Muscle Activity from Beta Envelopes

A feed-forward neural network was developed to map instantaneous beta amplitudes from multiple channels to the EMG activity of a group of muscles. Normalized beta envelopes from 60 channels (100 samples/second) were projected first through the auto-encoder and then fed into the feed-forward neural network to decode 5 muscles based on their relevance to the task and the quality of the signal (Anterior Deltoid, Pectoralis Major, Biceps Lateral, Triceps Long head, Flexor Digitorum Superficialis). The inputs were vectors of 60 × 1 elements, and the outputs were vectors of 5 × 1 elements. The neural network architecture (see Figure A.6a) used 120 hidden neurons with logarithmic sigmoid activation function. The output layer that predicts the EMG activities used a linear transfer function. Of the available trials, 80% were used for training and 20 % for testing. The prediction accuracy was computed for each individual muscle as the fraction of variance accounted for (*FVaF*) between the actual EMG and the EMG predicted from the neural network as,

$$FVaF_{muscle} = \left(1 - \frac{var(EMG_{act} - EMG_{Pred} - mean(EMG_{act} - EMG_{Pred}))}{var(EMG_{act})}\right) \times 100$$

Equation A.3

The input to the network was perturbed by swapping the spatial locations of the channels in two different ways. For each swap, beta profiles on eight electrodes were randomly selected on the 64 electrode array and then randomly swapped spatial locations with other beta profiles with the constraint that swapping occurred either parallel to or orthogonal to the BAO axis. A total of 5000 swaps were performed for each of the directions (parallel or orthogonal) and the *FVaF* for each swap was estimated.

Somatotopic Maps

In order to determine the somatotopy of M1, supra-threshold electrical stimuli (a train of 25 biphasic pulses with 200 µs pulse width per phase and 55 µs interphase interval and 330 Hz; current levels varied from 10 µA to 70 µA per electrode) were delivered to each single electrode one at a time and the corresponding evoked responses documented (H.C. Kwan et al., 1978). Two observers noted the responses while a third individual delivered the stimuli using a Blackrock Microstimulator R96 system (Blackrock Microsystems, Inc. Salt Lake City, UT). Certain muscles were also palpated to identify any evoked responses. We used a 7-point scale (color-coded in Figure A.5) to label each site from (fingers, red), to wrist (yellow), to elbow (baby blue), to shoulder (blue) joint and/or muscle twitches. Regression was performed relating the 7-point scale to the position of the electrode to compute the proximal-to-distal gradient. In monkeys Bx and Ls, regressions were performed using both medial and lateral arrays.

Quantification and statistical analyses

Throughout this paper, a statistical test was deemed significant when the resulting p-value was lower than 0.05, unless otherwise noted. Details about the specific statistical test, sample number, and any post-hoc corrections can be found in the results section and in the corresponding figure captions.

Results

Single-trial propagating patterns of beta attenuation

Three rhesus macaque monkeys (Bx, Ls, and Mk) were trained on a simple reaction time task to perform planar reaching movements by moving a cursor to visual targets using a two-link robotic exoskeleton (BKIN Technologies, ON, Canada) while multi-unit activity and LFPs were simultaneously recorded from multi-electrode arrays implanted in the upper limb area of M1 (Figure A.S1a). Monkey Bx was trained to make movements in two opposing directions (45^{o} and 225^{o}), and monkeys Ls and Mk made movements to one direction (45^{o} and 270^{o}, respectively). 0, 90, 180 and 270 degree movements correspond to directions to the right, away from the body, left, and into the body, respectively. LFP signals were band-pass filtered centered at the frequency of peak power in the beta frequency range (15-35 Hz: 31±3 Hz for monkeys Bx and Mk, and 21±3 Hz for monkey Ls; see Methods) from which beta amplitude profiles were computed using the Hilbert transform. Traditionally, beta amplitude dynamics are determined by trial-averaging beta profiles in order to reduce noise (Murthy and Fetz, 1996; Pfurtscheller and Lopes da Silva, 1999; Salmelin and Hari, 1994). However, trial-averaging conceals possible interesting beta dynamics that vary from trial to trial (Pernet et al., 2011). To extract single-trial beta profiles, we used an auto-encoder that was trained to generate de-noised versions of the input beta signals (Figure A.S1c). These single-trial, de-noised profiles exhibited characteristic attenuation (i.e. desynchronization) prior to movement initiation, a mesoscopic signature of cortical excitability (Lepage et al., 2008; Mäki and Ilmoniemi, 2010; Schulz et al., 2014). More importantly, these beta dynamics revealed spatial gradients that evolved in time indicative of spatio-temporal patterns that propagated in one of two oppositely oriented directions along a rostro-caudal axis in M1 (Figure A.S2b).

For each trial, we quantified the propagation direction of beta attenuation time prior to movement initiation by first determining when each electrode's normalized beta profile dropped below a threshold. We then used linear regression to predict beta attenuation times (BATs) from the spatial locations of each electrode (see Equation 1), where the electrode location on the array (*x* and *y* coordinates) was the independent variable and the corresponding BAT was the dependent variable. The regression coefficients could then be used to compute the orientation from early to late BATs (see Equation 2) which we refer to as the beta attenuation orientation (BAO) for that trial. Trials that satisfied the criterion of $R^2 \geq 0.2$ ($p \leq 0.05$, F-Statistic; number of trials = 1369/1868 (73%) for Bx making 45 degree arm movements; 1417/1909 (74%) for Bx making 225 degree arm movements; 1626/1723 (94%) for Ls; and 278/366 (76%) for Mk) from the regression fits were retained for further analyses. The single trial BAOs were primarily directed in one of two oppositely oriented directions (Figure A.2b). In other words, beta attenuation propagated along one axis, but not always in the same direction along that axis. For all three monkeys, the distributions of single-trial BAOs (pooled over 11 sessions for Bx making 45 degree movements and 11 sessions for Bx making 225 degree movements, 9 sessions for Ls, and 4 sessions for monkey Mk) were bimodally distributed along a roughly rostro-caudal axis (rostromedial-caudolateral axis for Bx and Mk and rostrolateral-caudomedial axis for Ls) albeit the two modes were not always equal in size (Figure A.2b). The BAO distributions were well fit by a mixture of von Mises functions model with means of 143° and -33° for Bx for 45 degree arm movements, and 137° and -32° for 225 degree arm movements; 33° and -126° for Ls; and 137° and -20° for Mk. The BAO distributions for the two movement directions in Bx were not statistically different ($p=0.1$, Kuiper's two sample test). Multi-unit activity was not statistically different for trials in either of the modes and the few trials that fell outside of the two modes (one-way ANOVA for 3

groups, p-values ranging from 0.21 to 0.99 for different datasets; Figure A.S3). However, trials in which the BAO propagated in the rostro-to-caudal direction had significantly shorter reaction times as compared to trials with caudal-to-rostral propagation in two of the monkeys (mean reaction time of 387 and 405 milliseconds, respectively, for Monkey Bx making 45 degree movements, p = 0.0049, two-sample t-test (not significant for 225 degree movements, p = 0.4); 119 and 143 milliseconds for Monkey Ls, p = 0.0002, two-sample t-test;).

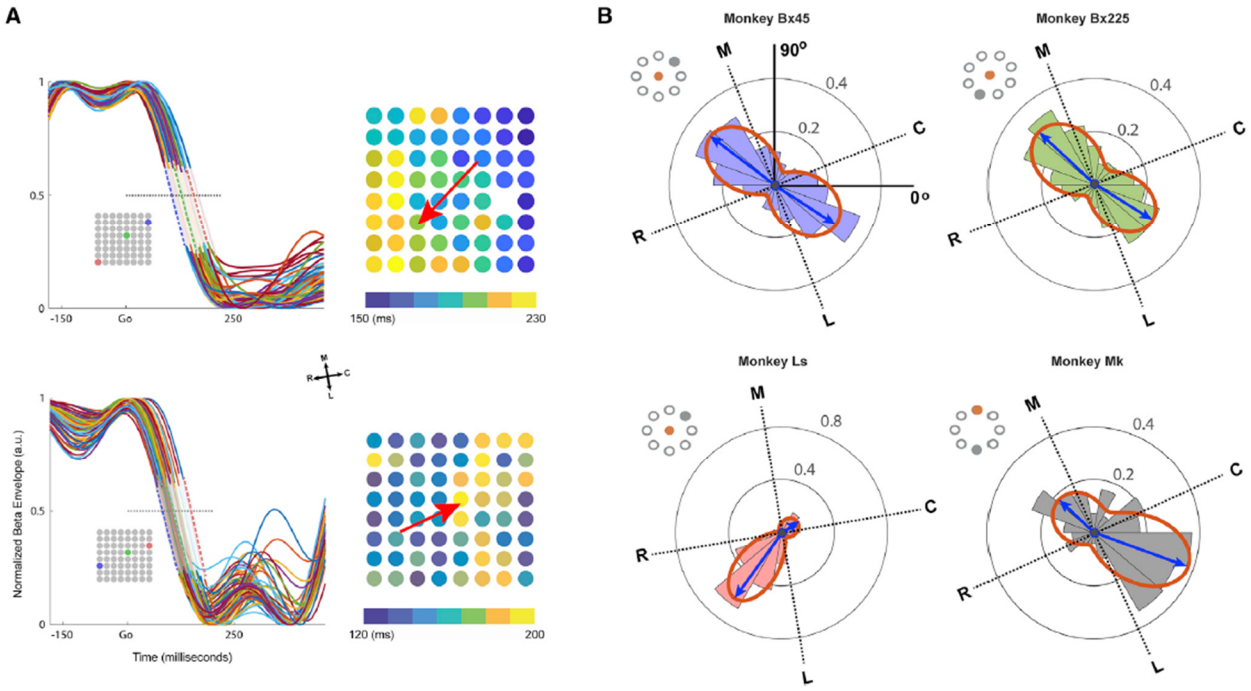

Figure A.2 Single trial beta attenuation propagates along one of the two directions along a rostrocaudal axis. a. Beta envelopes of two trials (left; inset shows spatial positions of three electrodes with early (blue), intermediate (green), and late (red) attenuation times) and their corresponding spatial maps of beta attenuation times (right) are shown for monkey Ls. Regression fits to the pattern show the beta attenuation orientation (BAO) directed rostrally or caudally (red arrows). **b.** Polar histograms show the distributions of BAOs across multiple single trials and recording sessions for three monkeys (a total of 1369 and 1417 trials in 11 sessions in Bx45 and Bx225, respectively; 1626 trials in 9 sessions in Ls; and 278 trials in 4 sessions for Mk). A mixture of two von Mises functions was fit to the BAO distributions (red curves) to estimate the two direction modes of the BAO (blue arrows). Insets represent the initial hold (filled red) and target positions (filled gray) of the hand.

Evidence using electrical stimulation linking propagating patterns to movement initiation

To provide more direct evidence that propagating patterns facilitate movement initiation, we conducted experiments designed to perturb movement initiation in which subthreshold, patterned electrical stimulation across a set of electrodes was delivered during the reaction time period (Figure A.3a). We hypothesized that patterned electrical stimulation that propagated against (INCONGRUENT) the natural propagating pattern of beta attenuation would delay movement initiation as compared to patterned stimulation that propagated with (CONGRUENT) the natural propagating pattern (see Methods). Given that the BAO varied from trial to trial (i.e. along the rostro-caudal or caudo-rostral directions), we could not assume a particular BAO on any given stimulation trial. For this reason, we stimulated trials randomly in one of the two directions and later sorted them as INCONGRUENT or CONGRUENT offline. Due to the bimodality of the BAOs, the characterization of a stimulation trial as INCONGRUENT or CONGRUENT did not necessarily indicate whether the BAO was rostral-to-caudal or caudal-to-rostral. Instead, each group could contain both types of BAO. The offline process of identifying the BAO in stimulation trials and sorting them in the two groups was challenged by the presence of stimulation artifacts. This was not an issue for monkey Ls as the bimodal distribution of BAOs was highly asymmetric on non-stimulation trials (i.e. nearly unimodal). Therefore, we could assume a single BAO direction across stimulation trials (2086 trials recorded over 13 sessions). For monkey Bx where the BAO distribution was nearly symmetric, we devised a method for selecting a subset of stimulation trials that we could assume had a highly unimodal BAO distribution based on no stimulation (NOSTIM) trials (see Methods). Only this subset of trials was analyzed for Bx (657/1772 or 37% of stimulation trials for 45 degree movement and 724/1686 or 43% of stimulation trials for 225 degree movement). Likewise, for monkey Mk, a similar procedure was

applied to select a subset of trials (84/187 or 45% of stimulation trials) from one of the datasets that showed a bimodal distribution. The second data set from Mk exhibited a highly unimodal distribution on NOSTIM trials. It should be emphasized that the assumption of unimodality is conservative and likely leads to weaker differential effects on reaction time given that some stimulation trials may have had BAOs directed in the opposite direction.

Reaction time distributions for the INCONGRUENT condition were significantly delayed as compared to those in the CONGRUENT condition for all three monkeys (Figure A.3b; $p = 0.009$ for Bx for 45 degree reaches and $p = 0.001$ for Bx for 225 degree reaches; $p = 0.019$ for Ls; and $p = 0.03$ for Mk, two-sample KS test comparing INCONGRUENT and CONGRUENT conditions). No significant difference in RT distributions was observed between CONGRUENT and NO STIM conditions ($p = 0.17$ for Bx for 45 degree reaches and $p = 0.08$ for Bx for 225 degree reaches; $p = 0.64$ for Ls; and $p=0.49$ for Mk, two-sample KS test). Mean reaction times were significantly longer for INCONGRUENT trials as compared to CONGRUENT and NOSTIM trials for all three monkeys (Figure A.3c, $p < 0.05$, F-statistic ANOVA; post-hoc Bonferroni correction). For CONGRUENT, INCONGRUENT, and NOSTIM trials, mean (standard error) reaction times for Bx (45 degree reaches) were 375 (2.2), 386 (2.2), and 372 (2.9) milliseconds, respectively, and for Bx (225 degree reaches) they were 363 (2.5), 377 (2.5), and 360 (2.75) milliseconds. For Ls mean reaction times were 160 (2.12), 169 (2.18), and 161 (2.15) milliseconds Monkey Ls tended to anticipate the presentation of the GO cue leading to very short reaction times. For Mk, the corresponding mean reaction times were 366 (6.5), 390 (7.2) and 357 (6.0) milliseconds. By comparing session mean reaction times over all 27 stimulation sessions and all three monkeys, INCONGRUENT session reaction times were significantly longer than those in CONGRUENT sessions ($p = 2.4e\text{-}5$, paired, two-tailed t-test, Figure A.3d).

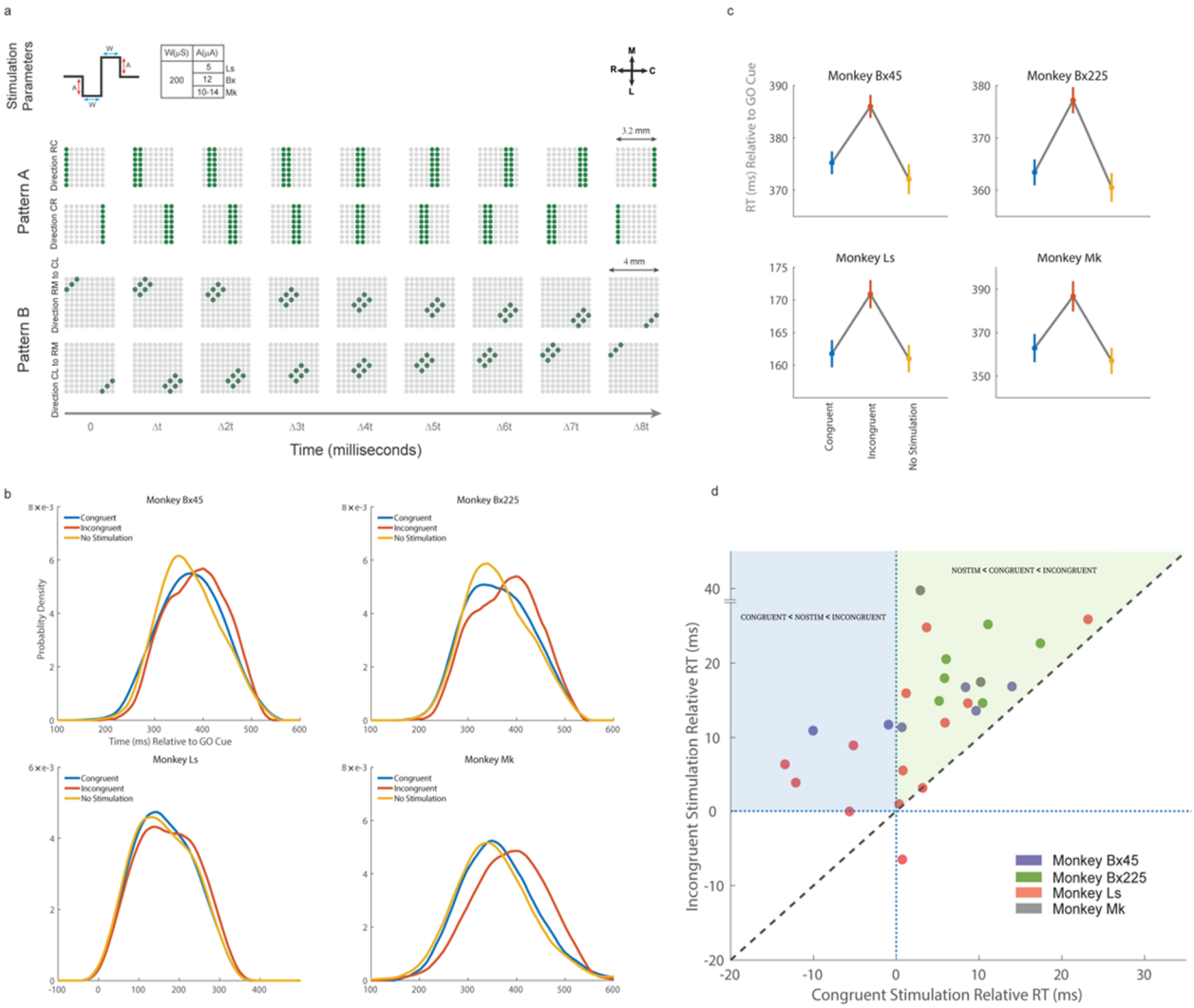

Figure A.3 Spatio-temporal stimulation affects reaction time. a. The stimulus was a biphasic pulse with sub-threshold currents (top), delivered concurrently over sets of electrodes with a propagation latency (Δt) of 10 milliseconds (4 milliseconds for Monkey Mk). Stimulation patterns were delivered to a group of electrodes propagating from rostral to causal sites or vice versa (Pattern A, middle) or diagonally (Pattern B, bottom). The stimulus patterns were delivered either along the BAO direction (CONGRUENT) or against the BAO direction (INCONGRUENT). **b.** The distributions of reaction times across trials for the two stimulation conditions along with those trials that received no stimulation (NO STIMULATION) are shown for Bx45 (731, 727, and 676 trials for CONGRUENT, INCONGRUENT, and NO STIMULATION), Bx225 (674, 650, and 595 trials), Ls (1028, 1048, and 1038 trials), and Mk (106, 91, and 168 trials). **c.** Mean (standard error) reaction time in the three conditions show that the INCONGRUENT stimulation resulted in delayed reaction compared to the other two conditions. **d.** Scatter plot comparing the mean reaction times between the two stimulation conditions from 27 individual experimental sessions over all three monkeys. The mean reaction time of the NO STIMULATION from each session was subtracted from the mean reaction times of the other two conditions. The diagonal dashed line represents the identity line, and the dotted lines show the zero mark. The shaded areas highlight regions where reaction times in the

(**Figure A.3** continued) INCONGRUENT condition are longer than in the CONGRUENT condition but also reaction times in the NO STIMULATION condition are longer than in the CONGRUENT condition (blue shaded area) or, alternatively, reaction times in the CONGRUENT condition are longer than in the NO STIMULATION condition (green shaded area).

Functional connectivity emerges along the rostro-caudal axis at movement initiation

If beta attenuation as measured by the LFP is truly a reflection of local network excitability and ultimately activation, we would expect a similar spatio-temporal pattern to emerge among unit activity at movement initiation. To characterize spatio-temporal patterning in neuronal spiking, we estimated functional connectivity among unit activity at different epochs during the reaching behavior in monkeys Bx and Ls (Figure A.4a). Monkey Mk was excluded from this analysis due to an inadequate number of channels with spiking activity. We used a Granger-type statistical model applied to point processes (Kim et al., 2011; Takahashi et al., 2015) to predict multi-unit activity (MUA) from one electrode based on the past MUAs of other electrodes (i.e. source) to infer the directed network connectivity among all simultaneously recorded electrodes (See Methods). The angle of each significant, directed connection between two electrodes was determined based on the spatial locations of the two electrodes. Each significant connection was then binned to create polar histograms (accounting for both excitatory and inhibitory connections as determined by the sign of the sum of history coefficients associated with the source electrode) representing different directions across the motor cortical sheet. During the movement preparation epoch (an epoch that spanned the GO cue so spiking reflected in part generic preparation without movement direction information), polar distributions of functional connectivity were estimated and were fitted by a mixture of two von Mises functions with means of -92° and 100° in Bx for 45

degree reaches (Figure A.4b, top), and -72° and 95° for 225 degree reaches (Figure A.4b, middle), and -67^{o} and 128^{o} in Ls for 45 degree reaches (Figure A.4b, bottom). For the movement initiation epoch, the von Mises means shifted orientation to -38° and 119° in Bx for 45 degree reaches (Figure A.4c, top) and -50° and 125° for 225 degree reaches (Figure A.4c, middle), and -123^{o} and 60^{0} in Ls for 45 degree reaches (Figure A.4c, bottom). A bimodal distribution ($p = 0.004$ for Bx 45 degree reaches and $p = 3.9e\text{-}5$ for Bx 225 degree reaches, $p = 0.01$ for Ls; Rayleigh test for uniform circular distribution modified to test for bimodality; a spatial shuffling test also indicated significant bimodality (see Figure A.S5) of connectivity emerged along a rostro-caudal axis during movement initiation that was similar to the BAO distribution ($p = 0.1$ in Bx for 45 degree reaches and $p = 0.05$ for 225 degree reaches, and $p = 0.055$ for Ls; Kuiper's two sample test). Moreover, the functional connectivity distributions for the two movement directions in Bx were not statistically different ($p=0.9$, Kuiper's two sample test). In contrast, functional connectivity during movement preparation showed a distribution that was significantly different from the BAO distribution ($p = 0.02$ in Bx for 45 degree reaches and $p = 0.001$ for the 225 degree reaches, and $p = 0.0001$ in Ls; Kuiper's two sample test).

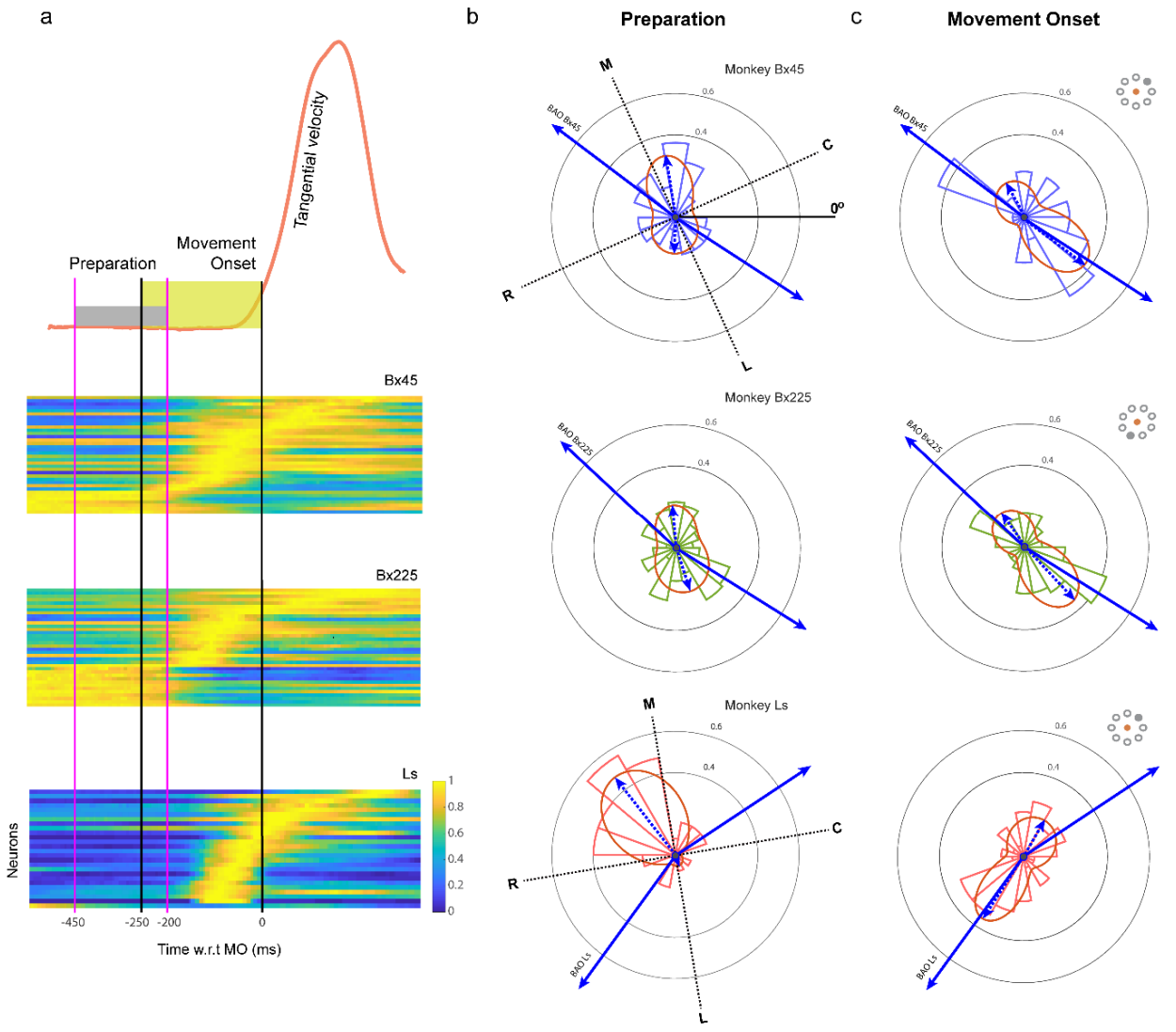

Figure A.4 Functional connections among neurons emerge along the BAO axis during movement onset. a. Multi-unit activity (MUA) from a population of M1 neurons was used to estimate functional connectivity during movement preparation and movement onset epochs. MUA for each electrode was normalized to its peak activity and sorted by time of peak activity. MUA from 60 and 64 electrodes are shown for Bx and Ls, respectively. **b.** Polar histograms of the orientation of functional connections during the movement preparation epoch (top, Bx for 45 degree movements; middle, Bx for 225 degree movements; bottom, Ls for 45 degree movements). The von Mises fits (red curves and dashed blue arrows) show functional connectivity distributions that were different from the BAO modes (blue arrows). A total of 95, 128, and 54 significant connections were found for Bx45, Bx225, and Ls, respectively. **c.** During the movement onset epoch, the neuronal functional connection distributions were oriented similar to the BAO distributions. A total of 52, 102, and 36 significant connections were found for Bx45, Bx225, and Ls, respectively.

In order to more effectively isolate the neural dynamics of movement planning from movement execution, we also examined functional connectivity during an instructed delay task for monkey Bx where the target stimulus was presented for a random duration ranging from 500 to 1200 milliseconds before a go cue to initiate the movement. Only trials with instructed delay durations longer than 1000 ms were used for the functional connectivity analysis. It is known that single units in primary motor cortex modulate during the instructed delay period where there is no movement (Crammond and Kalaska, 2000; Hocherman and Wise, 1991). We assessed the orientation of directed functional connections during the early (Figure A.S4, left) and late planning (Figure A.S4, right) epochs during the instructed delay period. Mixture models fit to these epochs showed von Mises means that were oriented nearly orthogonal to the BAO axis.

Propagating sequences and somatotopy

We examined the spatial relationship between the propagating sequences and the somatotopic organization of M1, as determined using suprathreshold electrical stimulation. This was performed to see if the somatotopy has any noticeable spatial orientation aligned with the propagating patterns. We stimulated each electrode and documented the evoked movement or muscle twitches through visual observation and muscle palpation in each of the three animals (Figure A.5). Given the nature of the behavioral task (i.e. a reaching task involving primarily proximal muscles), we confined our analysis of propagating sequences on arrays placed primarily in the proximal zone even though we had an additional array (in Bx and Ls) placed in the distal zone. Despite the crude somatotopy as others have documented (H. C. Kwan et al., 1978; H C Kwan et al., 1978; Park et al., 2004, 2001), we found that the axis of propagation was not aligned with and, in fact, was nearly orthogonal to the medio-lateral gradient from proximal to distal representations.

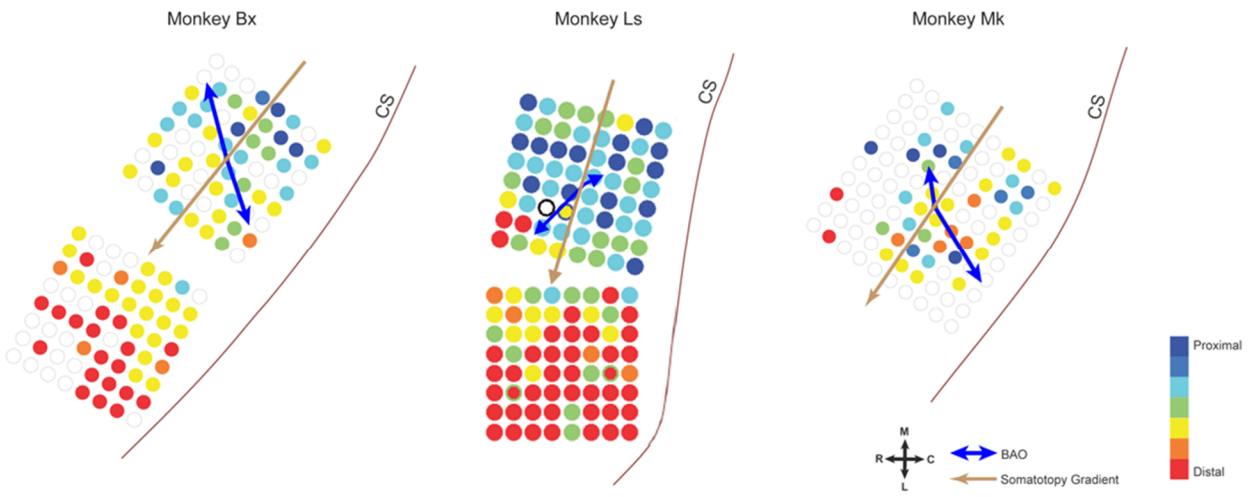

Figure A.5 Propagating sequence directions do not follow the somatotopic organization. The somatotopic maps across the arrays implanted in the three monkeys show a proximal-to-distal somatotopy (colored dots) oriented along the medio-lateral axes. The somatotopic maps for Bx and Ls are based on two 8x8 arrays implanted medio-laterally in M1. The BAO axes (blue arrows), computed for the medial arrays in Ls and Bx and the one array in Mk are nearly orthogonal to the proximal-to-distal gradient (brown arrows). (see Figure SA.5 for statistical robustness of the somatotopic gradient estimates)

Propagating patterns along the rostro-caudal axis more reliably predict muscle activity

We hypothesized that downstream areas such as the spinal cord (and motor neuron pools) may be sensitive to the spatio-temporal recruitment order of cortical neurons. Beta oscillation dynamics are likely not involved in the detailed components of movement execution (Murthy and Fetz, 1996). However, evidence has shown that cortical oscillations and muscle EMGs are related and exhibit significant coherence in the beta frequency range under certain behavioral conditions (Baker et al., 1997). More importantly, this coherence can modulate continuously and is related to motor parameters (Kilner et al., 2000). One way to test the idea that propagating beta attenuation may facilitate muscle recruitment is to decode muscle activity from beta amplitude profiles in cortex and then apply different spatial perturbations to the beta profiles. Using cortical LFP and

EMG data from Bx and Ls, we trained a feed-forward neural network (Figure A.6a, see Methods) using the Levenberg-Marquardt algorithm (Hagan and Menhaj, 1994; Marquardt, 1963) to reconstruct a subset of 5 EMG signals (muscles recruited during the task condition; reaching movements to the target at 45^{o}) from a set of cortical beta profiles (Figure A.6b and Figure A.S6a). Reconstruction performance on test data not used to train the network was assessed by the fraction of variance accounted for (FVaF in percentage) and ranged from 18% to 55% on all five muscles with an average of 40.5% for Bx and ranged from 15% to 51% on all muscles with an average of 36.5% for Ls. Our goal here was not to develop an accurate decoding algorithm for brain-machine interface applications, but rather to adequately reconstruct muscle activity with a model that could then be used to apply desired spatial perturbations. We applied two kinds of spatial perturbations (random swaps) to the model's input: a swap 1) parallel to or 2) orthogonal to the BAO axis (See Methods; Figure A.6c). A total of 5000 swaps were performed for each perturbation type from which a distribution of FVaFs were generated and compared to each other as well as to the unperturbed FVaF (Figure A.6d and Figure A.S6b). Only the parallel perturbation would disrupt the natural sequencing of beta attenuation propagation, and, therefore, we predicted that such perturbations would more effectively disrupt EMG output from the neural network model. Mean FVaFs were, in fact, significantly lower for the parallel perturbations as compared to orthogonal perturbations ($p = 6.6e\text{-}200$ for Bx and $p = 3.6e\text{-}84$ for Ls, two sample t-test).

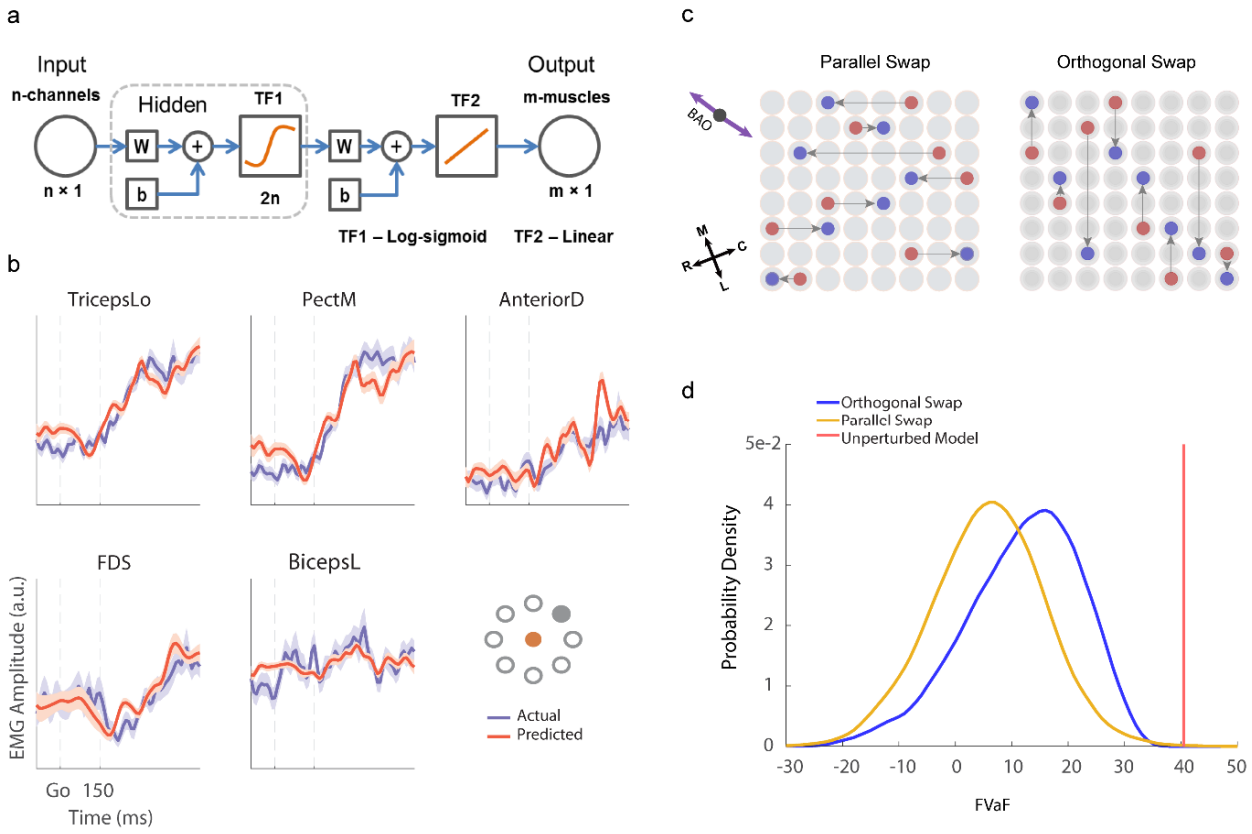

Figure A.6 EMG prediction is more sensitive to perturbations along the BAO axis. a. A feed-forward back propagation neural network architecture that maps instantaneous beta amplitudes to electromyographic (EMG) from 5 muscles that were active during the particular movement condition. **b.** Trial-averaged predicted EMG values (red) are overlaid on the actual trial-averaged EMG signals (blue) for Bx. **c.** Perturbation of the spatiotemporal pattern was performed along the BAO axis (parallel swap) or orthogonal to it (orthogonal swap), and FVaF of the model's performance was computed. **d.** Distributions of FVaFs over 5000 swaps are shown for the parallel swap condition (yellow; mean FVaF of 6.5%) and the orthogonal swap condition (blue; mean FVaF of 12%) along with the FVaF of the original unperturbed model (red line; mean FVaF of 40.5%). Inset represent the initial hold (filled red) and target positions (filled gray) of the hand.

Discussion

This work provides important evidence demonstrating that a specific, propagating rostro-caudal pattern of M1 desynchronization and unit modulation is a necessary component for voluntary movement initiation. First, we showed that single-trial propagating patterns exhibit a bimodal

distribution of directions, in which the two modes are opposite to each other. In other words, the patterns propagated in one of two directions along a rostro-caudal axis. Second, using subthreshold patterned electrical stimulation, we showed that patterned stimulation that propagates against the natural propagating direction (INCONGRUENT) leads to longer reaction times whereas stimulation propagating with the natural pattern (CONGRUENT) did not affect reaction times. While these perturbation experiments do not prove that propagating beta attenuation patterns have a causal role on movement initiation, the fact that patterned stimulation that is incongruent as opposed to congruent with the natural propagating direction on a trial-by-trial basis results in longer reaction times does provide strong evidence that the natural propagating patterns are involved in movement initiation. While any form of electrical stimulation will perturb the natural cortical dynamics associated with movement initiation, we suggest that the patterned stimulation propagating against the natural sequence provides a more potent perturbation. In fact, even CONGRUENT stimulation can slow reaction time in some cases but not as much as INCONGRUENT (see monkey Bx225, Figure A.3d). By timing the stimulation around desynchronization we argue that we have perturbed the spatio-temporal dynamics of neural activation associated with movement initiation and that INCONGRUENT stimulation more effectively perturbs these dynamics resulting in slower reaction. We did not observe significantly shorter relative reaction times in the CONGRUENT condition. This may be due to the fact that even congruent stimulation represents an unnatural form of input to cortex that will weakly perturb the ongoing cortical dynamics (See, however, six experiments to the left of zero in Figure A.3d (blue shaded area) where relative reaction time was negative in the CONGRUENT condition indicating faster reaction times relative to no stimulation). Subthreshold ICMS at single sites has been previously shown to lead to increased reaction time in dorsal premotor cortex followed by

normal motor execution (Churchland and Shenoy, 2007). Importantly, similar effects on reaction time were absent for similar single site, subthreshold ICMS in M1. We argue that single site stimulation may not be the ideal paradigm for perturbing the cortical dynamics in M1 associated with movement initiation. This is significant, more generally, as it suggests that spatiotemporally patterned stimulation may provide a more potent perturbation paradigm in other cortical areas that exhibit spatio-temporal patterning.

Second, functional network connectivity among an ensemble of spiking neurons emerges at movement initiation that is spatially anisotropic and oriented along a similar rostro-caudal axis. This was not observed during movement preparation or planning even though it is known that M1 neurons modulate during these periods (See Figure A.4 and Figure A.S4). Spatial structure in functional connectivity was often weak during movement preparation and planning, and, if anything, its spatial anisotropy was oriented orthogonal to the rostro-caudal axis.

Anatomical and physiological studies have suggested a spatial anisotropy of horizontal connectivity in M1 that might support these spatially organized propagating sequences. Retrograde axon degeneration following punctate lesions in M1 has indicated longer range horizontal connectivity along the rostro-caudal axis as compared to the medial-lateral axis (Gatter et al., 1978). Moreover, an ICMS study has provided evidence for dominant functional connectivity along the rostro-caudal axis (Hao et al., 2016).

These beta attenuation patterns observed at the single-trial level are novel and distinct from the beta waves (as measured by the phase gradient of the beta oscillations) we and others have previously documented to occur during movement preparation (Denker et al., 2018; Rubino et al., 2006; Rule et al., 2018; Takahashi et al., 2015, 2011). However, these two phenomena may be related as they both exhibit bimodal propagating distributions along a roughly rostro-caudal axis.

This may suggest a mechanism by which on-going beta waves propagating along the rostro-caudal axis during movement preparation lead to a sequential pattern of neural activation prior to movement initiation. Beta waves alternately propagate either in the rostral-to-caudal direction or vice versa in a seemingly random fashion during movement preparation. It is also known that excitability is enhanced at particular phases of the beta oscillation (Murthy and Fetz, 1996) (See also Figure A.1b,c). Therefore, as a particular beta wave travels across the cortical sheet in one direction, a wave front of excitability moves across the motor cortex in the same direction. Assuming input originating from outside of motor cortex signaling movement initiation interacts with this beta wave, the combination will more likely lead to firing at that position in motor cortex. The traveling wave front may, therefore, lead to a sequential pattern of activation.

An open question is how these propagation patterns are mechanistically related to appropriate muscle activations for movement initiation. One possibility is that rostro-caudal propagation enhances M1 output through recurrent connectivity due to stronger rostro-caudal horizontal connectivity. However, M1 firing rates for trials when propagating beta attenuation occurred along the rostro-caudal axis were not statistically different from those few trials when propagation occurred outside the rostro-caudal axis. Another possibility is that downstream areas such as the spinal cord are sensitive to the recruitment order of cortical sites. Our muscle decoding results indirectly supports this possibility. Perturbing the spatial order of beta amplitude inputs along the rostro-caudal axis more effectively disrupts the natural propagating patterns and leads to significantly weaker EMG predictions as compared to orthogonal perturbations which preserve the overall propagation pattern.

The sensitivity of downstream receiving populations to these cortical propagating sequences could be due to the specific characteristics of these patterns. For example, the propagation axis can be

thought of as a composition of two phenomena: simultaneous activation of populations orthogonal to the propagating axis (i.e. along the medio-lateral axis) and sequential activation of populations along the propagating axis. Either or both of these phenomena could be responsible for downstream activations that lead to movement initiation. One possibility is that synchronous activation along the medio-lateral axis and rostro-caudal cortical sequencing led to non-linear amplification of muscle activity which support movement initiation and generation. Further experiments will be needed to shed light on the exact nature of the downstream sensitivity to these natural spatiotemporal patterns.

Our results suggest that these propagating sequences serve a generic role in initiating movements and do not depend on the nature of the movement or the temporal sequencing of limb segments. Although we have not examined this question in great depth, our findings from monkey Bx demonstrate that the bimodal distributions of BAOs and functional connectivity are not statistically different between movements toward and away from the animal. Moreover, the spatial structure of these propagating patterns is nearly orthogonal to the medio-lateral gradient from proximal to distal representations. This suggests that these propagating sequences are likely not the result of proximal-to-distal sequencing that is observed in certain motor behaviors (Hirashima et al., 2002; Karst and Hasan, 1991).

These results have broad significance because they suggest that large-scale, spatially structured propagating patterns of activity may be a common strategy used in various cortical areas to perform behaviorally relevant computations. Spatio-temporal patterns such as traveling planar, radial, circular, and spiral waves have been documented across different cortical areas including somatosensory (Ferezou et al., 2007; Petersen et al., 2003), visual (Han et al., 2008; Muller et al., 2014; Prechtl et al., 1997; Sato et al., 2012; Xu et al., 2007; Zanos et al., 2015), auditory (Song et

al., 2006; Witte et al., 2007) cortices, and hippocampus. At the spatial scale that we examined these attenuation patterns, we found that they could be characterized as planar propagating patterns in over 70% of trials, but we do not rule out the possibility that more complex patterns would be observed at larger scales. Various functional roles for these spatio-temporal patterns have been put forth but it remains a possibility that they are epiphenomena of the recurrently connected cortex (Muller et al., 2018). Multi-site, spatio-temporal stimulation may be an important approach to provide more direct support for a role of these patterns in cortical processing.

Data and code availability

Behavioral data and custom code to reproduce figures can be made available upon request by the lead contact.

Author contribution

K.B., V.P. and W.L. contributed to multiple aspects of the work including surgical procedures, experimental design, data analysis, and manuscript writing/editing as well as data collection for monkeys Ls and Bx. K.B. and N.G.H. were responsible for the single-trial BAO estimation techniques. K.B., K.T. and N.G.H. contributed to the development of the functional connectivity analyses. K.T., M.B. and A.J.S. helped conceive of the patterned stimulation paradigm and contributed to surgical procedures, manuscript editing, and data collection for monkey Mk. N.G.H. supervised the study and contributed to surgical procedures, experimental design, data analysis, and manuscript writing.

Acknowledgments

We would like to thank Carrie Anne Balcer for assistance in animal care and training as well as Callum Ross, Juan Alvaro Gallego, and Raeed Chowdhury for assistance in chronic EMG implants.

Funding

This work was supported by the National Institute of Neurological Disorders and Stroke at the National Institutes of Health (Grants R01 NS045853 and R01 NS111982 to N.G.H.). This work used the Beagle supercomputer resources provided by the Computation Institute and the Biological Sciences Division of the University of Chicago and Argonne National Laboratory, and the Midway cluster at the Research Computing Center of the University of Chicago.

Competing interests

N.G.H. serves as a consultant for BlackRock Microsystems, Inc., the company that sells the multi-electrode arrays and acquisition system used in this study.

References

Baker, S. N., Olivier, E., & Lemon, R. N. (1997). Coherent oscillations in monkey motor cortex and hand muscle EMG show task-dependent modulation. *The Journal of physiology*, 501(Pt 1), 225.

Best, M. D., Suminski, A. J., Takahashi, K., Brown, K. A., & Hatsopoulos, N. G. (2016). Spatio-temporal patterning in primary motor cortex at movement onset. *Cerebral Cortex*, 27(2), bhv327.

Bullock, D., & Grossberg, S. (1988). Neural dynamics of planned arm movements: emergent invariants and speed-accuracy properties during trajectory formation. *Psychological review*, 95(1), 49.

Chase, M. H. (1983). Synaptic mechanisms and circuitry involved in motoneuron control during sleep. *International Review of Neurobiology*, 24, 213-258.

Chen, R., Yaseen, Z., Cohen, L. G., & Hallett, M. (1998). Time course of corticospinal excitability in reaction time and self-paced movements. *Annals of neurology*, 44(3), 317-325.

Chronux Home, http://chronux.org/ (accessed 5.7.19).

Churchland, M. M., Cunningham, J. P., Kaufman, M. T., Foster, J. D., Nuyujukian, P., Ryu, S. I., & Shenoy, K. V. (2012). Neural population dynamics during reaching. *Nature*, 487(7405), 51-56.

Churchland, M. M., Santhanam, G., & Shenoy, K. V. (2006). Preparatory activity in premotor and motor cortex reflects the speed of the upcoming reach. *Journal of neurophysiology*, 96(6), 3130-3146.

Churchland, M. M., & Shenoy, K. V. (2007). Delay of movement caused by disruption of cortical preparatory activity. *Journal of neurophysiology*, 97(1), 348-359.

Crammond, D. J., & Kalaska, J. F. (2000). Prior information in motor and premotor cortex: activity during the delay period and effect on pre-movement activity. *Journal of neurophysiology*, 84(2), 986-1005.

Denker, M., Zehl, L., Kilavik, B. E., Diesmann, M., Brochier, T., Riehle, A., & Grün, S. (2018). LFP beta amplitude is linked to mesoscopic spatio-temporal phase patterns. *Scientific reports*, 8(1), 1-21.

Donoghue, J. P., Sanes, J. N., Hatsopoulos, N. G., & Gaál, G. (1998). Neural discharge and local field potential oscillations in primate motor cortex during voluntary movements. *Journal of neurophysiology*, 79(1), 159-173.

Ferezou, I., Haiss, F., Gentet, L. J., Aronoff, R., Weber, B., & Petersen, C. C. (2007). Spatiotemporal dynamics of cortical sensorimotor integration in behaving mice. *Neuron*, 56(5), 907-923.

Gatter, K. C., Sloper, J. J., & Powell, T. P. (1978). The intrinsic connections of the cortex of area 4 of the monkey. *Brain: a journal of neurology*, 101(3), 513-541.

Georgopoulos, A. P., Kalaska, J. F., Caminiti, R., & Massey, J. T. (1982). On the relations between the direction of two-dimensional arm movements and cell discharge in primate motor cortex. *Journal of Neuroscience*, 2(11), 1527-1537.

Hagan, M. T., & Menhaj, M. B. (1994). Training feedforward networks with the Marquardt algorithm. *IEEE transactions on Neural Networks*, 5(6), 989-993.

Haller, M., Donoghue, T., Peterson, E., Varma, P., Sebastian, P., Gao, R., ... & Voytek, B. (2018). Parameterizing neural power spectra. *BioRxiv*, 299859.

Han, F., Caporale, N., & Dan, Y. (2008). Reverberation of recent visual experience in spontaneous cortical waves. *Neuron*, 60(2), 321-327.

Hanes, D. P., & Schall, J. D. (1996). Neural control of voluntary movement initiation. *Science*, 274(5286), 427-430.

Hao, Y., Riehle, A., & Brochier, T. G. (2016). Mapping horizontal spread of activity in monkey motor cortex using single pulse microstimulation. *Frontiers in neural circuits*, 10, 104.

Hatsopoulos, N., Joshi, J., & O'Leary, J. G. (2004). Decoding continuous and discrete motor behaviors using motor and premotor cortical ensembles. *Journal of neurophysiology*, 92(2), 1165-1174.

Hatsopoulos, N. G., & Suminski, A. J. (2011). Sensing with the motor cortex. *Neuron*, 72(3), 477-487.

He, S. Q., Dum, R. P., & Strick, P. L. (1993). Topographic organization of corticospinal projections from the frontal lobe: motor areas on the lateral surface of the hemisphere. *Journal of Neuroscience*, 13(3), 952-980.

Hirashima, M., Kadota, H., Sakurai, S., Kudo, K., & Ohtsuki, T. (2002). Sequential muscle activity and its functional role in the upper extremity and trunk during overarm throwing. *Journal of sports sciences*, 20(4), 301-310.

Hocherman, S., & Wise, S. P. (1991). Effects of hand movement path on motor cortical activity in awake, behaving rhesus monkeys. *Experimental brain research*, 83(2), 285-302.

Karst, G. M., & Hasan, Z. (1991). Timing and magnitude of electromyographic activity for two-joint arm movements in different directions. *Journal of Neurophysiology*, 66(5), 1594-1604.

Kaufman, M. T., Churchland, M. M., Ryu, S. I., & Shenoy, K. V. (2014). Cortical activity in the null space: permitting preparation without movement. *Nature neuroscience*, 17(3), 440-448.

Kilner, J. M., Baker, S. N., Salenius, S., Hari, R., & Lemon, R. N. (2000). Human cortical muscle coherence is directly related to specific motor parameters. *Journal of Neuroscience*, 20(23), 8838-8845.

Kim, S., Putrino, D., Ghosh, S., & Brown, E. N. (2011). A Granger causality measure for point process models of ensemble neural spiking activity. *PLoS computational biology*, 7(3), e1001110.

Kühn, A. A., Williams, D., Kupsch, A., Limousin, P., Hariz, M., Schneider, G. H., ... & Brown, P. (2004). Event-related beta desynchronization in human subthalamic nucleus correlates with motor performance. *Brain*, 127(4), 735-746.

Kwan, H. C., Mackay, W. A., Murphy, J. T., & Wong, Y. C. (1978). An intracortical microstimulation study of output organization in precentral cortex of awake primates. *Journal de physiologie*, 74(3), 231-233.

Kwan, H. C., MacKay, W. A., Murphy, J. T., & Wong, Y. C. (1978). Spatial organization of precentral cortex in awake primates. II. Motor outputs. *Journal of neurophysiology*, 41(5), 1120-1131.

Lepage, J. F., Saint-Amour, D., & Théoret, H. (2008). EEG and neuronavigated single-pulse TMS in the study of the observation/execution matching system: are both techniques measuring the same process?. *Journal of neuroscience methods*, 175(1), 17-24.

Mäki, H., & Ilmoniemi, R. J. (2010). EEG oscillations and magnetically evoked motor potentials reflect motor system excitability in overlapping neuronal populations. *Clinical neurophysiology*, 121(4), 492-501.

Marquardt, D. W. (1963). An algorithm for least-squares estimation of nonlinear parameters. *Journal of the society for Industrial and Applied Mathematics*, 11(2), 431-441.

Maynard, E. M., Hatsopoulos, N. G., Ojakangas, C. L., Acuna, B. D., Sanes, J. N., Normann, R. A., & Donoghue, J. P. (1999). Neuronal interactions improve cortical population coding of movement direction. *Journal of Neuroscience*, 19(18), 8083-8093.

Muller, L., Chavane, F., Reynolds, J., & Sejnowski, T. J. (2018). Cortical travelling waves: mechanisms and computational principles. *Nature Reviews Neuroscience*, 19(5), 255-268.

Muller, L., Reynaud, A., Chavane, F., & Destexhe, A. (2014). The stimulus-evoked population response in visual cortex of awake monkey is a propagating wave. *Nature communications*, 5(1), 1-14.

Murthy, V. N., & Fetz, E. E. (1996). Oscillatory activity in sensorimotor cortex of awake monkeys: synchronization of local field potentials and relation to behavior. *Journal of neurophysiology*, 76(6), 3949-3967.

Murthy, V. N., & Fetz, E. E. (1992). Coherent 25-to 35-Hz oscillations in the sensorimotor cortex of awake behaving monkeys. *Proceedings of the National Academy of Sciences*, 89(12), 5670-5674.

Park, M. C., Belhaj-Saïf, A., & Cheney, P. D. (2004). Properties of primary motor cortex output to forelimb muscles in rhesus macaques. *Journal of neurophysiology*, 92(5), 2968-2984.

Park, M. C., Belhaj-Saïf, A., Gordon, M., & Cheney, P. D. (2001). Consistent features in the forelimb representation of primary motor cortex in rhesus macaques. *Journal of Neuroscience*, 21(8), 2784-2792.

Pernet, C. R., Sajda, P., & Rousselet, G. A. (2011). Single-trial analyses: why bother?. *Frontiers in psychology*, 2, 322.

Petersen, C. C., Grinvald, A., & Sakmann, B. (2003). Spatiotemporal dynamics of sensory responses in layer 2/3 of rat barrel cortex measured in vivo by voltage-sensitive dye imaging combined with whole-cell voltage recordings and neuron reconstructions. *Journal of neuroscience*, 23(4), 1298-1309.

Pfurtscheller, G., & Da Silva, F. L. (1999). Event-related EEG/MEG synchronization and desynchronization: basic principles. *Clinical neurophysiology*, 110(11), 1842-1857.

Pompeiano, O. (1967). Functional organization of the cerebellar projections to the spinal cord. *Progress in brain research*, 25, 282-321.

Prechtl, J. C., Cohen, L. B., Pesaran, B., Mitra, P. P., & Kleinfeld, D. (1997). Visual stimuli induce waves of electrical activity in turtle cortex. *Proceedings of the National Academy of Sciences*, 94(14), 7621-7626.

Riehle, A., & Requin, J. (1993). The predictive value for performance speed of preparatory changes in neuronal activity of the monkey motor and premotor cortex. *Behavioural brain research*, 53(1-2), 35-49.

Rubino, D., Robbins, K. A., & Hatsopoulos, N. G. (2006). Propagating waves mediate information transfer in the motor cortex. *Nature neuroscience*, 9(12), 1549-1557.

Rule, M. E., Vargas-Irwin, C., Donoghue, J. P., & Truccolo, W. (2018). Phase reorganization leads to transient β-LFP spatial wave patterns in motor cortex during steady-state movement preparation. *Journal of neurophysiology*, 119(6), 2212-2228.

Salmelin, R., & Hari, R. (1994). Spatiotemporal characteristics of sensorimotor neuromagnetic rhythms related to thumb movement. *Neuroscience*, 60(2), 537-550.

Sanes, J. N., Donoghue, J. P., Thangaraj, V., Edelman, R. R., & Warach, S. (1995). Shared neural substrates controlling hand movements in human motor cortex. *Science*, 268(5218), 1775-1777.

Sato, T. K., Nauhaus, I., & Carandini, M. (2012). Traveling waves in visual cortex. *Neuron*, 75(2), 218-229.

Schulz, H., Übelacker, T., Keil, J., Müller, N., & Weisz, N. (2014). Now I am ready—now I am not: the influence of pre-TMS oscillations and corticomuscular coherence on motor-evoked potentials. *Cerebral cortex*, 24(7), 1708-1719.

Solodkin, A., Hlustik, P., Chen, E. E., & Small, S. L. (2004). Fine modulation in network activation during motor execution and motor imagery. *Cerebral cortex*, 14(11), 1246-1255.

Song, W. J., Kawaguchi, H., Totoki, S., Inoue, Y., Katura, T., Maeda, S., ... & Nishimura, M. (2006). Cortical intrinsic circuits can support activity propagation through an isofrequency strip of the guinea pig primary auditory cortex. *Cerebral cortex*, 16(5), 718-729.

Takahashi, K., Kim, S., Coleman, T. P., Brown, K. A., Suminski, A. J., Best, M. D., & Hatsopoulos, N. G. (2015). Large-scale spatiotemporal spike patterning consistent with wave propagation in motor cortex. *Nature communications*, 6(1), 1-11.

Takahashi, K., Saleh, M., Penn, R. D., & Hatsopoulos, N. G. (2011). Propagating waves in human motor cortex. *Frontiers Human Neuroscience*, 5, 40.

Tkach, D., Reimer, J., & Hatsopoulos, N. G. (2007). Congruent activity during action and action observation in motor cortex. *Journal of Neuroscience*, 27(48), 13241-13250.

Vigneswaran, G., Philipp, R., Lemon, R. N., & Kraskov, A. (2013). M1 corticospinal mirror neurons and their role in movement suppression during action observation. *Current Biology*, 23(3), 236-243.

Williams, D., Kühn, A., Kupsch, A., Tijssen, M., Van Bruggen, G., Speelman, H., ... & Brown, P. (2005). The relationship between oscillatory activity and motor reaction time in the parkinsonian subthalamic nucleus. *European Journal of Neuroscience*, 21(1), 249-258.

Witte, R. S., Rousche, P. J., & Kipke, D. R. (2007). Fast wave propagation in auditory cortex of an awake cat using a chronic microelectrode array. *Journal of neural engineering*, 4(2), 68.

Xu, W., Huang, X., Takagaki, K., & Wu, J. Y. (2007). Compression and reflection of visually evoked cortical waves. *Neuron*, 55(1), 119-129.

Zanos, T. P., Mineault, P. J., Nasiotis, K. T., Guitton, D., & Pack, C. C. (2015). A sensorimotor role for traveling waves in primate visual cortex. *Neuron*, 85(3), 615-627.

Supplementary material

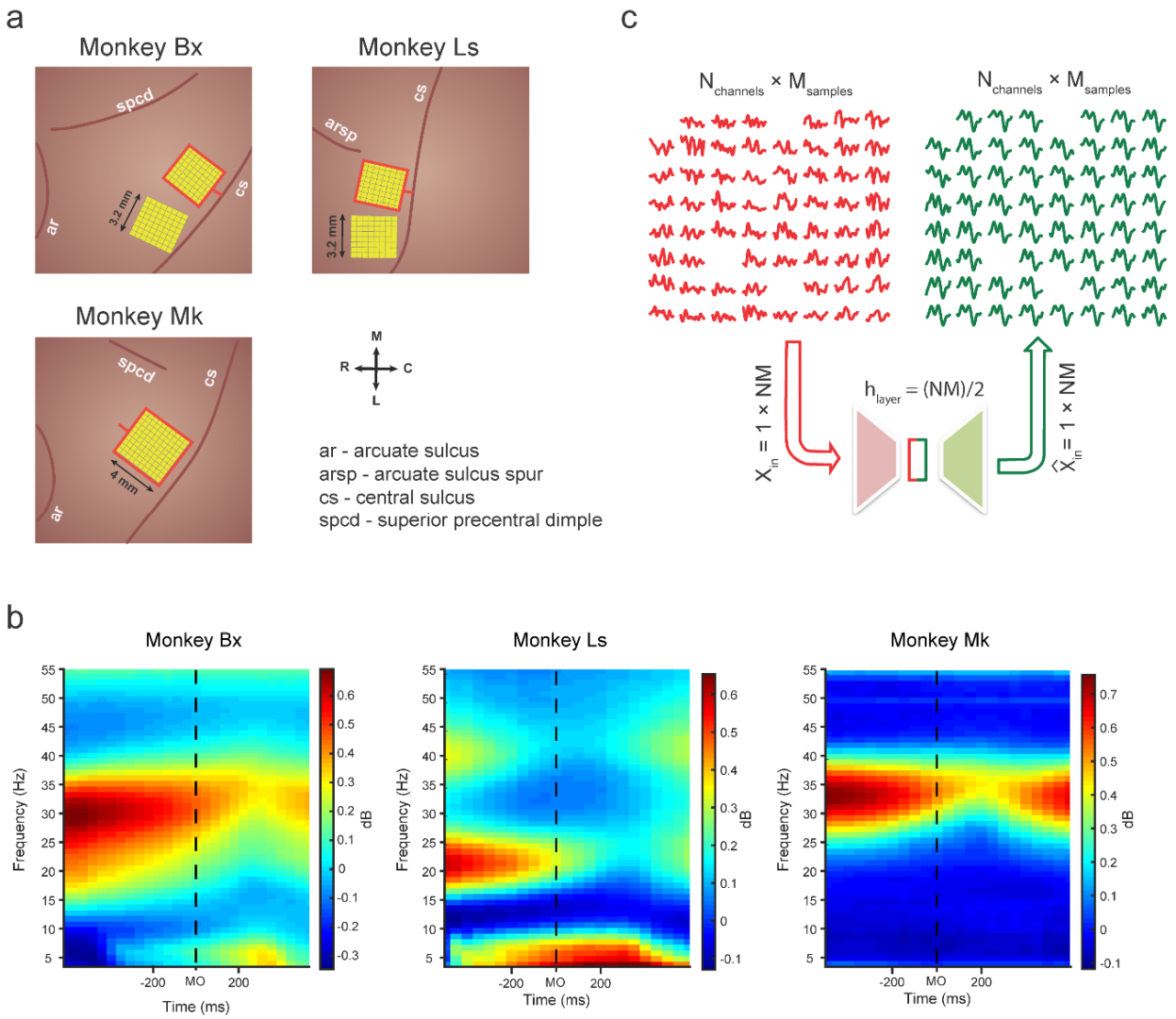

Figure A.S1 - related to Figure A.1. Multi-electrode array implantation and neural signal characteristics. a. Multi-electrode arrays were implanted in the primary motor cortex (M1) of three macaques (Bx, Ls, and Mk). The arrays marked with red border were used for analyses and patterned stimulation experiments. **b.** Spectral features show change in beta power relative to movement onset. Spectrograms were averaged over trials, channels and sessions for the three monkeys (Bx: left; Ls: middle; Mk: right). Data were aligned on movement onset (MO) and power spectra were computed in 1-second windows, with 50 ms sliding window. Color represents the power after subtracting the 1/f estimation of the aperiodic signal. **c.** The beta band envelopes from single trials were auto-encoded to de-noise the neural signals. Beta envelopes from N-channels sampled at 100 Hz (M-samples) were projected using the auto-encoder. The hidden layer consisted of (NM)/2 neurons, resembling a bottleneck architecture.

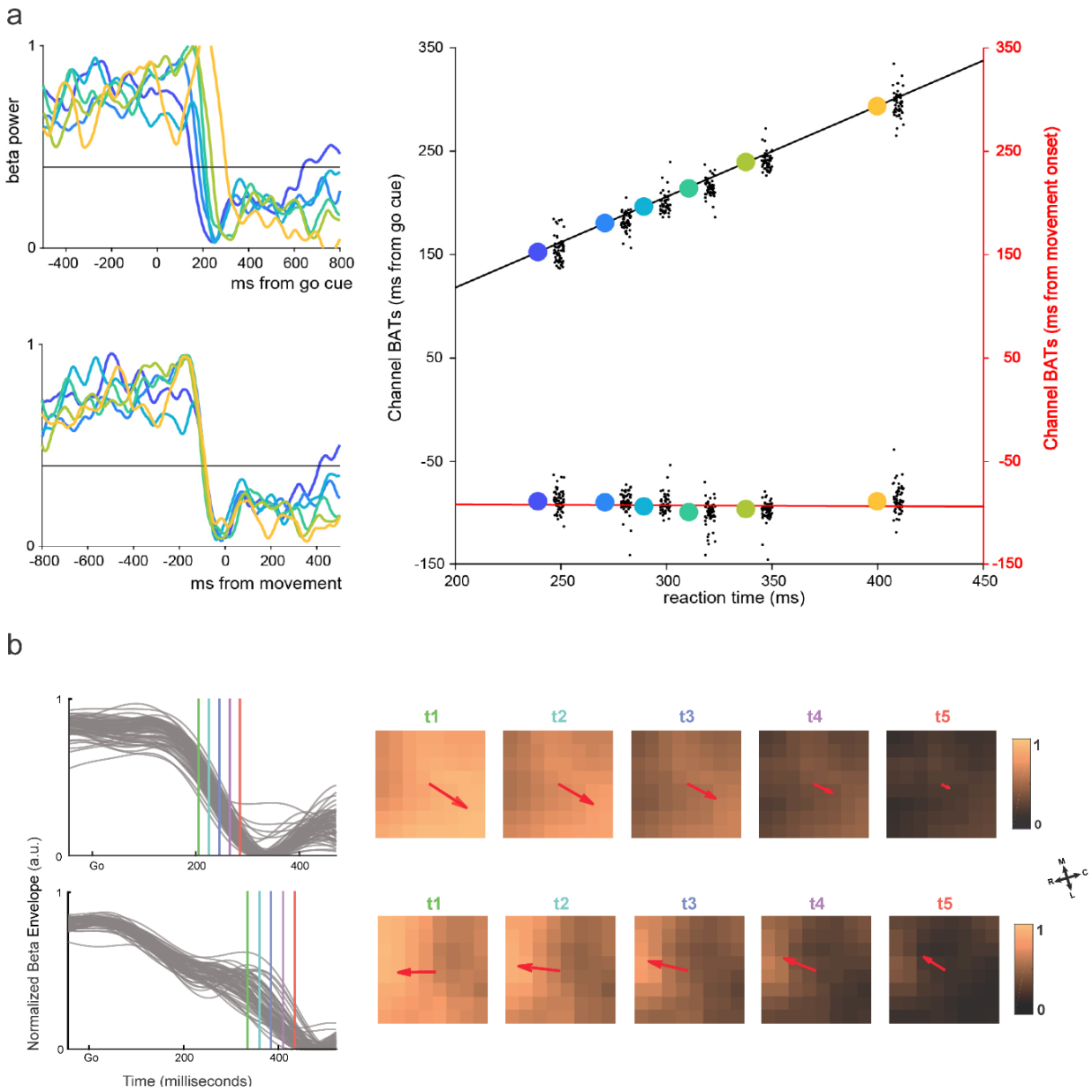

Figure A.S2 - related to Figure A.1. Beta attenuation times are time-locked to movement initiation and beta envelopes exhibit a spatial gradient. a. Normalized beta envelopes averaged over different trial groups from one session in monkey Bx. Trials were sorted based on reaction time and grouped in bins of 55 trials. Color represents reaction time average of each group from shortest (blue) to longest (yellow) trials. Average beta power for each group is plotted aligned on reaction time (top left) or on movement onset (bottom left). (right) Channel-averaged beta attenuation time regressed on mean reaction time in each trial group with respect to the GO cue (black line, $r^2 = 0.998$, p = 8e-9) or movement onset (red line $r^2 = 0.009$, p = 0.853). Each big colored dot represents channel-averaged values and each black dot represents single channel values. Color represents reaction time average of each group from shortest (blue) to longest (yellow) trials. b. Beta envelopes across channels from Monkey Bx for two trials (left) along with their corresponding spatial patterning (right) at different times (corresponding to vertical colored lines on left panel). Orientations of regression fits to the spatial patterning are denoted with arrows.

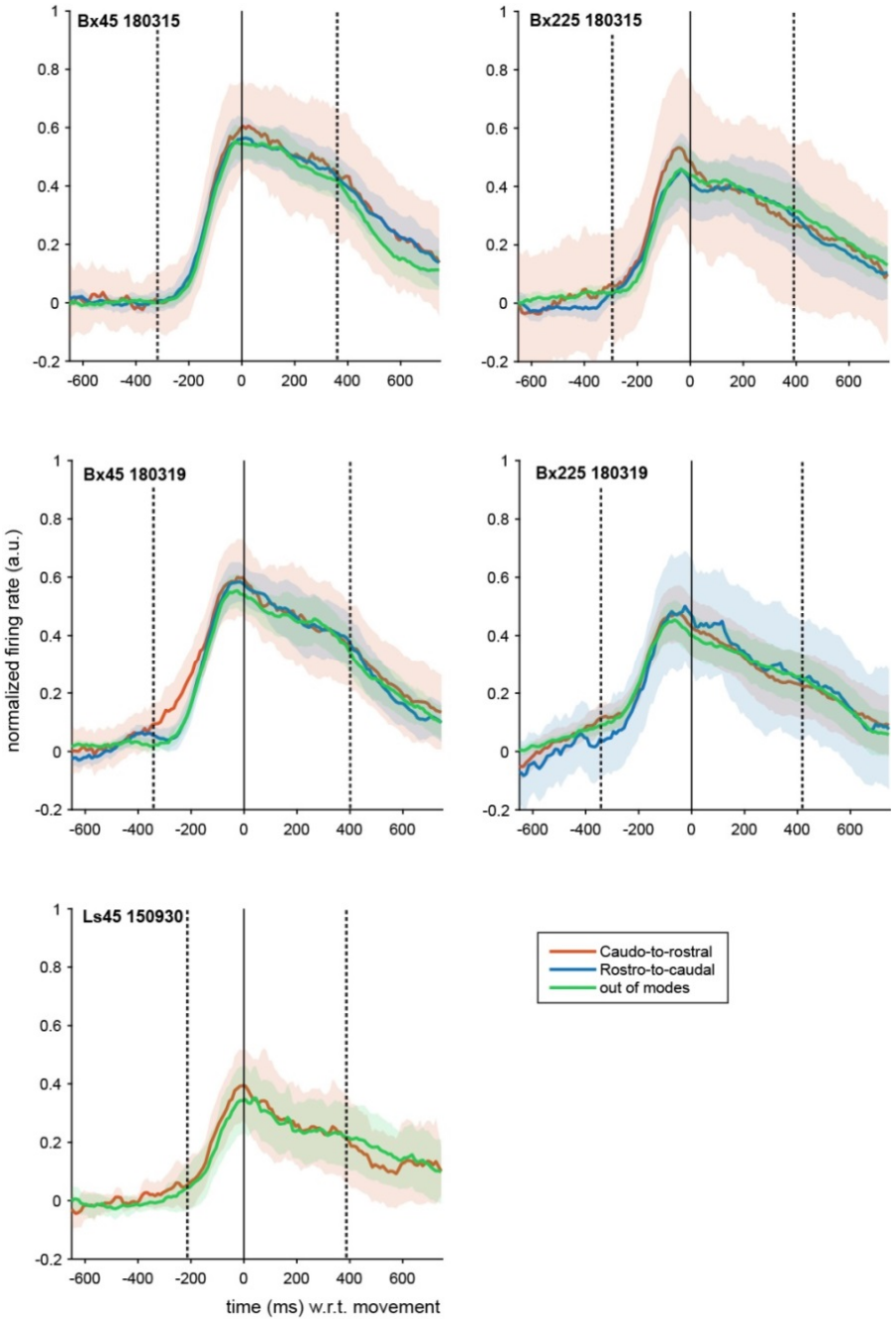

Figure A.S3 - related to Figure A.4. Population firing rate profiles in and outside BAO modes. Population peri-movement time histograms based on 32 to 60 multi-unit sites for trials in the caudal-to-rostral BAO mode (red line), rostral-to-caudal BAO mode (blue line), and trials outside of the two modes (green line) for representative datasets. Trials were aligned on movement onset (black vertical line) and each multi-unit site's firing rate profile was normalized before averaging (see Methods). Dotted vertical lines represent the median go cue and movement end. Shaded areas represent standard error of the mean.

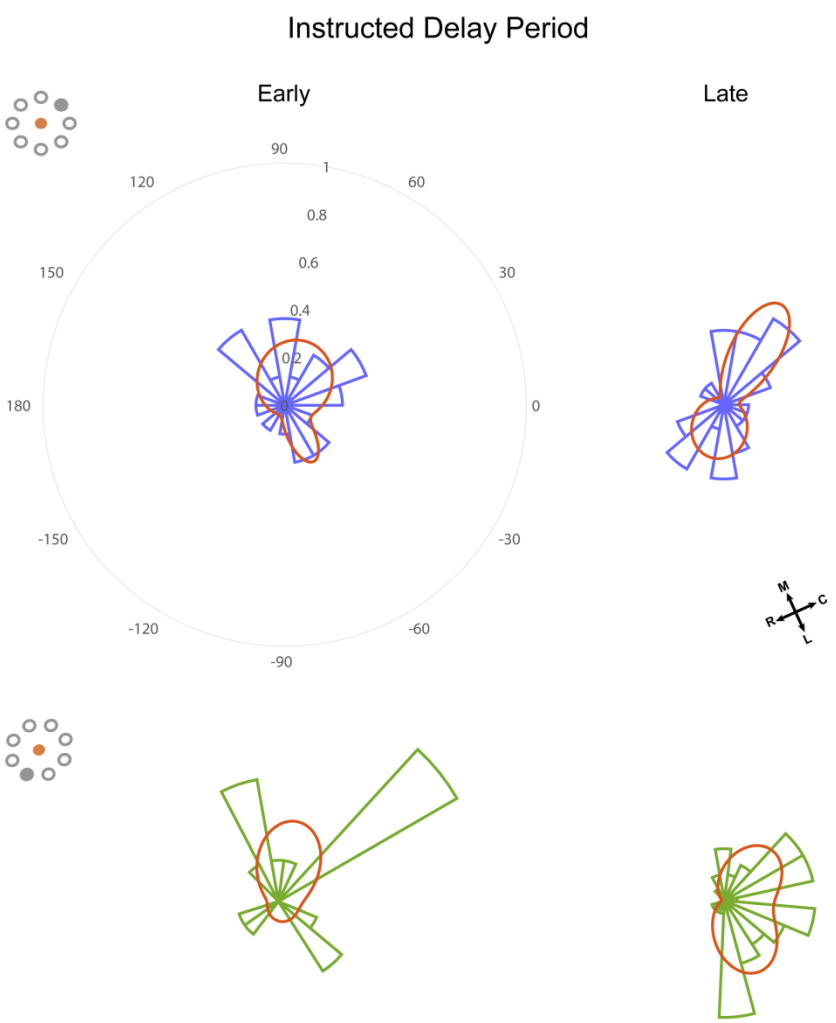

Figure A.S4 - related to Figure A.4. Distribution of functional connections during movement planning in an Instructed-delay task. Directional distributions of functional connections estimated using multi-unit activity is shown for early (100 to 350 ms after the instruction cue onset, total of 24 (for Bx45) and 16 (for Bx225) significant connections) and late (600 to 850 ms after the instruction cue onset, total of 28 (for Bx45) and 22 (for Bx225) significant connections) phases of the instructed delay period. The top panels are for monkey Bx reaching to the target at 45 degrees, and the bottom panels corresponds to reaches at 225 degrees. The distributions were fit with a mixture of two von Mises functions (red curves).

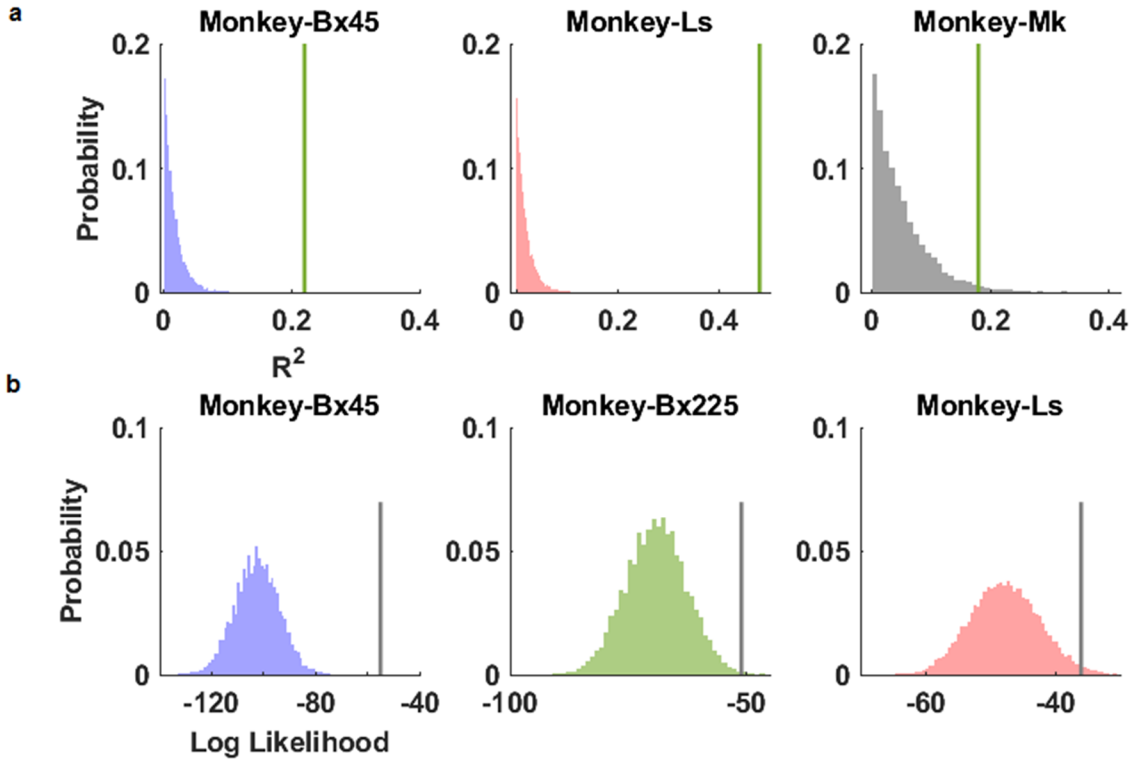

Figure A.S5 - related to Figures A.4 and A.5. Statistical significance of the proximal-to-distal somatotopic gradient and the bimodal distribution of the estimated functional connectivity maps. (a) The distribution of R^2 of the somatotopic gradient when electrode positions were shuffled is shown. The somatotopic gradient was computed by randomly permuting the electrode positions 10,000 times and multiple linear regression was used to determine the fit (R^2) to each permutation. The unshuffled model had significantly higher R^2 values (p value: 0.0 for Bx45 and Ls, and 0.02 for Mk). (b) The distribution of the log likelihood fits of a two-element von Mises mixture model to the distribution of functional connectivity with shuffled electrodes is shown. The electrode positions were randomly permuted10,000 times and the two-element von Mises mixture model was fit to the distribution of functional connectivity for each permutation. The original model showed significantly larger log likelihood fits compared to the shuffled models for the monkeys Bx and Ls (p value: 0.0 for Bx45, 0.0023 for Bx225 and 0.016 for Ls).

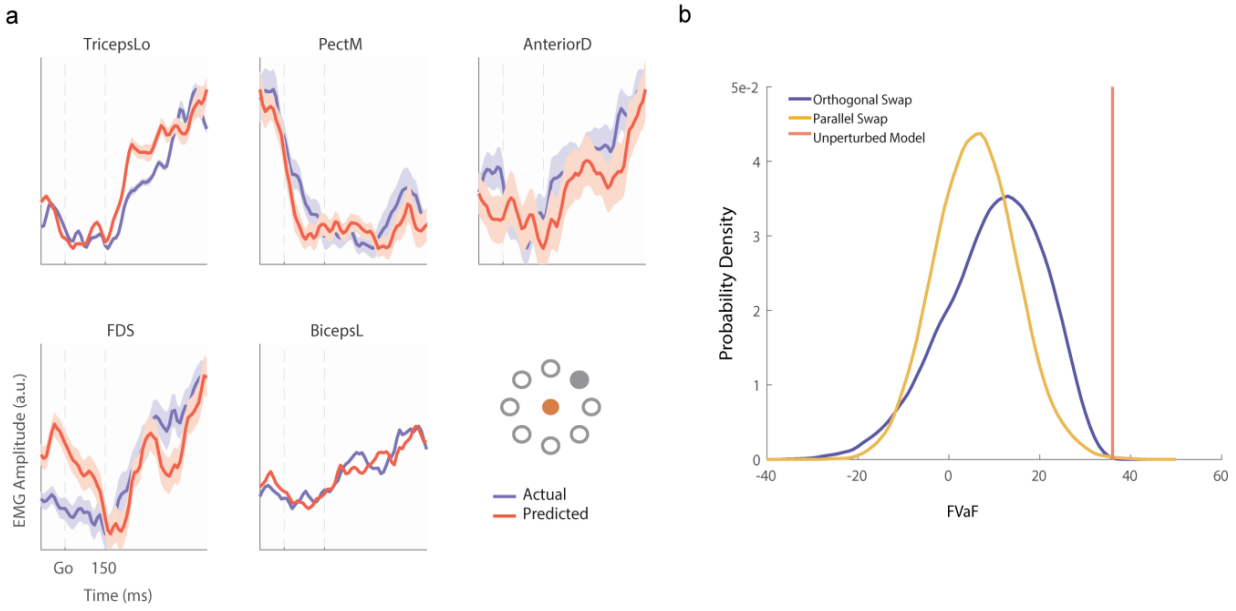

Figure A.S6 - related to Figure A.6. Effects of spatial perturbations on EMG predictions in monkey Ls. a. Trial-average predicted EMG (red) and actual EMG (blue) and profiles using a neural network trained with beta envelopes from Monkey Ls. **b.** Distributions of FVaFs over 5000 swaps are shown for the parallel swap condition (yellow; mean FVaF of 5%) and the orthogonal swap condition (blue; mean FVaF of 10%) along with the FVaF of the original unperturbed model (red line; mean FVaF of 36.5% (varying from 15 % to 51% across muscles). Inset represent the initial hold (filled red) and target positions (filled gray) of the hand.